MULTI-FEATURE FUSION FOR GPR-BASED LANDMINE DETECTION AND CLASSIFICATION

A THESIS SUBMITTED TO
THE GRADUATE SCHOOL OF NATURAL AND APPLIED SCIENCES
OF
MIDDLE EAST TECHNICAL UNIVERSITY

BY

ALPER GENÇ

IN PARTIAL FULFILLMENT OF THE REQUIREMENTS
FOR
THE DEGREE OF DOCTOR OF PHILOSOPHY
IN
ELECTRICAL AND ELECTRONIC ENGINEERING

APRIL 2019

Approval of the thesis:

MULTI-FEATURE FUSION FOR GPR-BASED LANDMINE DETECTION AND CLASSIFICATION

submitted by **ALPER GENÇ** in partial fulfillment of the requirements for the degree of **Doctor of Philosophy in Electrical and Electronic Engineering Department, Middle East Technical University** by,

Prof. Dr. Halil Kalıpçılar
Dean, Graduate School of **Natural and Applied Sciences**   _____

Prof. Dr. Tolga Çiloğlu
Head of Department, **Electrical and Electronic Eng.**   _____

Prof. Dr. Gözde Bozdağı Akar
Supervisor, **Electrical and Electronic Eng., METU**   _____

_____

Examining Committee Members:

Prof. Dr. Gönül Turhan Sayan
Electrical and Electronic Eng., METU   _____

Prof. Dr. Gözde Bozdağı Akar
Electrical and Electronic Eng., METU   _____

Prof. Dr. Özlem Aydın Çivi
Electrical and Electronic Eng., METU   _____

Prof. Dr. Ziya Telatar
Electrical and Electronic Eng., Ankara University.   _____

Assoc. Prof. Dr. Seniha Esen Yüksel
Electrical and Electronic Eng., Hacettepe University   _____

Date: 15.04.2019

I hereby declare that all information in this document has been obtained and presented in accordance with academic rules and ethical conduct. I also declare that, as required by these rules and conduct, I have fully cited and referenced all material and results that are not original to this work.

Name, Surname: Alper Genç

Signature:

ABSTRACT

**MULTI-FEATURE FUSION FOR GPR-BASED LANDMINE DETECTION
AND CLASSIFICATION**

Genç, Alper
Doctor of Philosophy, Electrical and Electronic Engineering
Supervisor: Prof. Dr. Gözde Bozdağı Akar

April 2019, 122 pages

Ground penetrating radar (GPR) is a powerful technology for detection and identification of buried explosives especially with little or no metal content. However, subsurface clutter and soil distortions increase false alarm rates of current GPR-based landmine detection and identification methods. Most existing algorithms use shape-based, image-based and physics-based techniques. Analysis of these techniques indicates that each type of algorithms has a different perspective to solve landmine detection and identification problem. Therefore, one type of method has stronger and weaker points with respect to the other types of algorithms.

To reduce false alarm rates of the current GPR-based landmine detection and identification methods, this study proposes a combined feature utilizing both physics-based and image-based techniques. Combined features are classified with support vector machine (SVM) classifier. The proposed algorithm is tested on a simulated data set contained more than 400 innocuous object signatures and 300 landmine signatures, over half of which are completely nonmetal. The results presented indicate that the proposed method in this study has significant performance benefits for landmine detection and identification in GPR data even in cluttered environment.

ÖZ

GPR'A DAYALI KARAMAYINI TESPİTİ VE SINIFLANDIRILMASI İÇİN ÇOKLU-ÖZELLİK FÜZYONU

Genç, Alper
Doktora, Elektrik ve Elektronik Mühendisliği
Tez Danışmanı: Prof. Dr. Gözde Bozdağı Akar

Nisan 2019, 122 sayfa

Yere nüfuz eden radar (GPR), yer altındaki patlayıcıların, özellikle az miktarda metal içeren veya hiç içermeyen gömülü cisimlerin tespiti ve teşhisi için güçlü bir teknolojidir. Fakat yer altı kargaşa ve toprak bozulmaları mevcut GPR tabanlı mayın tespit ve teşhis yöntemlerinin yanlış alarm oranlarını artırmaktadır. Literatürdeki algoritmalar temel olarak şekil-tabanlı, görüntü-tabanlı ve fizik-tabanlı teknikler kullanır. Bu teknikler analiz edildiğinde, her bir algoritma türünün, kara mayını tespit ve tanımlama problemini çözmek için farklı bir bakış açısına sahip olduğu görülecektir. Bu nedenle, her bir algoritma türü, diğer algoritma türlerine göre daha güçlü ve daha zayıf noktalara sahiptir.

Bu çalışma, mevcut GPR tabanlı mayın tespit ve tanımlama yöntemlerinin yanlış alarm oranlarını azaltmak için fizik-tabanlı yöntemler ile görüntü-tabanlı yöntemleri bir arada kullanan birleşik bir özellik önermektedir. Önerilen bu birleşik özellikler destek vektör makinesi (SVM) sınıflandırıcısı ile sınıflandırılmaktadır. Bu çalışmada önerilen algoritma, yarısından fazlası hiç metal içermeyen 300'den fazla simüle edilmiş mayın modeli ve 400'den fazla simüle edilmiş zararsız cisim modeli kullanılarak test edildi. Sonuçlar, bu çalışmada önerilen yöntemin, GPR verisi üzerinde mayın tespiti ve tanımlanması için kargaşa altındaki bir ortamda bile çok yüksek performansa sahip olduğunu göstermektedir.

Anahtar Kelimeler: Yere Nüfuz Eden Radar, Karamayını Teşhisi, Fizik Tabanlı Yaklaşım, Kümülatif Enerji Eğrisi, İçsel Empedans

This study is wholeheartedly dedicated to my beloved wife and lovely son, who have been my source of inspiration.

ACKNOWLEDGEMENTS

TABLE OF CONTENTS

LIST OF TABLES

LIST OF FIGURES

FIGURES

LIST OF ABBREVIATIONS

ABBREVIATIONS

AUC   : Area Under Curve

BRIEF   : Binary Robust Independent Elementary Features

CFAR   : Constant False Alarm Rate

CNN   : Convolutional Neural Network

CW   : Continuous Wave

EHD   : Edge Histogram Descriptors

EMI   : Electromagnetic Induction

FFT   : Fast Fourier Transform

FMCW   : Frequency Modulated Continuous Wave

FMICW   : Frequency Modulated Interrupted Continuous Wave

FN   : False Negative

FP   : False Positive

GPR   : Ground Penetrating Radar

HMM   : Hidden Markov Models

HoG   : Histogram of Oriented Gradients

ICA   : Independent Component Analysis

KNN   : K-nearest Neighbor

LMS   : Least Mean Squares

NMCW   : Noise Modulated Continuous Wave

PCA   : Principal Component Analysis

PEC   : Perfect Electrical Conductor

PLS-DA   : Partial Least Squares Discriminant Analysis

RBF   : Radial Basis Function

ROC   : Receiver Operating Characteristics

RPCA   : Robust Principal Component Analysis

RVM   : Relevance Vector Machine

RX   : Receiver

SFCW   : Stepped Frequency Continuous Wave

SIFT   : Scale Invariant Feature Transform

SMO   : Sequential Minimal Optimization

STFT   : Short Time Fourier Transform

SURF   : Speeded-up Robust Features

SVM   : Support Vector Machine

TN   : True Negative

TP   : True Positive

TX   : Transmitter

WVD   : Wigner Ville Distribution

LIST OF SYMBOLS

SYMBOLS

η : Intrinsic Impedance

Γ : Reflection Coefficient

τ : Transmission Coefficient

ϵ_0 : Permittivity of Free Space ($\cong 4\pi * 10^{-7}$)

ϵ_r : Relative Permittivity

μ_0 : Permeability of Free Space ($\cong \frac{1}{36\pi} * 10^{-9}$)

μ_r : Relative Permeability

σ : Conductivity

E_i : Electric Field of Incident Wave

E_r : Electric Field of Reflected Wave

E_t : Electric Field of Transmitted Wave

$E(z)$: Electric Field at a Distance z from the Source

γ : Propagation Constant

α : Attenuation Constant

β : Phase Constant

v : Velocity of the Signal

c : Speed of Light

h_a : Height of the GPR Antenna

h_t : Depth of the Target

h_c : Depth of the Calibration Object

CHAPTER 1

INTRODUCTION

Detection and removal of landmines is a major issue in both military and humanitarian applications. It is estimated that more than 110 million buried landmines are placed in about 70 countries [1]. Due to these landmines, there are more than 122000 recorded casualties in the period between 1999 and 2017. However, estimates show that there are another 7000 – 13000 annual casualties that were not recorded and most of their victims are children [2]. Over the last 50 years, landmines cause more death and injury than nuclear and chemical weapons combined. According to a research of the United Nations, to clear the buried landmines up to this day would take 1100 years and 33 billion dollars by using today's technology [3].

Because of the tragic effects of landmine explosion, finding the location of a buried landmine is an important and challenging problem. Production and deployment of a landmine is around 3 to 30 dollars. Therefore, employing landmines is an easy task and frequently used by some third nations and terrorist groups. However, removal costs are around 300 to 1000 dollars each [4]. The difficulty in removing landmines poses a great challenge to researchers around various parts of the world. Identification of buried landmines is very difficult due to different soil and weather conditions, different burial depths, large variety of landmine types, etc. Traditional approaches use EMI sensors (metal detectors), however modern mines (manufactured after 1950s) contain as little metal as possible to make them difficult to detect.

Ground penetrating radar (GPR) can detect landmines with little and even no metal content. GPR is a sensing technique that uses electromagnetic radiation, typically in UHF/L/S band, and detects the reflected signals from subsurface structures. Hence, non-metallic threats can be detected from the GPR measurement if the electromagnetic

properties of the buried object and the surrounding soil are sufficiently different. However, GPR measurements are also sensitive to subsurface changes because of the buried stones, roots, moisture variations etc. Hence, GPR based detection of buried threats can be subject to high false alarm rates and should be complemented by a proper discrimination algorithm. In the literature, many studies were performed to successfully detect and discriminate buried threats using GPR data. This previous research can be categorized into four broad classes: shape-based techniques, physics-based techniques, image-based techniques and convolutional neural networks (CNNs).

Shape-based techniques, which depend on detection of hyperbola-like shape in B-Scan image of GPR data, are popular due to its simplicity. When GPR antenna moves above an underground object, reflected signals from the buried target constitute a hyperbola shape in the corresponding B-Scan image. In this technique, the buried object is modeled as a point-scatterer and the surrounding soil is generally assumed homogeneous. The shape and structure of the resulting hyperbola contain information about the corresponding object and soil properties. Hough transform [5] and alternative fitting techniques [6] are the most popular shape-based object detection algorithms in GPR data. However, underground targets with moderate or large surface area and heterogeneous soil with clutter deteriorate the structure of the resulting hyperbola. Hence, the simplifying assumptions (point scatterer and homogeneous medium) decrease performance of the technique for real experiments.

Physics-based techniques for GPR processing depend on underlying theoretical foundations (Maxwell's equations, Green's functions, etc.). These techniques try to solve the resulting propagation equations to estimate intrinsic properties of the buried object. In the literature, specific studies were performed and published to estimate buried object shape and size [7] and there are also demining applications which exploit physics-based approach. These studies include advanced inversion techniques [8-9] to remove ground/antenna effects and extraction of physics-based features [10] for landmine detection. Since the GPR data belongs to a buried object within an unknown

2

environment, this approach tends to fail without accurate estimates of the subsurface electromagnetic properties of soil. Iterative estimation methods [11] are also available in the literature but they are computationally expensive and are not suitable for real-time operations.

Image-based algorithms are another popular GPR-based landmine identification method. Features are extracted from B-scan image of GPR data and then they are classified as threats or nonthreats [12-16]. The noise and uncertainty in real operations (due to heterogeneous soil, clutter, GPR transmit and receive noise, etc.) can be modeled successfully by these methods. Well-known image-based feature extraction techniques are hidden Markov Models (HMM) [17-19], Edge Histogram Descriptors (EHD) [20] and Histogram of Oriented Gradients (HoG) [21-23]. Last step of feature-based methods (image-based features or physics-based features) is classification. To generate accurate class boundaries, large amount of training data should be available that contains different target types under different surrounding conditions. If these algorithms are not trained successfully, the resulting performance decreases significantly.

Instead of computing the features beforehand and apply classification, these two-steps can be handled by CNNs. In the literature, there are specific studies for landmine detection using CNNs in GPR B-Scan data [24-26]. Although the results are quite promising, CNNs are difficult to train and a large variety of GPR data for landmines should be available to create a robust network. Without enough training GPR data (for very different landmines, under very different conditions, etc.), CNNs tend to converge local optimum and the performance will be low for other types of landmines under different conditions. Since most of the available GPR data of landmines belongs to army and generally confidential, it is difficult to gather enough data to train CNNs.

Each category of algorithms explained above (shape-based, physics-based, image-based and CNNs) has pros and cons. In the literature, there are also specific studies which combine different types of algorithms to increase the overall performance. In [27], physics-based features and statistical features are used together to decrease false-

alarm rates of GPR-based landmine detection algorithms. However, context is assumed to be homogeneous and the calculations are performed under this assumption. In [28], soil dielectric properties are estimated to identify the context by using physics-based approach and then image-based features are extracted based on this identifying context.

In this study, we also propose a system that jointly uses physics-based and image-based techniques for detection and classification. The main objective of the proposed method is to discriminate landmines from non-landmine targets such as buried large stones, plants roots, innocuous munitions, cans, plastic caps, etc. in GPR data. These non-landmine targets which have comparable sizes with landmines will be called as "innocuous object" for the rest of this study. Both landmines and innocuous objects are detected by the pre-screener algorithm given in Section 3.2 and they are classified as threat or non-threat in the proposed classification algorithm in Section 3.5. Unlike previous studies, both soil and target dielectric properties are calculated by utilizing physics-based equations in the proposed feature extraction algorithm. The proposed feature descriptor has computationally less expensive for both extraction and classification compared to descriptors found in the literature. In addition, the changes in the environment are modelled automatically by a "Context-based Parameter Update" step.

In the proposed system, initially a calibration measurement is taken in the experimental area similar to [27]. From this measurement, three calibration parameters are calculated: signal speed in the soil, dielectric properties and attenuation coefficient of the soil. After the calibration step, potential mine locations are determined with an LMS-based pre-screener algorithm. The calibration parameters are updated for each alarm location by observing the difference of the ground bounce between the calibration area and the alarm location. For classification of detected objects, three features are extracted from the B-scan data. The first feature estimates intrinsic impedance of the buried object. For this, object depth is calculated by using GPR signal speed in the soil and then intrinsic impedance of the object is computed by

4

means of intrinsic impedance and attenuation coefficient of the soil which are determined in the calibration step and updated for the corresponding alarm location. The second feature identifies the time length of significant GPR signal belongs to the buried object. To measure this, total energy value and cumulative energy curve of A-Scan data, which has the highest amplitude in the corresponding B-Scan image, is used. The third feature computes the gradient of the B-Scan image and the value of this feature depends on the size, especially surface area of the buried object. Finally, the underground target is classified by SVM based on the extracted features. The proposed algorithm is tested on a simulated data set. In the simulations, smaller objects (like small pebbles), soil heterogeneity or moisture variations underground which are not detected by the pre-screener as a target, but which deteriorate the GPR data of a landmine or innocuous object, are also modelled. These smaller objects, soil heterogeneity or moisture variations will be called as "clutter" for the rest of this study.

The main contribution of this thesis is to propose two new physics-based features, which are dielectric and energy feature, for landmine identification in GPR data. The proposed algorithm combines these features with an image-based feature, which is geometry feature, to increase discrimination power. This multi-feature fusion approach allows to estimate both the shape and the intrinsic properties of the buried objects. The experimental results show that the proposed features have very high discrimination power which reduces false alarm rates of various GPR-based landmine detection algorithms even in cluttered environment.

CHAPTER 2

BACKGROUND

2.1. Ground Penetrating Radar

Ground Penetrating Radar (GPR) is an instrument, which uses radar signals to image subsurface structures. GPR has many applications including landmine detection, archeology, soil inspection, boundary layer detection, mineral exploration, cavity detection, pavement inspection, pipeline detection and inspection, layered vegetation, etc. GPR uses radio waves with frequencies from 300 MHz up to 4 GHz depending on the application [29-31]. For GPR signals, there is a trade-off between the penetration depth and the resolution. Lower frequency signals can penetrate deeper in the ground at the cost of low resolution. On the other hand, higher frequency signals can measure subsurface structures in high resolution at the expense of low penetration depth. Therefore, the operating frequency of GPR should be selected according to the corresponding application. In this thesis, the targets of interest are anti-personal landmines, which are buried shallowly underground. Moreover, high-resolution measurement is needed to discriminate anti-personal landmines from innocuous objects. Hence, in this study the center frequency of GPR is chosen as around 1.5 GHz.

There are two common GPR types: time-domain (impulse) radar and frequency-domain (continuous wave (CW)) radar. A time-domain GPR transmits an impulse and receives the reflected signal as a function of time. For this GPR, the return signal is evaluated based on its arrival time and the changes in its amplitude. The target depth can be calculated by time-of-flight principle [31, 32]. Most commercial GPR systems are based on the impulse radar technique. In this study, we also propose a landmine identification problem based on time-domain GPR signals.

Continuous wave (CW) GPR transmits an infinite duration signal (such as continuous sine-wave) and receives the return signal simultaneously. For this GPR signal, detection of target depth is not possible, since the signal does not change. To make the detection possible, modulation techniques are applied in frequency-domain. Frequency Modulated Continuous Wave (FMCW) GPR, which is also called as "Swept Frequency Continuous Wave", transmits a frequency sweep from a start frequency to a stop frequency. Hence, FMCW uses the difference in frequency instead of time. However, FMCW GPR system suffers from interference since it uses a large frequency spectrum. To avoid occupying the large frequency spectrum, Stepped Frequency Continuous Wave (SFCW) GPR is used [31, 32]. Transmitting frequency of SFCW GPR is stepped in linear increments from a start frequency to a stop frequency. For this GPR, the weaker return signal from a deeper target can be masked by stronger signal, because the receiver is always active. This problem can be solved by gating the transmitter and receiver.

A common problem for continuous wave GPR systems is the strong reflection from the ground surface. Since the transmitted signal has infinite duration and the receiver is always on, the strong return signal from the ground surface can overshadow the reflections of the underground objects. To overcome this problem, Frequency Modulated Interrupted Continuous Wave (FMICW) and Noise Modulated Continuous Wave (NMCW) waveforms are proposed. Details of these waveforms can be found in [33].

The basic working principle of GPR includes a transmitter and a receiver as shown in Figure 2.1, that are moved above the surface to measure reflections from sub-surface objects.
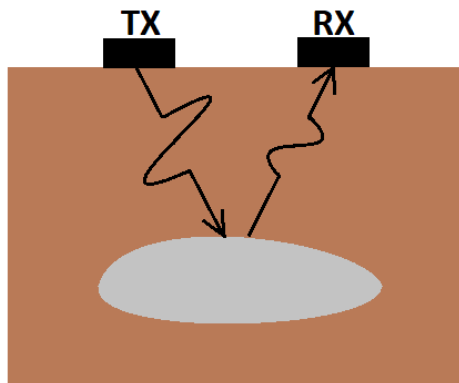
Figure 2.1. Basic Working Principle of GPR

GPR generally consists of a line array of transmitting antennas and receiving antennas as shown in Figure 2.2. The distance between two adjacent antennas is a few cm. The transmitting antenna array and the receiving antenna array can be straight or cross. For the straight case, the transmitted pulse of an antenna element is usually received by the corresponding receiving antenna element at the same order. For the cross case, the transmitted pulse of an antenna element is usually received by two receiving antenna elements across the transmitting antenna. For each case, the transmitted energy is reflected from various buried objects and receiving antennas receive the reflected waves back.
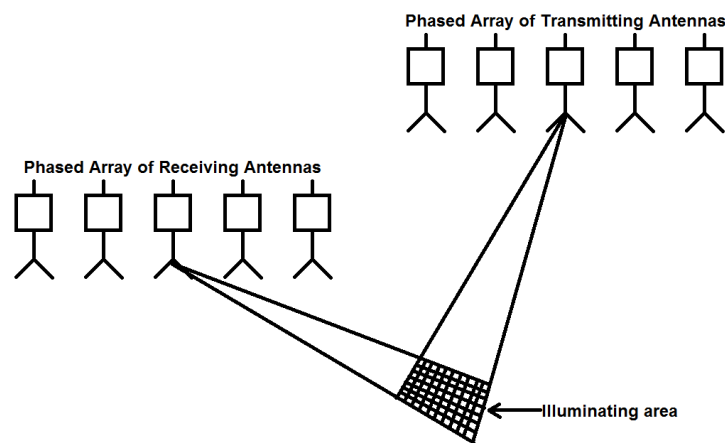
Figure 2.2. Line Array of Antennas

GPR data are usually represented as one or two-dimensional dataset that are denominated by A-, B- and C-Scans that is explained below.

A-Scan: At a fixed position (x_i, y_j), a single radar trace $A(x_i, y_j, t)$ is called as A-Scan given in Figure 2.3 [29-31]. The only variable is t and it is related by depth of the target and the propagation velocity of electromagnetic wave into the soil. When GPR transmits the incident wave, usually the highest reflection comes from air-ground interface due to the large dielectric discontinuity. This return is called as ground bounce that is shown in Figure 2.3.
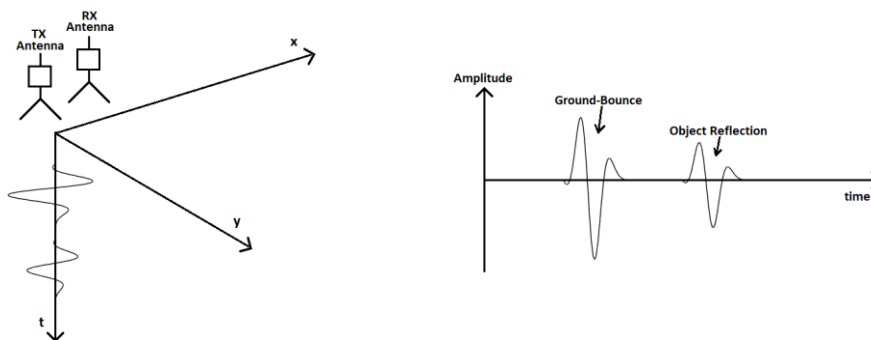
Figure 2.3. A-Scan Configuration and Representation

B-Scan: If the GPR antennas move along the x-axis and take measurements at specific locations, multiple A-Scans form a two dimensional dataset $B(x, y_j, t)$ which is called as B-Scan [29-31]. If the amplitude of the return signal is shown by a color-scale, a 2D image is obtained as given in Figure 2.4.
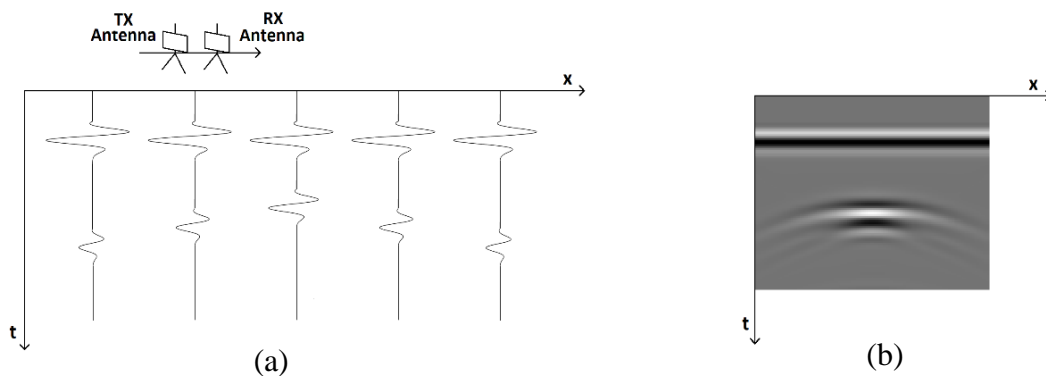
Figure 2.4. (a) B-Scan Formed by Multiple A-Scans, (b) 2D Representation of B-Scan

C-Scan: If the GPR antennas move over a regular grid in x-y plane, a three-dimensional dataset C(x, y, t) is obtained. In other words, multiple parallel B-Scans form a three-dimensional GPR data as shown in Figure 2.5-a. In this data, a horizontal slice at a certain depth (C(x, y, ti)) is called as C-Scan [29-31]. Responses of mines are represented as blobs in C-Scan data as shown in Figure 2.5-b.

(a) (b)
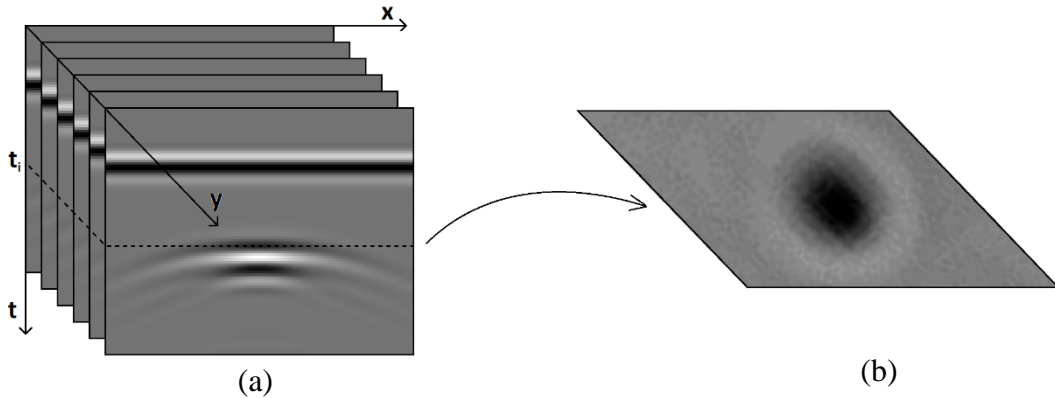
Figure 2.5. (a) Three-Dimensional GPR data, (b) A Horizontal Slice at t=t_i (C(x, y, t_i))

Line array of antennas given in Figure 2.2 can record a B-Scan data with a single measurement from all antennas. They are located along x-axis (cross-track direction) and GPR system moves along y-axis (down-track direction). Therefore, a three-dimensional GPR data is obtained as shown in Figure 2.6.
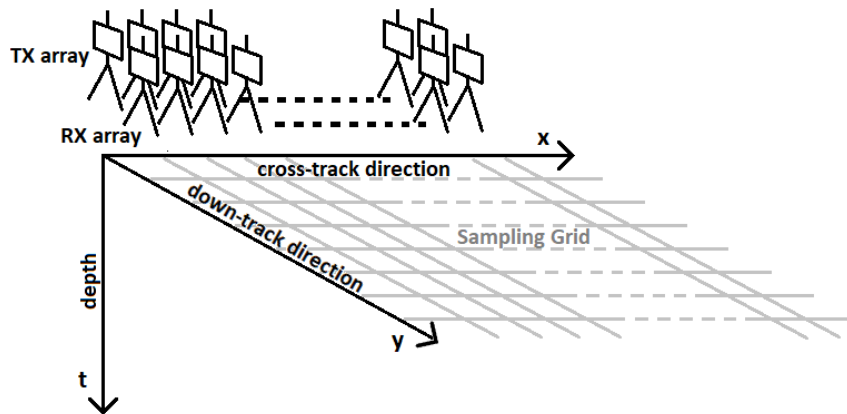
Figure 2.6. C-Scan Data Acquisition by a Line Array of Antennas

11

After collecting the GPR data, image processing techniques are applied to A, B or C-Scans for buried object detection and identification.

2.2. Current GPR-based Landmine Detection & Identification Methods

As described in the previous section, GPR uses radar pulses to image subsurface structures. However, the received raw image has to be processed for target detection. The main steps of GPR-based landmine detection process are written below:

- Ground Bounce Removal,
- Pre-screener,
- Feature Extraction,
- Classification.

2.2.1. Ground Bounce Removal

One of the most challenging features of GPR is the ground-bounce which is the initial spike in energy caused by reflected signal generated by the air ground interface. The energy of the ground-bounce is generally the highest energy peak in a GPR A-Scan as shown in Figure 2.7.
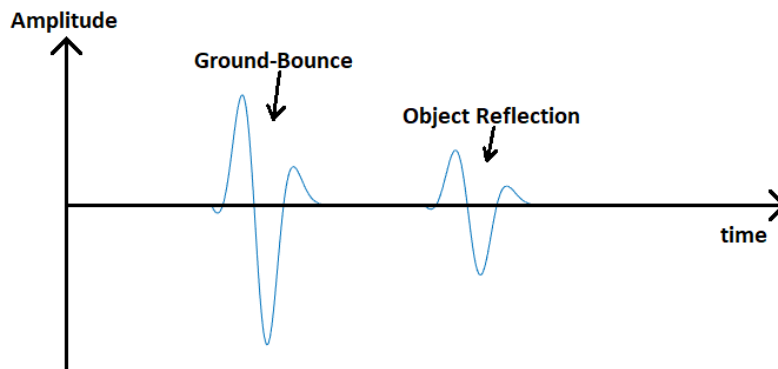
Figure 2.7. Ground Bounce and Object Reflection in an A-Scan Data

For the GPR-based landmine detection methods, false alarms are commonly generated in locations where the ground bounce is not removed properly. Hence, almost all GPR-

based algorithms use ground bounce removal techniques. Before and after the ground bounce removal of an example B-scan is shown in Figure 2.8.

(a)

(b)

Figure 2.8. (a) Raw GPR Data, (b) Ground Bounce Removed GPR Data

In the literature, there are many methods for ground-bounce removal. "Simple average operation" finds the location of the ground-bounce as the mid-point of the maximum and minimum of an A-scan [34, 35]. "Model based approach" models clutter using parametric modeling for ground-bounce removal [36-38]. "Ensemble average method" averages the time-domain signatures acquired as the antenna is scanned over the ground and subtracts that average from the data for ground-bounce removal [39, 40]. Additionally, "PCA and ICA based approach" is used for ground-bounce and clutter reduction [41-43]. Specific filtering operations (mean, median, moving median, wiener filtering) are also used for ground-bounce removal in GPR-based applications [44, 45].

2.2.2. Pre-Screener

The idea behind pre-screener algorithm is to minimize the amount of data that will be used in the feature extraction step. Therefore, complex discrimination algorithms are applied to a small subset of data to achieve real-time processing. However, all target locations should be identified by the pre-screener algorithm. Any missing target by the pre-screener is undetected by the system. Hence, a pre-screener algorithm should have very high probability of detection (almost 100%) at the expense of high false

alarm rate. These false alarms are rejected in next steps (feature extraction and classification).

In the literature, common pre-screener algorithms are Constant False Alarm Rate (CFAR) [46], Robust Principal Component Analysis (RPCA) [47], Q-Scan [48], Blob-filter [49] and Least Mean Square [50-52] algorithm.

In GPR B-Scan data, signals reflected from mines usually have high-energy contrast with respect to the background. CFAR algorithm is applied to each depth bin and measures the local contrast. Hence, high-energy locations can be identified as anomaly regions.

RPCA tries to divide a given matrix M into two matrices L and S such that M=L+S, where S is sparse and L is low-rank. In GPR B-Scan data, the anomaly regions in the subsurface are relatively sparse and the background is approximately low-rank. For a given GPR B-Scan image, RPCA detects the possible anomaly regions by finding the sparse component of B-Scan matrix.

Q-Scan is an energy-based anomaly detection algorithm such as CFAR. Differently from CFAR algorithm, Q-Scan estimates background mean and variance for each scan. Afterwards, clutter is removed from the image in the background removal step. Target signature is not removed due to its rapid gradient.

In GPR C-Scan data, the buried landmines constitute blob-like shapes as shown in Figure 2.5-b. Blob filter is a 2D Gaussian filter which is applied to each depth layer of GPR C-Scan data to detect these shapes.

To detect the possible alarm locations, LMS algorithm requires pre-processing steps such as data aligning and median filtering. Then, GPR B-Scan data is separated into statistically similar depth bins and LMS algorithm is applied to each depth bin to generate decision statistics. Afterwards, the individual depth segments are combined into a single confidence map. The confidence map is thresholded and the discrete alarm locations are generated. Finally, the specific anomaly locations are identified by using non-maximal suppression.

2.2.3. Feature Extraction

In the previous step, the possible anomaly locations are detected by a pre-screener algorithm. In this step, these anomaly regions are further processed to identify them as threats or non-threats. To achieve this, complex discrimination algorithms are applied to these locations and discriminative features are extracted. These features are used for classification. Since these complex feature extraction algorithms are applied to a small subset of data (to the result of the pre-screener algorithm), real-time processing becomes possible.

In the literature, many different feature extraction techniques are used for detection and classification of landmines in GPR data. Symmetry feature is mainly used for GPR-based landmine detection algorithms [53]. Since landmines are generally constructed such that they have high level of symmetry, classifying subsurface targets as either symmetric or asymmetric is a strong method for landmine identification.

The hyperbolic shape of GPR reflectance of a landmine is another important feature for landmine detection problems. Some studies [54, 55] use gradient magnitude as a feature to estimate the location of these hyperboles.

In recent years hidden Markov Models are very popular for GPR-based landmine detection algorithms. In the related studies [17, 56], features are the observation vectors which encode important information about the landmine signatures in a compact form. These observation vectors are then processed by the HMM to produce probabilities that certain locations have landmine.

Time-frequency domain signature analysis of GPR data is used for landmine detection in recent years [57-59]. Mostly, STFT (Short Time Fourier Transform) and WVD (Wigner Ville Distribution) of A-scans are used for feature extraction. In this method, the signal (A-scan) is first windowed (Hanning, Hamming, Kaiser, etc.) around the time of interest and then FFT is used for each window.

The application of texture features for landmine detection in GPR data is another important detection method. The 2-D texture-based approaches to the classification of

images are well-established, and application of such approaches to the problem of landmine detection is popular in recent years. The basic goal behind this technique is the translation of an intensity image to a texture feature image via differencing in the image domain followed by successive stages of vector classification [60].

Edge histogram descriptors (EHD) for feature extraction in GPR-based landmine detection algorithms are widely used in recent studies [20]. For a generic image, the EHD represents the frequency and the directionality of the brightness changes in the image. For landmine detection, the EHD is used to capture the spatial distributions of the edges within the GPR data. Since the reflection of a landmine has a characteristic shape (hyperbola), the diagonal edge, flat edge and anti-diagonal edge can be detected by EHD method.

The spectral characteristics of GPR data is used for landmine detection in some studies [61]. The motivation behind this approach comes from that landmine targets and innocuous objects often have different shapes, yielding different energy density spectrum (EDS) which may be used for their discrimination.

The pattern recognition approach is also used for GPR-based landmine detection algorithms [14]. In this approach, initially a binary image is obtained from GPR B-Scan data and the objects in the binary image are detected by means of linear/hyperbolic patterns formulated in a genetic optimization framework. In this step, the hamming distance between the corresponding pattern and the binary image content is used.

Instance matching techniques are used to extract discriminative features in GPR data. Instance matching aims to find instances of a previously trained object within a scene. It is different from template matching technique at several points. Most recent instance matching algorithms are insensitive to common types of transformations in visual images such as scale, rotation, occlusion and intensity. For a given image, instance matching techniques initially detect the areas of interest (which is called as keypoints) and then a descriptor is evaluated for these keypoints. Corner detection and blob

detection are the main keypoint identification methods. SIFT, SURF and BRIEF are most famous keypoint descriptors.

Corner detector shifts a window within an image and recognizes the intensity changes. Around a corner point, intensity changes in all directions. On a single edge or constant area, intensity difference will be low at least on one direction. Harris and Stephens propose a corner detector algorithm based on the gradients around each pixel and the sum of squared differences [62]. While corner detectors try to find corners on an image, blob detectors focus on finding areas where the intensity differs widely from surrounding area. Blob detector algorithm applies 2-D Gaussian smoothing to a given image and calculates the Hessian matrix for each pixel [63]. After one of these detectors finds the corresponding keypoints in an image, SIFT, SURF or BRIEF descriptors are evaluated around these selected pixels.

The Scale Invariant Feature Transform (SIFT) uses 16x16 patch of pixels for each feature point. Around each keypoint, pixels are divided into 4x4 sub-patches. Magnitude and angle of the gradient for each pixel are calculated. The magnitudes are normalized with respect to their distance from the corresponding keypoint using a Gaussian mask. Normalized magnitudes of the pixels are binned according to their angle's distance to eight discrete angle value that are calculated equally between 0° and 360°. Therefore, an eight-dimensional vector is obtained for each sub-patch. Since there are 16 sub-patches within a patch, 128-dimensional feature vector is constructed by concatenating the single eight-dimensional vectors from sub-patches. For a given feature point, this 128-dimensional vector represents the SIFT descriptor [64].

Speeded up Robust Features (SURF) is a faster alternative of SIFT with a comparable performance. The implementation of SURF descriptor is similar to the implementation of SIFT. SURF uses 20x20 patch of pixels for each keypoint. Within a patch, SURF creates 16 – 5x5 sub-patches. Within each sub-patch, x and y-direction gradients are calculated for each pixel by using two Haar wavelet filters. From these gradients, four statistics are calculated such that sum of x-gradients, sum of y-gradients, sum of absolute of x-gradients and sum of absolute of y-gradients. Therefore, four-

17

dimensional feature vector is constructed for each sub-patch. There are 16 sub-patches within a patch, hence 64-dimensional feature vector is extracted by concatenating the single four-dimensional vectors from sub-patches. For a given feature point, this 64-dimensional vector represents the SURF descriptor [63].

Binary Robust Independent Elementary Features (BRIEF) is another keypoint descriptor method. Unlike SIFT and SURF, BRIEF does not calculate the gradients, instead it calculates the comparisons between different locations within a patch around the keypoint. These comparisons show relative intensity changes, thus the structure within a patch. The locations used in BRIEF descriptor are chosen randomly, however the same set of locations should be used for training and testing [65].

Object detection methods are also used for GPR-based landmine detection and identification problem as well as instance matching techniques. Unlike instance matching methods which can find an identical version of a known object, object detection aims to detect instances of an object class within images. Pedestrian detection [66], face detection [67] and car detection [68] are common applications of object detection methods. The main difference between object detection and instance matching is that in object detection problem there are both transformations challenges (scale, rotation, occlusion, intensity, etc.) and uncertainty between interclass variations. Histogram of Oriented Gradients (HoG) is an example object detection method used for pedestrian detection by Dalal and Triggs [66]. This method is also used for landmine detection and identification problem in several studies [21-23].

Feature extraction and classification of targets based on the extracted features are very popular for image processing applications. Generating a robust and discriminative feature increases the classification accuracy tremendously. In this study, we also utilize this approach for landmine detection in GPR B-Scan images by proposing three new discriminative features given in Section 3.4.

2.2.4. Classification

After extracting the features, the next step is the classification of the buried objects such as landmines and non-landmines. For this issue, several classification methods are used in the literature. Sakaguchi and Pasolli [34, 69] use support vector machine while Ratto [28] uses relevance vector machine. Nuaimy and Gamba [40, 70] use neural network classification and Delbo [71] applies fuzzy clustering technique to differ landmines from innocuous objects. Kempen [45] uses bayes decision rule while Sakaguchi [69] applies partial least squares discriminant analysis (PLS-DA) and random forest method for landmine classification.

Before starting to explain classification methods, learning algorithms will be described briefly. Learning algorithms (or Machine Learning) can gain insight by observing a sample dataset and achieve data-driven predictions for a new data. To learn the discriminative characteristics of the sample dataset, learning algorithms observe the extracted features (which are described in Section 2.2.3) and tries to figure out a prediction rule as shown in Figure 2.9.
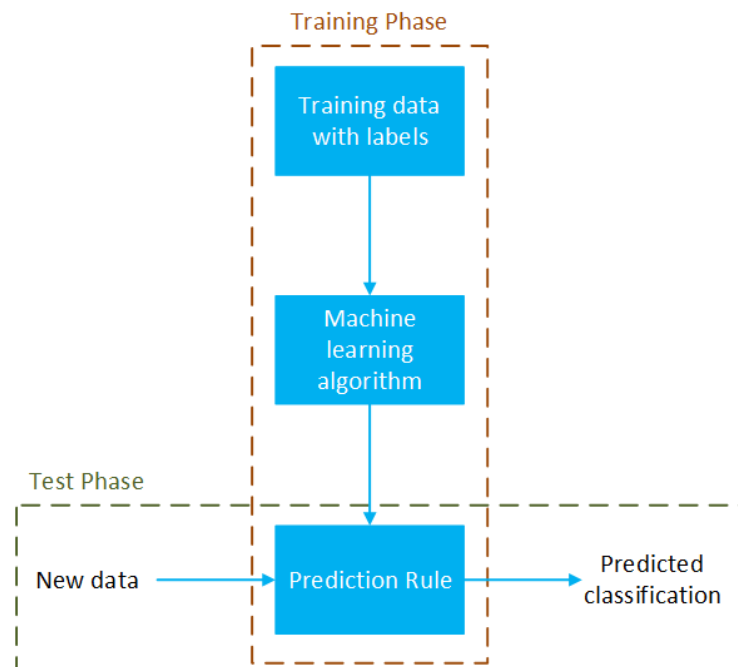
Figure 2.9. Training Phase and Test Phase of Learning Algorithms

19

Learning algorithms can be categorized into two different approaches as Supervised and Unsupervised learning. A supervised learning algorithm learns the prediction rule based on a given training dataset and their labels. On the other hand, an unsupervised learning algorithm learns the prediction rule from the input data without their labels. Hence, unsupervised learning does not have a definite result. In this study, we will focus on supervised learning algorithms that have different approaches for learning the discriminative characteristics from a training dataset and making a prediction rule. These approaches are called as Classification methods. In this section, the main Classification algorithms in the literature are described briefly.

Support Vector Machine (SVM) and Relevance Vector Machine (RVM) are two popular classification methods for hyperspectral images. For a given training data x_i and label y_i for $i \in [1, 2, ..., n]$, these two models try to classify the given data based on the input features x_i, weight vector w and bias b. If the data is not linearly solvable, each method uses Kernel functions $K(x_i, x_j)$ to make the problem linear in a higher dimensional space [72].

SVM tries to maximize the distance between decision boundary (which is called as maximum-margin hyperplane) and two classes. SVM solves the following linear model: $y = w^T x + b$ [73, 74]. If the given data and classes are not linearly separable, SVM uses kernel functions to achieve non-linear classification. Details of this issue are given in Section 3.5.

RVM applies the Bayesian principle to SVM idea. According to the following likelihood function, conditional probabilities of targets t should be maximized based on x_i and w [75-78].

$$P(t|w) = \prod_{i=1}^{n} \sigma\{y(x_i, w)\}^{t_i} [1 - \sigma\{y(x_i, w)\}]^{1-t_i}, \tag{1}$$

$$\text{where } \sigma(y) = \frac{1}{1 + e^{-y}}$$

The weights w are based on two classes of hyperparameters which are Gaussian distributed. To maximize the likelihood function in Eq. 1, these hyperparameters are optimized iteratively.

Random forest is an ensemble classification algorithm. It does not classify the given data by using its all features at once. Instead, it fits large number of simple classifiers on various subsamples of the given dataset. These classifiers are decision-trees and the entire system is known as forest [79]. Random forest is a complex algorithm and it is difficult to implement in real-time.

During classification, Partial Least Squares Discriminant Analysis (PLS-DA) Method achieves dimensionality reduction in the feature space [80, 81]. Let the input data X has dimensions nxm ($n: observations, m: features$). PLS-DA tries to project X onto a new space which has the necessary information about X with a lower dimension. This can be achieved by a transformation matrix $W: T = XW$. Here, the class labels can be represented by:

$$Y = UC^T + G, \tag{2}$$

where U is a linear function and G is the error of the model. The relation between data X and the labels Y can be found by solving C with the following equation:

$$C = (TT^T)^{-1}TY, \tag{3}$$

K-Nearest Neighbor (KNN) classifier is generally based on Euclidean distance between the training samples and a given test sample. Let the input data X has dimensions nxm ($n: observations, m: features$). i^{th} sample x_i has m features: $(x_{i,1}, x_{i,2}, ..., x_{i,m})$. Euclidean distance between i^{th} sample and j^{th} sample can be calculated by the following formula:

$$d(x_i, x_j) = \sqrt{(x_{i,1} - x_{j,1})^2 + \cdots + (x_{i,m} - x_{j,m})^2}, \tag{4}$$

For a given test sample, Euclidean distance between this sample and all training samples are calculated. Majority label of K-nearest training samples indicates the class label of the given test sample [82-84].

Fuzzy clustering, which is generalization of partition clustering methods, allows classification into multiple clusters. Let we have k clusters and the variables $(p_{i,1}, p_{i,2}, \ldots, p_{i,k})$ represent the probabilities such that $p_{i,j}$ is the probability of data x_i belongs to cluster j. Here, $p_{i,j}$ should be between 0 and 1; sum of the probabilities $(p_{i,1} + p_{i,2} + \ldots + p_{i,k})$ should be 1. Fuzzy clustering algorithm tries to minimize the following function [85, 86]:

$$C = \sum_{a=1}^{k} \frac{\sum_{i=1}^{n} \sum_{j=1}^{n} p_{i,a}^2 p_{j,a}^2 d(x_i, x_j)}{2 \sum_{j=1}^{n} p_{j,a}^2}, \tag{5}$$

Where $d(x_i, x_j)$ represents the dissimilarity between data x_i and x_j. Euclidean distance is generally used for dissimilarity function.

Bayes Decision Rule, which is also called as Naive Bayes Theorem, is a classification method based on Bayes' Theorem as its name implies. This technique assumes two types of probabilities which is calculated from the training data: probability of each class and conditional probability of each class given each input data x. After these probabilities are calculated, the model is used to estimate the class label of new input data using Bayes' Theorem [87, 88].

Up to this point, the classification algorithms, which process the extracted features of the input data (not the input data itself), have been presented. Neural Networks are also considered as a robust classifier. Unlike previous ones, neural networks process the input data itself (not the extracted features). The idea has arisen from the fascination of human brain and understanding of mankind. Therefore, neural networks consist of units (like neurons in human neural system) that convert an input data x into an output y. These units are arranged in layers such that each unit in a specific layer takes the input, performs a non-linear function and passes the output to the next layer.

When the data passes from one unit to the next one, weightings are applied. During the training phase, these weightings are tuned to learn the algorithm [89, 90].

2.3. Methods Utilized in this Thesis

In this section, we will describe the techniques, which are available in the literature and we have utilized in the proposed algorithm, in detail. Summary of these techniques were briefly given in Section 2.2. This section does not include our proposed method which will be given in Section 3.

2.3.1. Maximum Detection Technique for Ground Bounce Removal

In a GPR B-Scan data, ground bounce usually dominates the rest of the image as shown in Figure 2.8-a. By using this phenomenon, location of the ground bounce can be detected by finding the maximum of each scan as proposed in [91]. However, this idea is not always correct. If dielectric properties of soil are close to the dielectric properties of air and there is a highly conductive target underground, amplitude of the primary reflection coming from the target may be higher than the amplitude of the ground bounce. So, in this study we have adopted the maximum detection technique proposed in [91] with some modifications for ground bounce removal.

For a GPR system, height of the radar antenna from the ground is known before starting landmine sweeping. However, a vehicle mounted GPR cannot maintain the antenna at a fixed height. So, location of the ground bounce may change from scan to scan due to up-down movement of GPR antenna. Based on these movements, maximum and minimum height of GPR antenna can be estimated, therefore the ground bounce is located within a predictable range. In this study, we find the maximum value of the signal within this range to detect the position of the ground bounce. Thus, we avoid to mis-detect a higher reflection, which is coming from a buried object deeper in the ground, as ground bounce.

During the experiments, height of the GPR antenna is 16 cm above the ground. For this configuration, the ground bounce is approximately located between time samples

400 and 700 as shown in Figure 2.10. In the given A-Scan data in Figure 2.10, the maximum value belongs to primary reflection is around time sample 1000. If the proposed method in [91] is applied directly, the location of the ground bounce is mis-detected. To avoid this issue, we select a predictable region for the position of ground bounce. For this example, this region is between time samples 400 and 700. However, this is the case when the GPR antenna is exactly 16 cm above the ground. To compensate up-down movement of the antenna, we choose this region as between time samples 200 and 900. Therefore, during the experiments, height of the GPR antenna is 16 cm and we detect the position of the ground bounce by finding the maximum value of the signal between time samples 200 and 900.
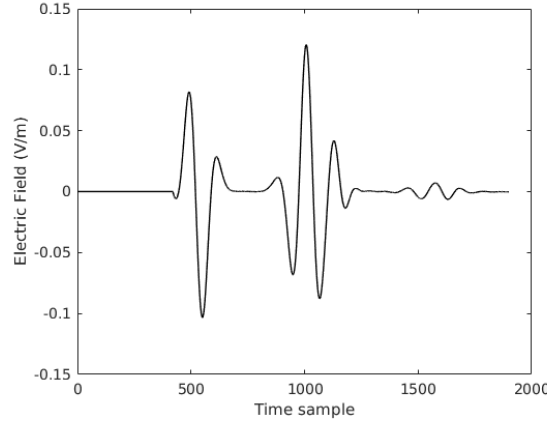
Figure 2.10. Positions of Ground Bounce and Primary Reflection

After maximum detection, each A-Scan data is aligned and L time samples after the ground bounce peak are removed. L should be chosen as the duration of ground bounce in time. For our example in Figure 2.10, L is around 300-time samples. Theoretically, ground bounce removal process is summarized below:

$For\ every\ x, Do$

$$t_i = argmaxB(x,t)\ for\ 200 < t < 900$$

$$B^*(x,t) = B(x, t + t_i + L)$$

End

24

2.3.2. Least Mean Squares (LMS) Approach for Pre-screener

The working principle of this approach is based on an adaptive filter using the least mean squares method. LMS algorithm adjusts the filter coefficients (weights) for each new sample of the input data. For each selected window, LMS finds the differences from the background by adaptively updating the filter coefficients [50-52].

Since the targets which are buried deeper have weak GPR response with respect to shallowly buried targets, LMS algorithm tends to remove the response of deeply buried targets. To avoid this issue, B-Scan image is normalized to enhance the deeper region of data. To achieve this, each row of ground bounce removed B-Scan image is normalized before LMS algorithm. An example B-Scan image before and after normalization is shown in Figure 2.11.

(a)   (b)
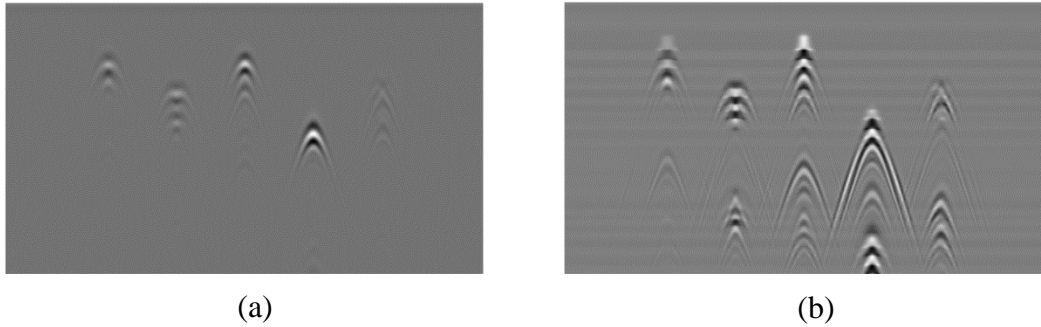
Figure 2.11. (a) B-Scan Image Before Normalization, (b) B-Scan Image After Normalization

After normalization, LMS algorithm is applied with a sliding window to B-Scan image. This window can be rectangular (2D LMS) or one dimensional (1D LMS). The working principle of 1D LMS and 2D LMS are similar and a brief review is presented here. At time n, assume our point of interest is d_n. Consider a weight vector w_n and an input vector u_n. The LMS algorithm performs like below:

$$output\ at\ time\ n: y_n = w_n^T * u_n$$

$$error\ at\ time\ n: e_n = d_n - y_n$$

$$updated\ weight\ vector: w_{n+1} = w_n + \mu * u_n * e_n$$

In this formula μ is the scaling factor which determines the update ratio of the weight vector.

1D LMS algorithm is applied to each column of B-Scan image separately. Consider a point of interest at the xth column of B-Scan image. For the corresponding point d_n, a guard-band data selection mask is used and the data selected by this mask gives the input u_n. 1D data selection mask for an example scenario, such that the filter length is 12 and guard band length is 5, is shown in Figure 2.12. In the figure, d_n is denoted by square and u_n is the input vector that consists of circles and has length 12.
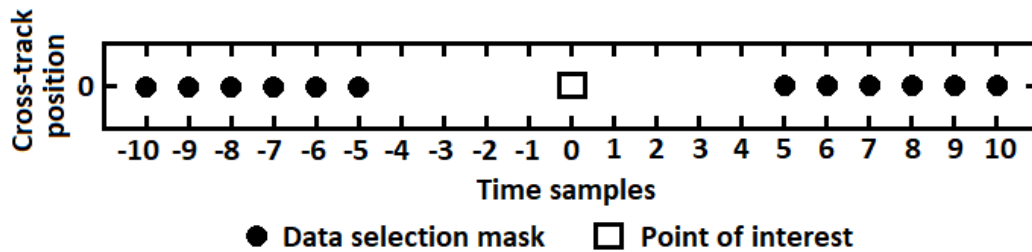
Figure 2.12. 1D LMS Data Selection Mask

After applying the given 1D mask to the B-Scan image, if we draw the error values e_n for all time samples and for all cross-track positions, the pre-screener image shown in Figure 2.13 is obtained. Here, μ is chosen as 0.01 and the initial value of weight vector is chosen as $w_0 = [\frac{1}{12}, \frac{1}{12}, \frac{1}{12}, \frac{1}{12}, \frac{1}{12}, \frac{1}{12}, \frac{1}{12}, \frac{1}{12}, \frac{1}{12}, \frac{1}{12}, \frac{1}{12}, \frac{1}{12}]$.
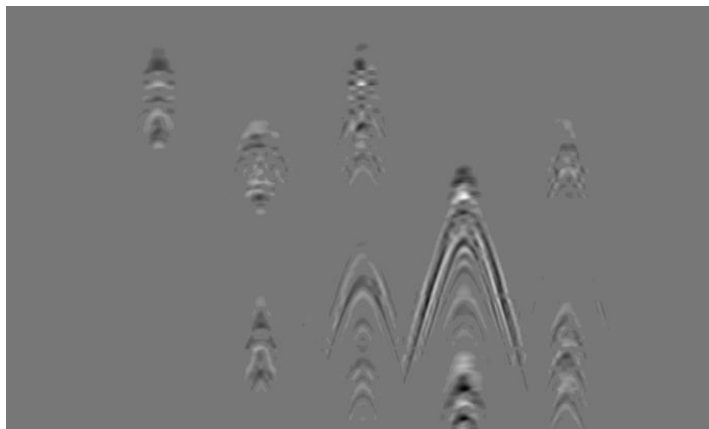
Figure 2.13. 1D LMS Result – Pre-screener Image

Afterwards, if the pre-screener image is thresholded, a binary image is obtained as given in Figure 2.14. Here, absolute value of each pixel is thresholded at the value 0. From the binary image, the possible anomaly regions can be detected.
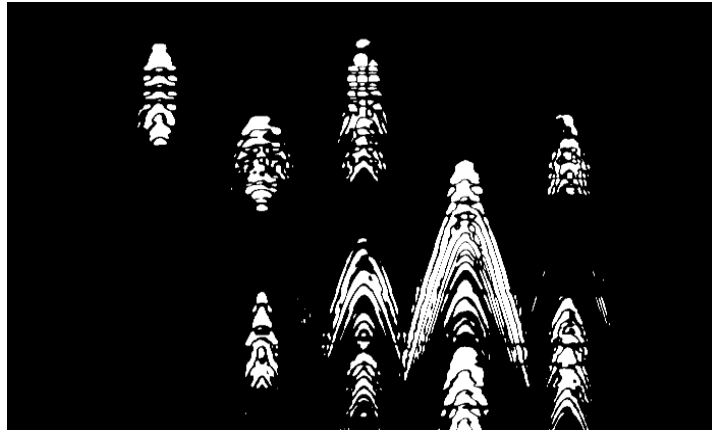
Figure 2.14. 1D LMS Result – Binary Image

Although 1D LMS algorithm is applied to each column separately, 2D LMS algorithm is applied in both cross-track (x) and depth (z) directions. To achieve this, a 2D guard-band data selection mask is used and the data selected by this mask gives the input u_n. 2D data selection mask for an example scenario, such that 11x6 filter is used with guard band length is 3 in cross-track direction, is shown in Figure 2.15. In the figure, d_n is denoted by square and u_n is the input vector that consists of circles and has length 66.
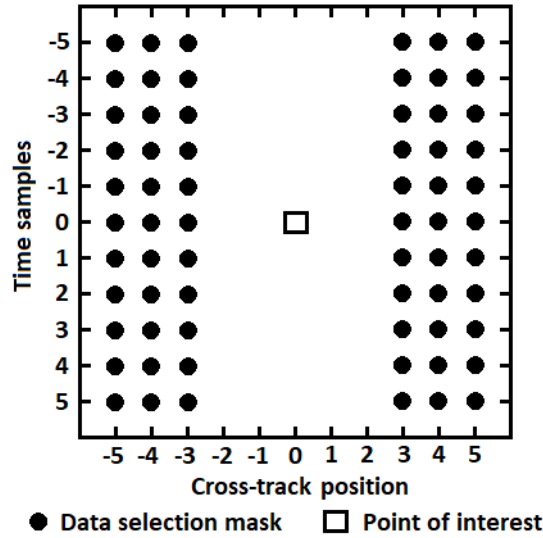
Figure 2.15. 2D LMS Data Selection Mask

After applying the given 2D mask to the B-Scan image, if we draw the error values e_n for all time samples and for all cross-track positions, the pre-screener image shown in Figure 2.16 is obtained. Here, μ is chosen as 0.01 and the initial value of weight vector is chosen as $w_0 = [\frac{1}{66}, \frac{1}{66}, \dots, \frac{1}{66}]$.
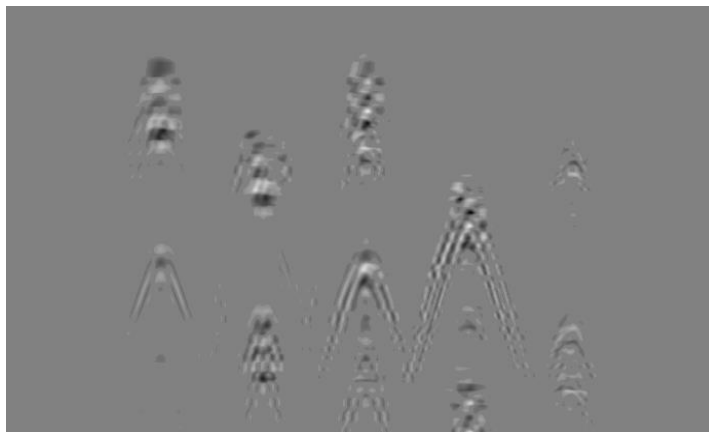
Figure 2.16. 2D LMS Result – Pre-screener Image

Afterwards, if the pre-screener image is thresholded, a binary image is obtained as given in Figure 2.17. Here, absolute value of each pixel is thresholded at the value 0. From the binary image, the possible anomaly regions can be detected.

28

Figure 2.17. 2D LMS Result – Binary Image

From the binary image given in Figure 2.14 or 2.17, the possible anomaly regions can be detected by using the binary mapping of the projection of each column as described in Section 3.2.

2.3.3. Gradient-based Algorithm

In this study, gradient-based algorithm is utilized to find the center of an anomaly region. In reference studies [17, 56], for a given B-Scan image observation vectors are created for each cross-track position. These observation vectors show the degree of edges in the diagonal and anti-diagonal directions. The transition region from diagonal to anti-diagonal edges corresponds to the center of the underground target.

Gradient-based algorithm works as follows. Assume the given ground bounce removed raw image, which is shown in Figure 2.18, is denoted by $S(x, z)$.

Figure 2.18. Ground Bounce Removed Raw Image

29

Initially, second derivative of the given raw image is calculated by Eq. 6 and Eq. 7. This process removes stationary effects and enhances the edges as shown in Figure 2.19.

$$S^{l}(x,z) = \frac{[S(x+2,z)+2S(x+1,z)-2S(x-1,z)-S(x-2,z)]}{3}, \quad (6)$$

$$S^{ll}(x,z) = \frac{[S^{l}(x+2,z)+2S^{l}(x+1,z)-2S^{l}(x-1,z)-S^{l}(x-2,z)]}{3}, \quad (7)$$
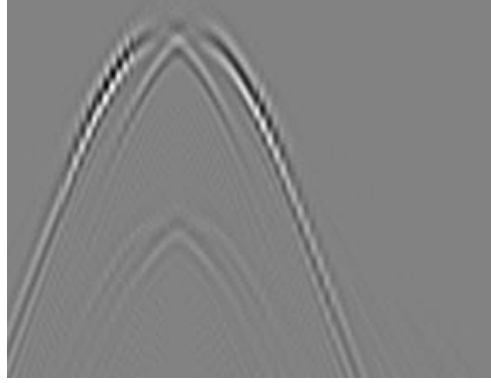
Figure 2.19. Second Derivative of the Given Raw Image

Afterwards, the derivative values are normalized along x direction by Eq. 8-10. Normalization enhances the deeper region of the GPR image, hence all depth segments have similar contrast in the normalized image as shown in Figure 2.20.

$$\mu(z) = mean_x(S^{ll}(x,z)), \quad (8)$$

$$\sigma(z) = standard\_dev_x(S^{ll}(x,z)), \quad (9)$$

$$N(x,z) = \frac{S^{ll}(x,z)-\mu(z)}{\sigma(z)}, \quad (10)$$
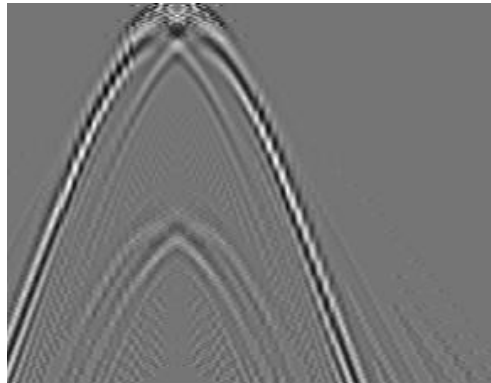
Figure 2.20. Normalized Second Derivative

30

The gradient-based algorithm proposes to create positive and negative parts of the normalized second derivative by Eq. 11 and Eq. 12. These positive and negative parts correspond to bright and dark areas respectively as shown in Figure 2.21.

$$N^+(x,z) = \{ \begin{matrix} N(x,z), & if\ N(x,z) > 1 \\ 0, & else \end{matrix}, \quad (11)$$

$$N^-(x,z) = \{ \begin{matrix} -N(x,z), & if\ N(x,z) < -1 \\ 0, & else \end{matrix}, \quad (12)$$

(a)   (b)
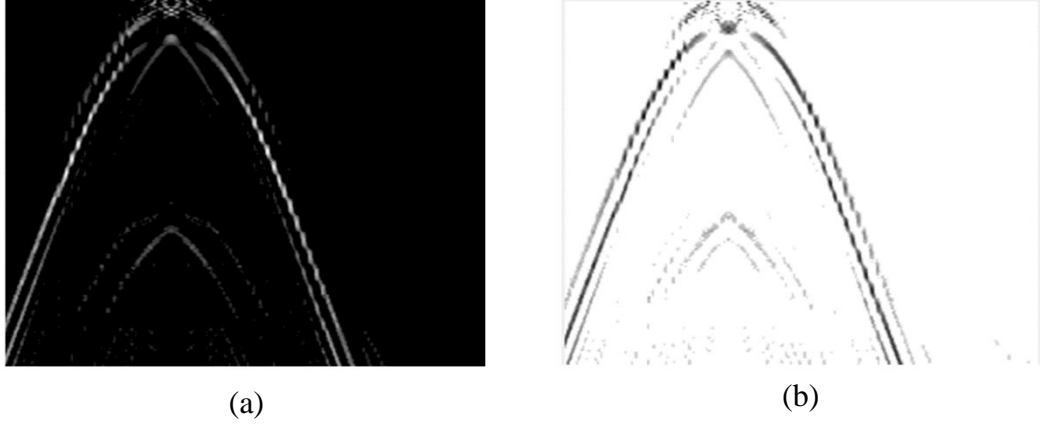
Figure 2.21. (a) Positive Image, (b) Negative Image

Then, for each point in the positive image and negative image given in Figure 2.21, the strengths of diagonal (45° direction) and anti-diagonal (135° direction) edges are calculated by Eq. 13-16.

$$PA(x,z) = \min\{N^+(x,z-1), N^+(x+1,z), N^+(x+2,z+1), N^+(x+3,z+2)\}, \quad (13)$$

$$NA(x,z) = \min\{N^-(x,z-1), N^-(x+1,z), N^-(x+2,z+1), N^-(x+3,z+2)\}, \quad (14)$$

$$PD(x,z) = \min\{N^+(x,z+2), N^+(x+1,z+1), N^+(x+2,z), N^+(x+3,z-1)\}, \quad (15)$$

$$ND(x,z) = \min\{N^-(x,z+1), N^-(x+1,z+1), N^-(x+2,z), N^-(x+3,z-1)\}, \quad (16)$$

Afterwards, for each cross-track position x, we find the location z of the maximum value in PA, NA, PD and ND matrices. Assume the total number of rows is "n" for the raw image given in Figure 2.18. So, position of the maximum values can be found by Eq. 17-20.

$$m_{pa}(x) = argmax\{PA(x,z): z = 1,2,\dots,n\}, \quad (17)$$

$$m_{na}(x) = argmax\{NA(x,z): z = 1,2,\dots,n\}, \quad (18)$$

$$m_{pd}(x) = argmax\{PD(x, z): z = 1, 2, \ldots, n\}, \quad (19)$$

$$m_{nd}(x) = argmax\{ND(x, z): z = 1, 2, \ldots, n\}, \quad (20)$$

Finally, for each cross-track position 16-dimensional observation vector is obtained by Eq. 21.

$$O(x) = (o_1(x), o_2(x), \ldots, o_{16}(x)), \quad (21)$$

$$o_1(x) = PD(x, m_{pd}(x) - 2) \qquad o_9(x) = PA(x, m_{pa}(x) - 2)$$

$$o_2(x) = PD(x, m_{pd}(x)) \qquad o_{10}(x) = PA(x, m_{pa}(x))$$

$$o_3(x) = PD(x, m_{pd}(x) + 2) \qquad o_{11}(x) = PA(x, m_{pa}(x) + 2)$$

$$o_4(x) = PD(x, m_{pd}(x) + 4) \qquad o_{12}(x) = PA(x, m_{pa}(x) + 4)$$

$$o_5(x) = ND(x, m_{nd}(x) - 2) \qquad o_{13}(x) = NA(x, m_{na}(x) - 2)$$

$$o_6(x) = ND(x, m_{nd}(x)) \qquad o_{14}(x) = NA(x, m_{na}(x))$$

$$o_7(x) = ND(x, m_{nd}(x) + 2) \qquad o_{15}(x) = NA(x, m_{na}(x) + 2)$$

$$o_8(x) = ND(x, m_{nd}(x) + 4) \qquad o_{16}(x) = NA(x, m_{na}(x) + 4)$$

In the observation vector, the first quadruple shows the strength of positive diagonal edge, the second quadruple shows the strength of negative diagonal edge, the third quadruple shows the strength of positive anti-diagonal edge and the last quadruple shows the strength of negative anti-diagonal edge. Therefore, by observing the index of the observation vector at a specific cross-track position, we can estimate the edge direction in this region.

B-Scan image of an underground target has "only diagonal", "both diagonal and anti-diagonal" and "only anti-diagonal" edges consecutively as shown in Figure 2.22.

Figure 2.22. Diagonal Edge / Both Diagonal and Anti-Diagonal Edges / Antidiagonal Edge Regions

If the observation vectors belong to the image given in Figure 2.22 are calculated from left of the image to the right part, three different types of observation vectors are obtained as given in Figure 2.23.

(a)

(b)

(c)

(d)

(e)
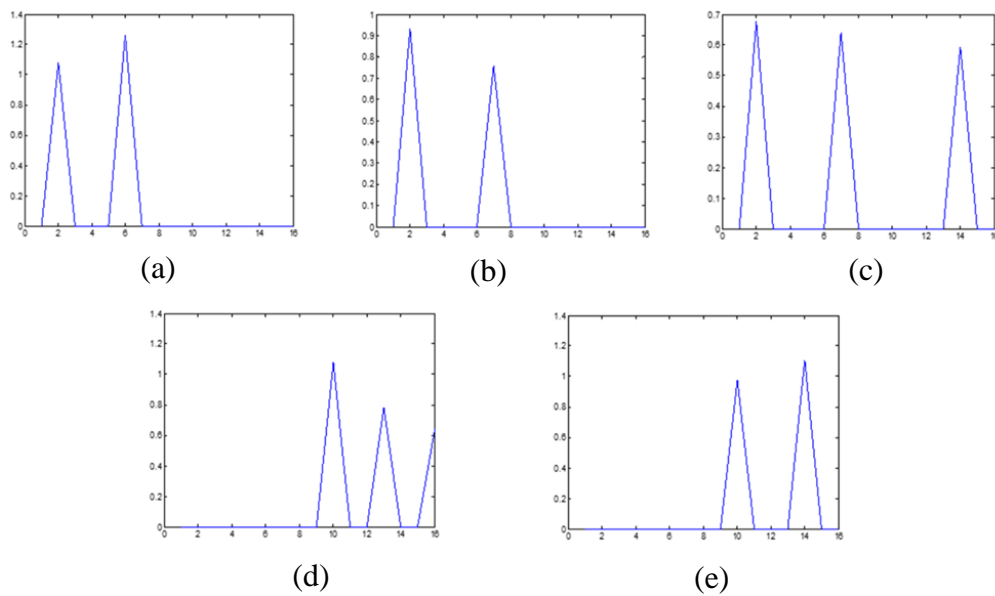
Figure 2.23. (a-b) Type-I Observation Vectors, (c) Type-II Observation Vector, (d-e) Type-III Observation Vectors

In this study, the gradient-based algorithm is used to find the center of the underground target. As explained above, Type-II observation vector belongs to the transition region from diagonal to anti-diagonal edges. This region corresponds to the center of the

33

buried object. To localize this center point, we utilize the gradient-based approach and find the position of the Type-II observation vectors. If, there are multiple observation vectors belong to the transition region, the A-Scan data which has the highest amplitude is chosen as the center part.

2.3.4. Histogram of Oriented Gradients (HoG) Feature Extraction

In this study, performance of the proposed algorithm, which is explained in Section 3, is compared with two well-known image-based feature extraction methods that are Histogram of Oriented Gradients (HoG) and Edge Histogram Descriptors (EHD) feature extraction methods. Therefore, in this and the next section HoG and EHD methods are explained respectively.

To extract HoG feature descriptor from GPR B-Scan image, Torrione et. al. explains the algorithm as follows [22]. Initially, the ground bounce removed raw GPR data is resampled to 18 x 24 pixels as shown in Figure 2.24.

(a)   (b)
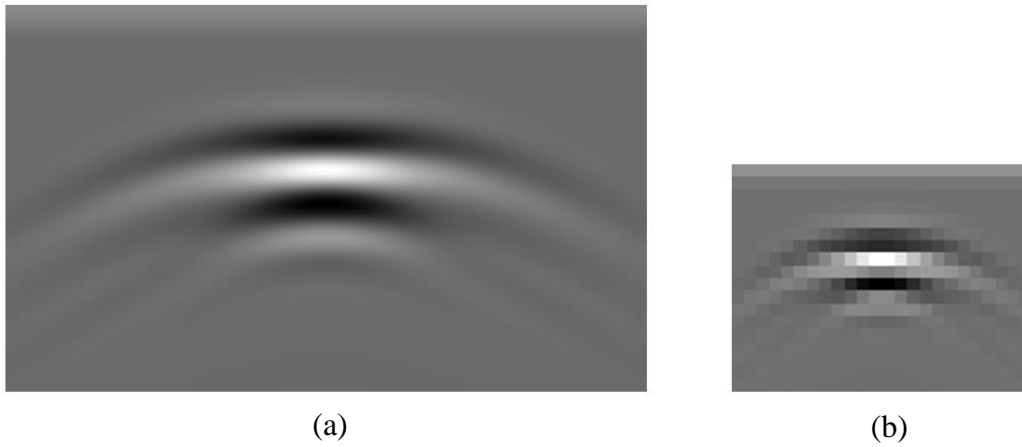
Figure 2.24. (a) Original Raw Image, (b) Resampled Image

The resampled image is divided into 3x4 cells and each cell contains 6x6 pixels. HoG features are extracted from two overlapping blocks such that each block consists of 3x3 cells as shown in Figure 2.25.
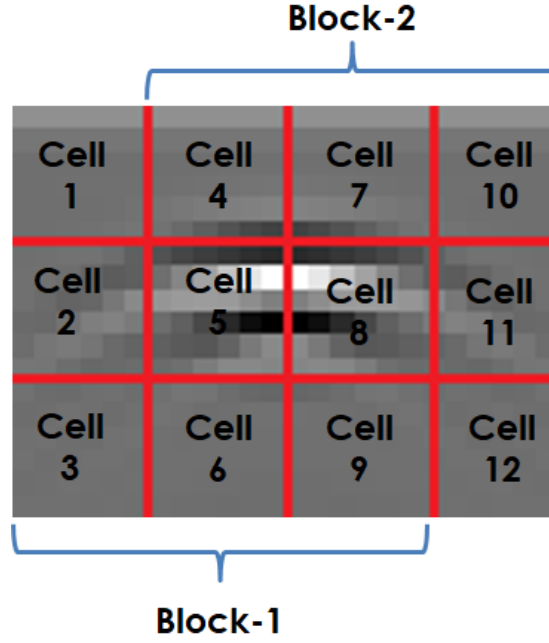
Figure 2.25. HoG Cells and Blocks of Resampled Image

For each cell, histogram of oriented gradient values of the pixels are calculated. Torrione et. al. suggests using nine unique histogram bins equally spaced in the range [0, π]. To calculate the histogram, horizontal and vertical derivatives of each cell are computed. Let, I is the corresponding 6x6 cell. Then, the derivatives are computed by Eq. 22 and Eq. 23.

$$I_x = I * g_x, \tag{22}$$
$$I_y = I * g_y, \tag{23}$$
$$\text{where } g_x = [-1\ 0\ 1]\ and\ g_y = [-1\ 0\ 1]^T,$$

Then, magnitude and angle of each pixel are computed in the corresponding cell by Eq. 24 and Eq. 25.

$$G(i,j) = \sqrt{I_x(i,j)^2 + I_y(i,j)^2}, \tag{24}$$
$$A(i,j) = arctan\frac{I_y(i,j)}{I_x(i,j)}, \tag{25}$$

Gradient value of each pixel contributes two histogram bins such that angle value of this pixel is between these two histogram bins. The contribution is inversely proportional with the distance between the angle value and the corresponding

35

histogram bins. For example, if the gradient and the angle of a pixel is 9 and 30° respectively, one-third of the gradient value contributes the histogram bin "45°" and two-thirds of the gradient value contribute the histogram bin "22.5°". If the angle of a pixel is exactly equal to a histogram bin, the entire gradient value contributes this bin.

For each cell, gradient and angle values of 36 pixels are calculated and one histogram is created with length 9. Let, $H(c_i, k)$ denotes the histogram of cell-i for $k = 1, 2, \dots, 9$. For the first block (in Figure 2.25), histograms of nine cells (from cell-1 to cell-9) are concatenated together and normalized to obtain 81-dimensional feature descriptor (H_1) by Eq. 26.

$$H_1 = \frac{[H(c_1), \ H(c_2), \ \dots, \ H(c_9)]}{\sum_{i=1}^{9} \sqrt{\|H(c_i)\|_2^2}}, \tag{26}$$

For the second block, the same operation is performed to achieve 81-dimensional feature descriptor (H_2) by Eq. 27.

$$H_2 = \frac{[H(c_4), \ H(c_5), \ \dots, \ H(c_{12})]}{\sum_{i=4}^{12} \sqrt{\|H(c_i)\|_2^2}}, \tag{27}$$

Finally, these two vectors (H_1 and H_2) are concatenated to obtain the final 162-dimensional HoG feature descriptor. The visualization of HoG feature vectors of the image given in Figure 2.24 is shown in Figure 2.26.
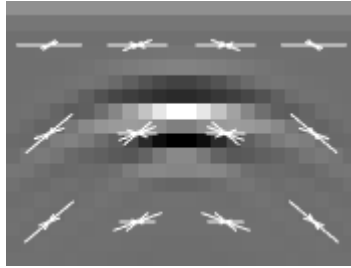
Figure 2.26. Visualization of HoG Feature Vectors

2.3.5. Edge Histogram Descriptor (EHD) Feature Extraction

In this section, Edge Histogram Descriptor (EHD) feature extraction method is explained briefly. To extract EHD feature descriptor from GPR B-Scan image, Frigui

et. al. explains the algorithm as follows [20]. Although HoG feature extraction algorithm resizes the raw image into a lower dimension, EHD method performs on the original raw image. B-Scan image is vertically subdivided into seven overlapping sub-images as shown in Figure 2.27. In this example, we use 50% overlapping.
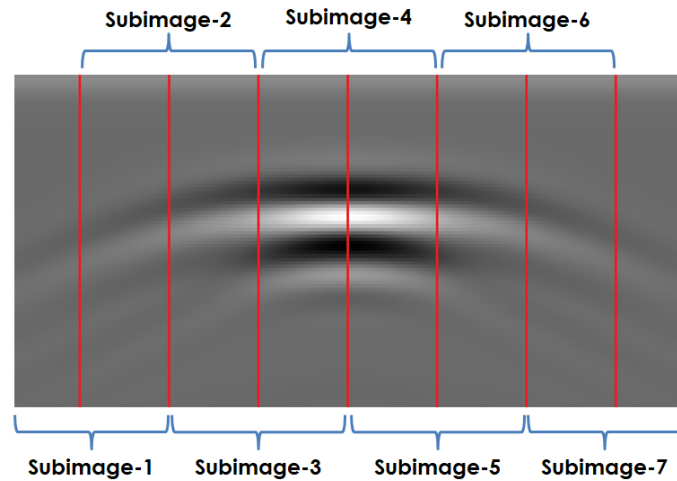
Figure 2.27. EHD Subimages

For each sub-image, histogram values are computed in a similar way of HoG algorithm. Different from HoG feature extraction method, five unique histogram bins equally spaced in the range $[0, \pi]$ are used. These 5-bin histogram vectors are concatenated together to obtain 35-dimensional EHD feature descriptor. The visualization of EHD feature vectors of the image given in Figure 2.27 is shown in Figure 2.28.
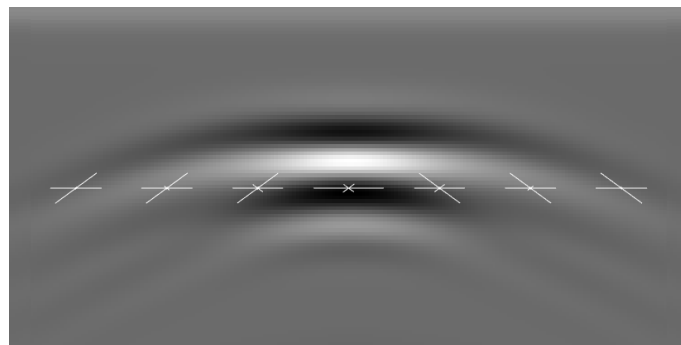
Figure 2.28. Visualization of EHD Feature Vectors

2.3.6. Support Vector Machine (SVM) Classification

In this study, we have applied two-class Support Vector Machine (SVM) algorithm to classify landmines and innocuous objects. In this section, the basic working principle of SVM algorithm is described for linearly separable case and linearly non-separable case.

If we have linearly separable two classes as shown in Figure 2.29, SVM tries to find a hyperplane (decision boundary) which satisfies the equation $w^T x + b = 0$ [73, 74]. Any data point (x_i) above this decision boundary belongs to the first class $(y_i = 1)$ and any data point (x_i) below this decision boundary belongs to the second class $(y_i = -1)$. This output labelling provides the decision function given in Eq. 28.

$$f(x) = sign(w^T x + b), \qquad (28)$$

According to the decision function given in Eq. 28, the classification result can be checked by Eq. 29.

$$y(w^T x + b) \geq 0, \qquad (29)$$
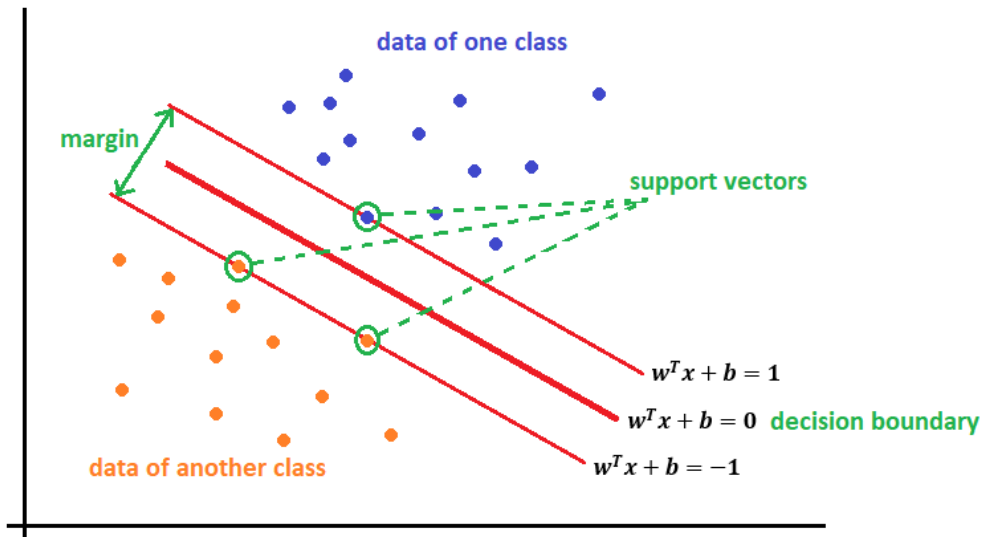
Figure 2.29. Linearly Separable Two Classes

38

In Figure 2.29, there is a space between the decision boundary and the nearest data points (which are called as support vectors) of the classes. So, we can regenerate the classification rule as any data point (x_i) above $w^T x + b = 1$ belongs to the first class $(y_i = 1)$ and any data point (x_i) below $w^T x + b = -1$ belongs to the second class $(y_i = -1)$. According to this definition, there is a distance between the two boundaries. Firstly, these boundaries are parallel since they have the same w and b parameters. If we pick a point x_1 on line $w^T x + b = -1$, the closest point on line $w^T x + b = 1$ to x_1 is the point $x_2 = x_1 + \lambda w$. So, the distance between x_1 and x_2, which is the shortest distance between two boundaries, is $\lambda \|w\|$. If we solve the equations for λ, Eq 30-35 are obtained.

$$w^T x_2 + b = 1, \tag{30}$$

$$w^T (x_1 + \lambda w) + b = 1, \tag{31}$$

$$w^T x_1 + b + \lambda w^T w = 1, \tag{32}$$

$$-1 + \lambda w^T w = 1, \tag{33}$$

$$\lambda w^T w = 2, \tag{34}$$

$$\lambda = \frac{2}{w^T w} = \frac{2}{\|w\|^2}, \tag{35}$$

According to Eq. 35, the distance between two boundaries is $\lambda w = \frac{2}{\|w\|} = \frac{2}{\sqrt{w^T w}}$. SVM algorithm tries to maximize this distance, thus the data points from different classes lie as far away from each other as possible. To maximize $\frac{2}{\sqrt{w^T w}}$, we should minimize $w^T w$. So, the quadratic problem to be solved by SVM can be expressed by Eq. 36.

$$argmin_{w,b} w^T w \text{ such that } y_i(w^T x_i + b) \geq 1 \; \forall i \in \{1, 2, \ldots, n\}, \tag{36}$$

Soft margin extension of SVM algorithm allows some data points of one class to appear on the other side of decision boundary. If we cannot guarantee that all data points are labelled correctly, we can use soft margin extension as given in Eq. 37. ϵ_i is a non-negative slack variable for each x_i.

$$argmin_{w,b,\epsilon} w^T w + C \sum_i \epsilon_i \ such\ that\ y_i(w^T x_i + b) \geq 1 - \epsilon_i, \qquad (37)$$

If the data points belong to different classes are not linearly separable, special kernel functions ($\emptyset(x)$) can be used to map data vectors (x_i) into a higher-dimensional space in which new data vectors ($\emptyset(x_i)$) are linearly separable. In this case, the quadratic problem to be solved by SVM can be expressed by Eq. 38. An example kernel mapping is shown in Figure 2.30. The linearly non-separable data (in Figure 2.30-a) is mapped into a higher dimensional space in which the new data vectors are linearly separable as given in Figure 2.30-b.

$$argmin_{w,b,\epsilon} w^T w + C \sum_i \epsilon_i \ such\ that\ y_i(w^T \emptyset(x_i) + b) \geq 1 - \epsilon_i, \qquad (38)$$
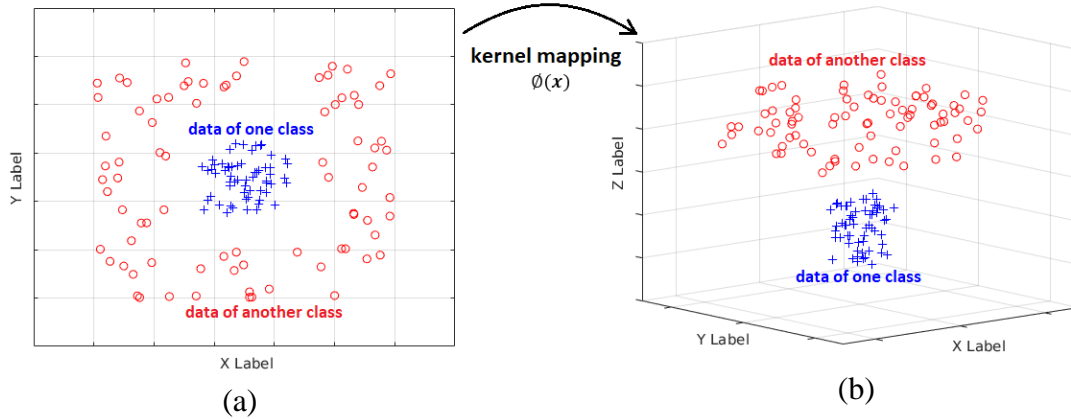
Figure 2.30. (a) Linearly Non-separable Data, (b) Linearly Separable Data

2.4. Reflection and Propagation Theory of Electromagnetic Signals

As explained in the Introduction part, in this study our aim is to combine physics-based approach with image-based techniques to increase the discrimination performance of the final GPR-based landmine detection algorithm. Physics-based techniques that will be utilized in this study are subject to widely accepted theoretical foundations and formulations. In this section, the underlying electromagnetic formulations, which show the relationship between the physics-based features and the electromagnetic properties of the soil and the buried object, are explained.

2.4.1. Reflection and Transmission of Electromagnetic Signal at the Interface between Two Different Dielectrics

Any medium through which electromagnetic wave propagates have a property called as intrinsic impedance (η). The relation between intrinsic impedance (η) and reflection coefficient (Γ) which can be calculated by GPR measurement is explained below.

For a general medium with permittivity, permeability and conductivity given by $(\epsilon, \mu, \sigma) = (\epsilon_r \epsilon_0, \mu_r \mu_0, \sigma)$, the intrinsic impedance can be calculated by Eq. 39 at a given frequency ω [92-94]. Here, ϵ_r is the relative permittivity, μ_r is the relative permeability and σ is the conductivity of the medium. ϵ_0 and μ_0 are permittivity and permeability of free space.

$$\eta = \sqrt{\frac{j\omega\mu}{\sigma + j\omega\epsilon}} = \sqrt{\frac{\mu}{\epsilon}}(1 - j\frac{\sigma}{\omega\epsilon})^{-1/2}, \tag{39}$$

A lossy medium ($\sigma \neq 0$) is said to be low-loss if $\frac{\sigma}{\omega\epsilon} \ll 1$. A low-loss dielectric is a good but imperfect insulator with a nonzero equivalent conductivity [90]. Practically, a dielectric is accepted as low-loss if $\sigma < \frac{\omega\epsilon}{10}$. Assuming that we are working in a low-loss condition, Eq. 39 becomes [92]:

$$\eta \cong \sqrt{\frac{\mu}{\epsilon}}\left(1 + j\frac{\sigma}{2\omega\epsilon}\right), \tag{40}$$

$$\text{where} \quad Re\{\eta\} = \sqrt{\frac{\mu}{\epsilon}} \quad \text{and} \quad Im\{\eta\} = \frac{\sigma}{2\omega\epsilon}\sqrt{\frac{\mu}{\epsilon}}$$

Within the operating frequency of current GPR systems (800 MHz – 4 GHz) [97] and the dielectric properties of common soil types ($\mu_r \cong 1$, $4.5 < \epsilon_r < 10$, $0.1\ mS/m < \sigma < 15\ mS/m$) [95, 96], the working medium can be assumed as low-loss. If the dielectric properties of soil in the experimental area are beyond these ranges (due to moisture or clay content), operating frequency of GPR should be adjusted appropriately.

When an electromagnetic wave passes from one medium to another medium with different intrinsic impedance, a fraction of its energy is reflected and the remainder is transmitted through the interface. In terms of the intrinsic impedances, reflection (Γ) and transmission (τ) coefficients can be calculated as given in Eq. 41 [92]. Note that, in Eq. 41 η_1 and η_2 are relative intrinsic impedance values of the mediums, since $\eta_0 = \sqrt{\frac{\mu_0}{\epsilon_0}}$ (intrinsic impedance of vacuum) is cancelled out from numerator and denominator.

$$\Gamma = \frac{E_r}{E_i} = \frac{\eta_2 - \eta_1}{\eta_2 + \eta_1} \quad \text{and} \quad \tau = \frac{E_t}{E_i} = \frac{2\eta_2}{\eta_2 + \eta_1}, \tag{41}$$

During GPR measurement, GPR antenna is positioned at a certain height from ground surface as shown in Figure 2.31. The underground target is located at an unknown depth.
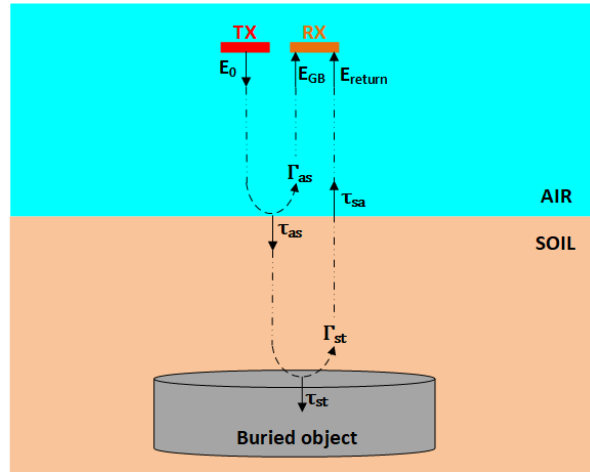
Figure 2.31. Reflection and Transmission at the Air-Soil Boundary

Please observe the reflection and transmission of GPR signal at the air-soil boundary in Figure 2.31. In the figure, a reflection coefficient (Γ_{as}) and a transmission coefficient (τ_{as}) are used to describe the amplitude of the reflected wave (E_r) and the transmitted wave (E_t) relative to the amplitude of the incident wave (E_i). In this scenario, $E_i = E_0$, $E_r = E_{GB}$ and E_t is the transmitted signal into the soil. For the propagation through air to soil as shown in Figure 2.31, $\eta_1 = \eta_{\text{air}} \cong 1$ [98, 99] and

$\eta_2 = \eta_{\text{soil}}$. For the sake of simplicity, the relative intrinsic impedance of soil will be denoted as "η_s", conductivity, relative permittivity and permeability values of soil will be denoted as "σ_s", "ϵ_s" and "μ_s" respectively. Moreover, conductivity, relative permittivity and permeability values of air will be accepted as "0", "1" and "1" respectively for the rest of this study. Thus, reflection coefficient (Γ_{as}) in Figure 2.10 is;

$$\Gamma_{as} = \frac{\eta_s - 1}{\eta_s + 1} = |\Gamma_{as}|e^{j\sphericalangle\Gamma_{as}}, \tag{42}$$

where $Re\{\Gamma_{as}\} = |\Gamma_{as}|\cos(\sphericalangle\Gamma_{as})$ and $Im\{\Gamma_{as}\} = |\Gamma_{as}|\sin(\sphericalangle\Gamma_{as})$

So, η_s in terms of Γ_{as} can be written as [98];

$$Re\{\eta_s\} = \frac{1 - Re\{\Gamma_{as}\}^2 - Im\{\Gamma_{as}\}^2}{(1 - Re\{\Gamma_{as}\})^2 + Im\{\Gamma_{as}\}^2} \quad \text{and} \quad Im\{\eta_s\} = \frac{2Im\{\Gamma_{as}\}}{(1 - Re\{\Gamma_{as}\})^2 + Im\{\Gamma_{as}\}^2}, \tag{43}$$

Eventually, by measuring the amplitude ($|\Gamma_{as}|$) and phase ($\sphericalangle\Gamma_{as}$) of the reflection coefficient (Γ_{as}) for a specific frequency ω, the relative permittivity (ϵ_s) and conductivity (σ_s) values of the soil can be computed by using Eq. 39-43. Note that, the relative permeability of soil is assumed to be equal to that of air [95].

2.4.2. Attenuation of Electromagnetic Signal Propagating Through a Medium

In this section, the propagation loss is introduced in a lossy medium. When an electromagnetic signal propagates through a medium, the amplitude and phase of the signal change with respect to the propagation constant (γ) of the medium. Given E_0 is the complex amplitude at the source of an electromagnetic signal, value of the complex amplitude E_z at a distance z is given in Eq. 44 [92].

$$E(z) = E_z = E_0 e^{-\gamma z}, \tag{44}$$

Since the propagation constant is a complex quantity, it can be written as $\gamma = \alpha + j\beta$ where α is called the attenuation constant and β is called the phase constant. Under low-loss condition, α and β can be computed by Eq. 45 [92].

$$\alpha = Re(\gamma) \cong \frac{\sigma}{2}\sqrt{\frac{\mu}{\epsilon}} \quad (Np/m) \quad \text{and} \quad \beta = Im(\gamma) \cong \omega\sqrt{\mu\epsilon} \quad (rad/m), \quad (45)$$

Amplitude of the propagating signal changes depending on the attenuation constant (α) of the medium. If we take the absolute value of both sides in Eq. 44, the phase term can be cancelled out as shown in Eq. 46.

$$|E_z| = |E_0|e^{-\alpha z}, \quad (46)$$

This equation is valid for very narrow beams only. If the radiating electromagnetic beams become wider as z increases, amplitude of E_z is:

$$|E_z| = G(z)|E_0|e^{-\alpha z}, \quad (47)$$

Here, $G(z)$ is the geometrical spreading factor and depends on the antenna type of GPR [101]. For example, $G(z) = \frac{1}{z}$ for dipole antenna which is used for simulations given in the results section.

2.4.3. Velocity of Electromagnetic Signal Propagating Through a Medium

Propagation velocity of an electromagnetic signal into a medium with permittivity (ϵ) and permeability (μ) can be computed by Eq. 48 [92].

$$v = \frac{1}{\sqrt{\mu\epsilon}} = \frac{c}{\sqrt{\mu_r \epsilon_r}} \quad (m/s), \quad (48)$$

where c is the speed of light in free space.

CHAPTER 3

PROPOSED ALGORITHM

The proposed algorithm is composed of two stages which are "Calibration Measurement" and "Detection & Classification" steps. For the first stage, a calibration measurement is taken to estimate intrinsic characteristics of the soil in the experimental area. In "Detection & Classification" step, anomaly locations are detected in the same area and they are classified as targets or non-targets by utilizing the calibration parameters as shown in Figure 3.1.
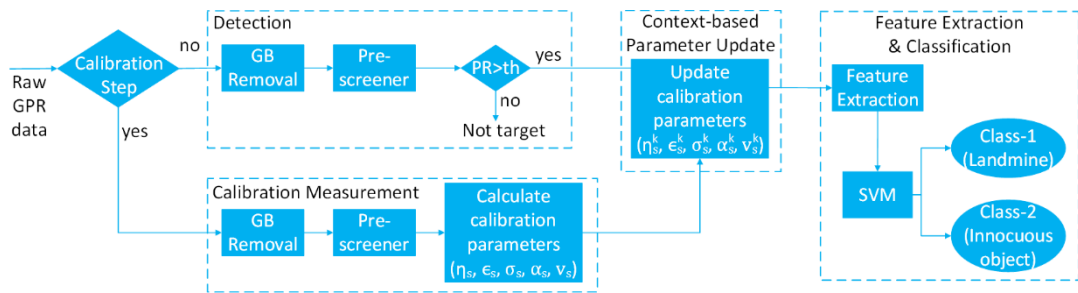
Figure 3.1. Flow Chart of the Proposed Method

A typical scenario for landmine sweeping is shown in Figure 3.2. Before starting landmine sweeping in an experimental area, a calibration object is buried in the same area to take the calibration measurement.
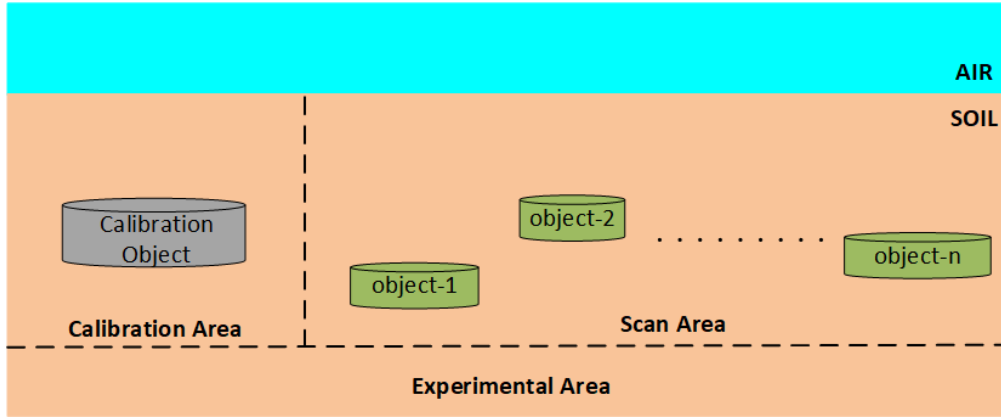
Figure 3.2. Scenario for Landmine Sweeping

A typical GPR measurement and relevant parameters are shown in Figure 3.3, when GPR antenna is above the target or calibration object. In real experiments, there is a distance between TX and RX of GPR, therefore transmitted ray from TX should propagate obliquely and be reflected from the ground (or underground object) to reach RX of GPR. However, during this study, calculations are performed under normal incidence case as shown in Figure 3.3. Since the distance between TX and RX is very small according to GPR antenna height (h_a) and target depth (h_c), oblique angles are very small. Therefore, normal incidence assumption is acceptable for this study. The difference between the calculations under normal incidence case and under oblique incidence case is shown in Appendix A.

E_0	: elect. field intensity of incident wave
E_{GB}	: elect. field intensity of ground bounce
$E_{return}(h_{c/t})$	: elect. field intensity of primary reflection from target at depth $h_{c/t}$
ϵ_0	: electrical permittivity of vacuum
μ_0	: magnetic permeability of vacuum
σ_0	: electrical conductivity of vacuum
ϵ_s	: electrical permittivity of soil
μ_s	: magnetic permeability of soil
σ_s	: electrical conductivity of soil
Γ_{as}	: reflection coeff. from air to soil
τ_{as}	: transmission coeff. from air to soil
Γ_{st}	: reflection coeff. from soil to target
τ_{st}	: transmission coeff. from soil to target
τ_{sa}	: transmission coeff. from soil to air
h_a	: height of the GPR antenna
$h_{c/t}$	: h_c - depth of the calibration object h_t - depth of the target
$\ell_{c/t}$	: ℓ_c - length of the calibration object ℓ_t - length of the target
$D_{c/t}$	: D_c - diameter of the calibration object D_t - diameter of the target

Figure 3.3. GPR Measurement of Calibration Object or Targets

46

By means of calibration measurement, intrinsic properties of soil are estimated and they are used in target classification step. The calibration object is a cylindrical shape PEC (Perfect Electrical Conductor) with diameter D_c and height l_c as shown in Figure 3.3. During calibration measurement and landmine sweeping, height of the GPR antenna above the surface of the ground is h_a. Before starting landmine sweeping in an area, this cylindrical PEC is buried at depth h_c and GPR is passed over the buried calibration object.

For the Target Detection & Classification Phase, initially the ground bounce is removed from the original GPR data. Then, a pre-screener algorithm is used to detect the possible anomaly locations. Hence, the amount of data that will be used in the feature extraction step is minimized. For each anomaly region, the gradient-based algorithm is used to select A-scan data which has the highest amplitude in the corresponding B-Scan image. In Context-based Parameter Update step, the calibration parameters are updated by considering the variation of the soil dielectric properties for each anomaly region. To achieve this, the ground bounce values in the calibration area and in the anomaly region are compared. Afterwards, for each anomaly region, three different features are extracted by utilizing the intrinsic characteristics of the soil which are calculated in the calibration measurement and updated in the context-based parameter update step. Finally, targets are classified by SVM based on these extracted features.

3.1. Calibration Measurement

In Section 2.4, the relation between the reflection coefficient and intrinsic parameters of a medium is given. This step shows how to extract these parameters from GPR data. As stated before, the calibration object is a cylindrical shape PEC (Perfect Electrical Conductor) with diameter D_c and height l_c which is used to compute the dielectric properties (relative permittivity and conductivity) of soil, attenuation constant of soil and GPR signal velocity in the soil. In all computations, A-Scan data measured at the cross-track position x = x_0 (A(x_0, t)) is used given in Figure 3.4. Here, x_0 corresponds

to apex of target response hyperbola and it is computed using the gradient-based algorithm given in [17]. Details of this computation process are given in Section 3.3. An example calibration measurement and the corresponding A-Scan data (mid A-Scan) are shown in Figure 3.4.

(a)　　　　　　　　　　　　　　　　(b)
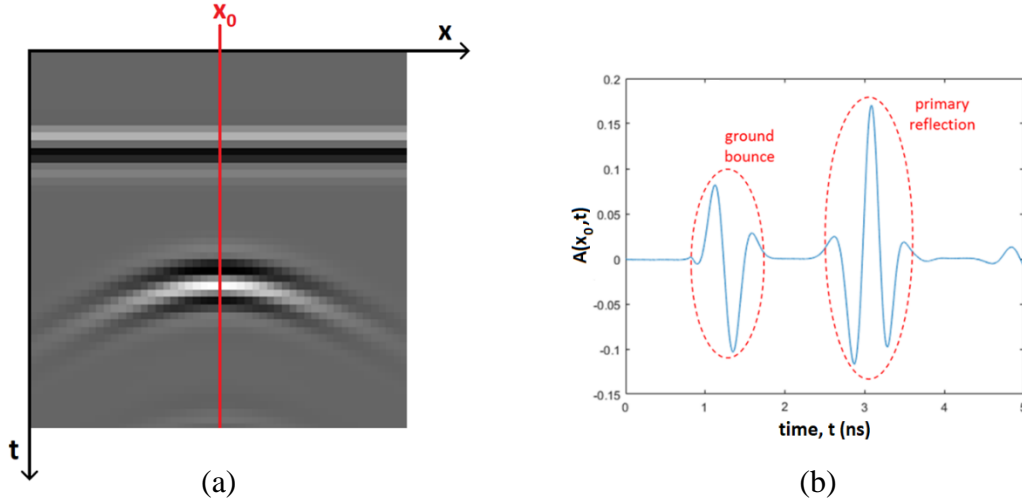
Figure 3.4. An Example Calibration Measurement (a) B-Scan Image, (b) A-Scan Data at $x=x_0$

3.1.1. Dielectric Properties of Soil

In this step, the complex intrinsic impedance, conductivity and relative permittivity of the soil in the calibration area are computed. E_0 is the electric field at the TX according to Figure 3.3. Using Eq. 44, value of the incident wave (E_0) at the air – soil boundary becomes:

$$E(h_a) = E_0 e^{-\alpha_{air} h_a} e^{-j\beta_{air} h_a}, \tag{49}$$

Here, $\alpha_{air} \cong 0$ and $\beta_{air} \cong \omega\sqrt{\mu_0 \epsilon_0}$ according to Eq. 45, because $\mu_{air} \cong \mu_0, \epsilon_{air} \cong \epsilon_0$ and $\sigma_{air} \cong 0$. So, the value of the signal at the air – soil boundary is:

$$E(h_a) = E_0 e^{-j\omega\sqrt{\mu_0 \epsilon_0} h_a}, \tag{50}$$

The value of the ground bounce (E_{GB}), which is the reflected signal from the surface of the ground, is:

48

$$E_{GB} = E_0|\Gamma_{as}|e^{-j\omega\sqrt{\mu_0\epsilon_0}2h_a}e^{j\angle\Gamma_{as}}, \tag{51}$$

Here, $\Gamma_{as} = |\Gamma_{as}|e^{j\angle\Gamma_{as}}$ is complex reflection coefficient of soil. Therefore, it can be calculated by using Eq. 52.

$$|\Gamma_{as}|e^{j\angle\Gamma_{as}}e^{-j\omega\sqrt{\mu_0\epsilon_0}2h_a} = \frac{E_{GB}}{E_0}, \tag{52}$$

Note that, the term $e^{-j\omega\sqrt{\mu_0\epsilon_0}2h_a}$ is due to the antenna height (h_a) and causes a time delay. If Eq. 52 is given in terms of amplitude and phase separately, the following equations are obtained:

$$|\Gamma_{as}| = \frac{|E_{GB}|}{|E_0|}, \tag{53}$$

$$\angle(E_{GB}, E_0)|_w = \angle\Gamma_{as} - 2\omega\sqrt{\mu_0\epsilon_0}h_a, \tag{54}$$

Calculating the amplitude of the reflection coefficient is straightforward, it is simply amplitude of the ratio of ground bounce to incident wave. However, calculating the phase difference is more challenging, because phase difference depends on the frequency and it has a different value for each different operating frequency. Therefore, phase difference should be calculated for a specific frequency value. To achieve this, ground bounce and incident wave are transformed into frequency domain by applying Fast Fourier Transform (FFT). Afterwards, phase of the ground bounce and phase of the incident wave can be computed for a specific frequency value and phase difference can be obtained. In this study, the frequency value for which phase difference is calculated is chosen as the center frequency of GPR.

Afterwards, the complex intrinsic impedance of soil ($Re\{\eta_s\}$ and $Im\{\eta_s\}$) is calculated according to Eq. 43. Finally, the relative permittivity (ϵ_s) and conductivity (σ_s) of the soil in the calibration region are calculated by Eq. 40 under the assumption that the permeability of soil is assumed to be equal to that of air [95].

Twelve different soil types are created which have relative permeability of 1, conductivity of 10 mS/m and relative permittivity between 4.5 and 10 with the

increment of 0.5 to verify the computation process of the complex intrinsic impedance of soil. For each soil type, a reference GPR measurement is taken by gprMax modelling software [102] and the ground bounce values are saved for each case. By using these ground bounce values, complex reflection coefficients are computed by Eq. 52-54 and complex intrinsic impedances are calculated by Eq. 42 and Eq. 43. In Figure 3.5, theoretical and simulated results of complex intrinsic impedance values of given twelve different soil types are shown. Theoretical results are computed according to Eq. 40. Simulated results are calculated by using the simulated ground bounce values and Eq. 42, 43, 52, 53 and 54. Please observe that, simulated complex intrinsic impedance values are very close to the theoretical results which verifies the proposed method.
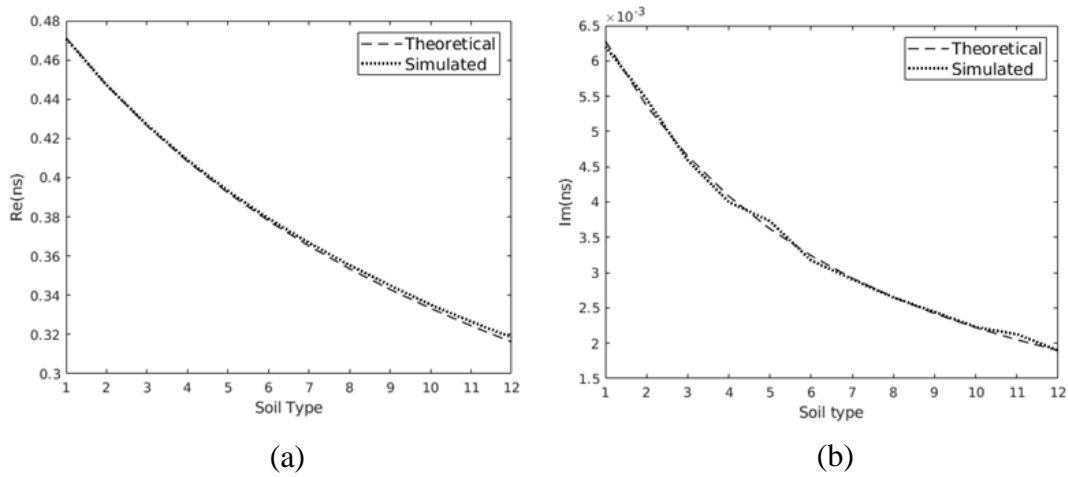
Figure 3.5. Theoretical and Simulated Result of Complex Intrinsic Impedance Values of 12 Different Soil Types, (a) Real Part, (b) Imaginary Part

3.1.2. Attenuation Constant of Soil

In this step, the attenuation constant of the soil in the calibration area is calculated. The material of calibration object is PEC and intrinsic impedance of PEC is very small. Hence, reflection coefficient of PEC material is -1 ($\Gamma_{st} = -1$ in Figure 3.3 for calibration measurement). Therefore, PEC object reflects all energy back. Using Figure 3.3, Eq. 41 and Eq. 47, amplitude of E_{return_PEC} can be given as:

$$A(h_c) \triangleq \left|E_{return\_PEC}(h_c)\right| \cong |E_0||\tau_{as}\tau_{sa}|G(h_a + h_c)e^{-2\alpha_s h_c}, \qquad (55)$$

where $\quad |\tau_{as}\tau_{sa}| = \left|\dfrac{4\eta_s}{(\eta_s+1)^2}\right| \quad$ and $\quad G(h_a + h_c) = \dfrac{1}{8\pi^2(h_a+h_c)^2}$

$A(h_c)$ is defined as amplitude of the return signal from a PEC surface at depth h_c as shown in Figure 3.3. In the simulations, dipole antenna is used; therefore geometrical spreading factor $(G(h_a + h_c))$ varies inversely as the square of the distance [103]. Attenuation constant of soil α_s can be computed by inversely solving Eq. 55.

A PEC material is buried at 15 cm depth in a soil with $\mu_s = 1$, $\epsilon_s = 4.5$, $\sigma_s = 10\ mS/m$ and the amplitude of the primary reflection is measured by using gprMax modeling software to verify Eq. 55 experimentally. Then, α_s is calculated by using this measurement as explained above. Afterwards, in gprMax modeling software the same PEC material is buried at depths between 10 cm and 14.5 cm with the increment of 0.5 cm in the same soil. Amplitude of the primary reflection is measured for each case. Moreover, for each case the amplitude of the primary reflection is calculated theoretically by utilizing Eq. 55. Finally, the simulated results are compared with the calculated values as shown in Figure 3.6. The results are very similar for each case which verifies the proposed method.

Figure 3.6. Simulated and Theoretical Results for Attenuation

3.1.3. GPR Signal Velocity in the Soil

In this step, GPR signal velocity in the soil of the calibration area is calculated. GPR signal velocity in a medium can be calculated by utilizing Eq. 48. Since, the relative permittivity value of the soil is already calculated in Section 3.1.1, Eq. 48 can be applied to compute GPR signal velocity theoretically. On the other hand, GPR signal velocity into the corresponding soil can be calculated experimentally by using the calibration measurement. By referring Figure 3.3, the incident wave reflected from the ground (ground bounce) travels $2h_a$ while the reflected signal from the buried object (primary reflection) travels $2h_a + 2h_c$ until they reach the RX of GPR antenna. GPR signal velocity into the soil can be calculated by using the time difference between these two received signals as given in Eq. 56. During landmine sweeping, this information is used to estimate the buried depth of the target. For the sake of consistency, in this section GPR signal velocity is calculated experimentally.

The time difference between the ground bounce and the primary reflection gives the time of GPR signal travels $2h_c$ way of soil (h_c forth and h_c back). Therefore, GPR signal velocity into the soil (v_s) can be calculated by Eq. 56.

$$v_s = \frac{2h_c}{|time_{ground\ bounce} - time_{primary\ reflection}|}, \tag{56}$$

To verify Eq. 56 experimentally, a PEC material is buried at 15 cm depth in 12 different soil types which have relative permeability of 1, conductivity of 10 mS/m and relative permittivity between 4.5 and 10 with the increment of 0.5. GPR signal velocity values are calculated by Eq. 56. Afterwards, the same values are calculated by Eq. 48 theoretically. Finally, the simulated results are compared with the calculated values as shown in Figure 3.7. The results are very similar for each case which verifies the proposed method.
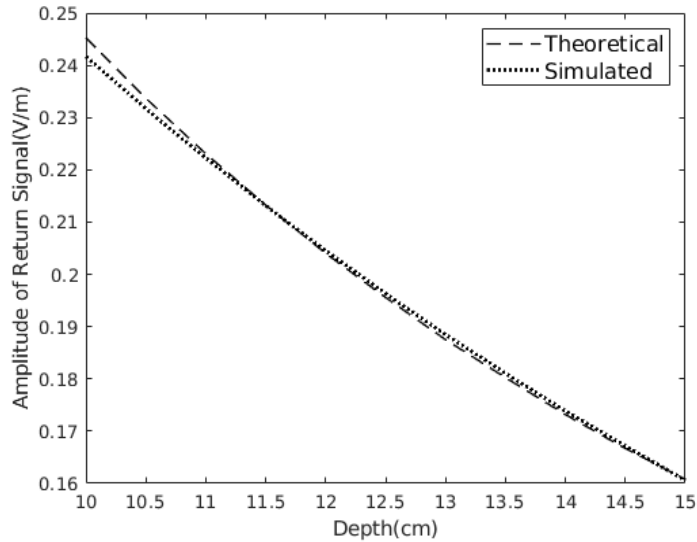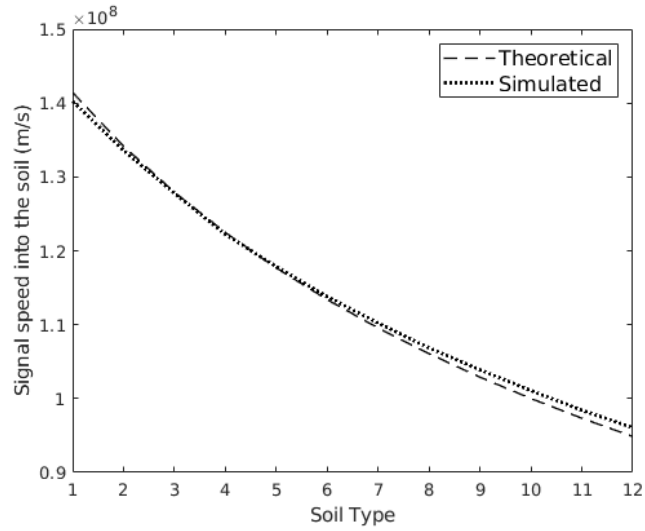
Figure 3.7. Simulated and Theoretical Results for GPR Signal Velocity

All in all, from the calibration measurement, three important parameters: dielectric properties of soil (ϵ_s, σ_s and η_s), attenuation constant of soil (α_s) and GPR signal velocity in the soil (v_s) are calculated by Eq. 49-56. These parameters are used to extract intrinsic features of the alarm locations for further experiments.

3.2. Ground Bounce Removal and Pre-screener

After the calibration measurement, next step is to detect and classify buried objects in the same experimental area. Initially, ground bounce is removed from the original GPR data as proposed in [91]. Maximum detection technique is used to find the location of the ground bounce. Details of this technique is given in Section 2.3.1. After maximum detection, alignment is necessary due to up-down movement of vehicle mounted GPR antenna. Then, L time samples after the ground bounce peak are removed from each A-Scan data. L is determined based on the ground bounce in time [91]. An example scenario is shown in Figure 3.8. PMA, PMD and PMN, which are explained in detail in the results section, are three landmines. Tin box has 8 cm diameter and 8 cm height. Rock has 7 cm width, 14 cm length and 3 cm height. B-Scan GPR data belongs to this example scenario is given in Figure 3.9-a. After the ground bounce removal step, this B-Scan data is shown as in Figure 3.9-b.
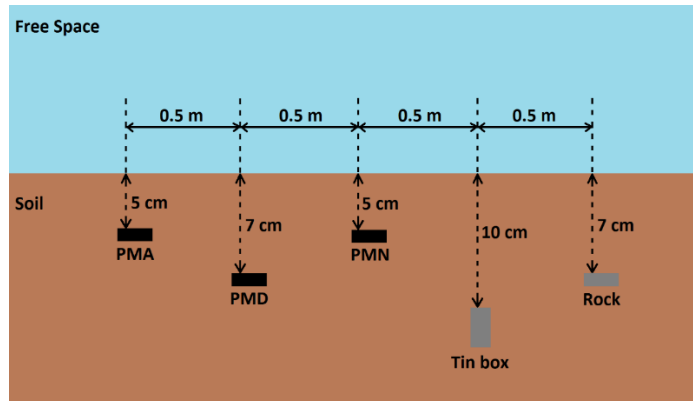
Figure 3.8. An Example Simulation Scenario

Figure 3.9. (a) Raw GPR Data, (b) Ground Bounce Removed GPR Data

Complex discrimination algorithms can be run in real-time by only applying these algorithms to a small subset of available data. To minimize the amount of data which will be used in the feature extraction step, an LMS-based pre-screener algorithm is utilized. Other pre-screener algorithms than LMS can also be used in this step. We have adopted LMS algorithm since, it is one of the most widely used adaptive pre-screener techniques in the literature [50-52].

In this study, 1-D LMS algorithm is applied through each column of B-Scan image as described in Section 2.3.2. Since the targets which are buried deeper have weak GPR response with respect to shallowly buried targets, LMS algorithm tends to remove the response of deeply buried targets. To avoid this issue, B-Scan image is normalized to enhance the deeper region of data. To achieve this, each row of ground bounce removed B-Scan image is normalized before LMS algorithm.

For implementation of 1D LMS algorithm, filter length is chosen as 12 and guard-band length is chosen as 5. For each selected window, LMS finds the differences from the background by adaptively updating the filter coefficients. Then, a threshold is applied to the Pre-screener Result (PR) and a decision is made according to that threshold as explained in [52]. Then, projections of thresholded image is obtained and binary mapping is applied to the value of each projection. Finally, the centroids of connected areas are chosen as the mid-points of anomaly regions. As an example, LMS result of B-scan image given in Figure 3.9-b and the possible anomaly regions are shown in Figure 3.10.
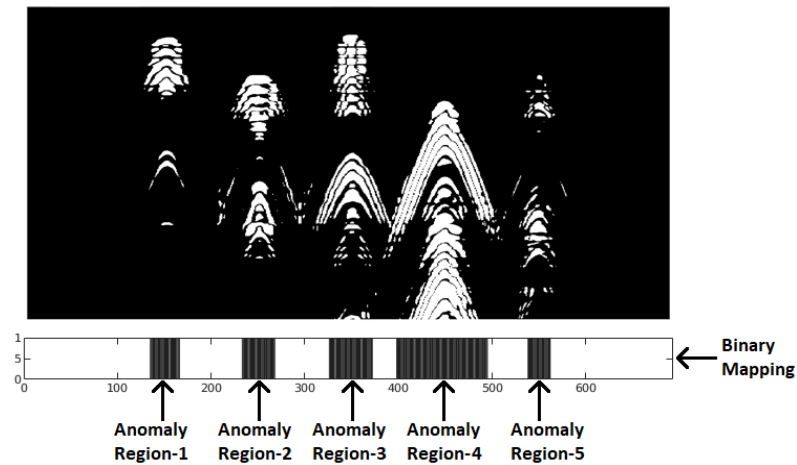
Figure 3.10. LMS Result of B-Scan Image Given in Figure 3.9-b, Binary Mapping Result and Possible Anomaly Regions

For each anomaly region, the gradient-based algorithm described in [17] is utilized to select the A-Scan data that is measured when GPR antenna was above the center of the target (when GPR antenna is at the position shown in Figure 3.3). Details of the gradient-based algorithm is given in Section 2.3.3. For a given B-Scan image, gradient-based algorithm finds the degree to which edges occur in the diagonal and anti-diagonal directions. The algorithm formulates the states of the discrete model of the target as the leading edge, center and trailing edge. The region where diagonal edges occur corresponds to leading edge state and where anti-diagonal edges occur corresponds to trailing edge state. Center state of the algorithm shows the transition

region from diagonal to anti-diagonal edges [17]. The A-Scan data, which will be further processed for the feature extraction step, belongs to this transition region. If there are multiple A-Scan data into this region, the one which has the highest amplitude is chosen as shown in Figure 3.11. This A-Scan data will be called as "mid A-Scan" of a given B-Scan image for the rest of this study. Here, it is not always possible to find the correct mid A-Scan data due to noise of the system. The impact of this issue is discussed in the results section.
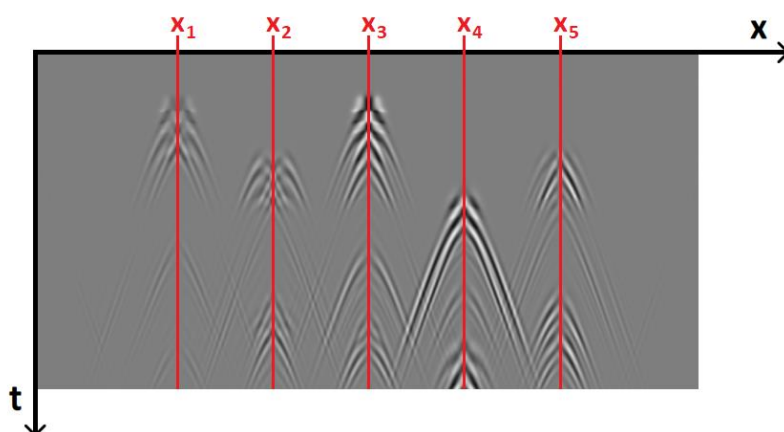
Figure 3.11. Result of the Gradient-based Method – x_1, x_2, x_3, x_4 and x_5 Denote the Positions of A-Scan Data to Be Used for Feature Extraction Step

Before starting the feature extraction step, the calibration parameters are updated for the corresponding anomaly region by Context-based Parameter Update step.

3.3. Context-based Parameter Update

In the calibration measurement, three important parameters: dielectric properties of soil (ϵ_s, σ_s and η_s), attenuation constant of soil (α_s) and GPR signal velocity in the soil (v_s) are calculated by Eq. 49-56 for the calibration region. The relative permeability of soil is almost always assumed to be equal to 1 and does not vary from area to area [95]. However, conductivity and relative permittivity of soil may change even in small areas especially depending on the soil moisture content [105, 106]. Since the calibration parameters vary during landmine sweeping, large scale estimates are not reliable and these parameters should be updated for each anomaly region.

Initially, the dielectric properties of the "k^{th}" anomaly region (ϵ_s^k, σ_s^k and η_s^k) are calculated by applying the same procedure described in Section 3.1.1. Initially, amplitude ($|\Gamma_{as}^k|$) and phase ($\sphericalangle\Gamma_{as}^k$) of the reflection coefficient are computed by Eq. 53 and Eq. 54. Then, the complex intrinsic impedance of soil (η_s^k) is calculated according to Eq. 43. Finally, the relative permittivity (ϵ_s^k) and conductivity (σ_s^k) of the soil in the "k^{th}" anomaly region are calculated by Eq. 40.

Afterwards, attenuation constant and GPR signal velocity of the "k^{th}" anomaly region (α_s^k and v_s^k) are found by updating the attenuation constant and GPR signal velocity of the calibration area (α_s and v_s) as shown in Figure 3.12. To achieve this, the difference between the dielectric properties of the "k^{th}" anomaly region (ϵ_s^k, σ_s^k and η_s^k) and the dielectric properties of the calibration region (ϵ_s, σ_s and η_s) is utilized.
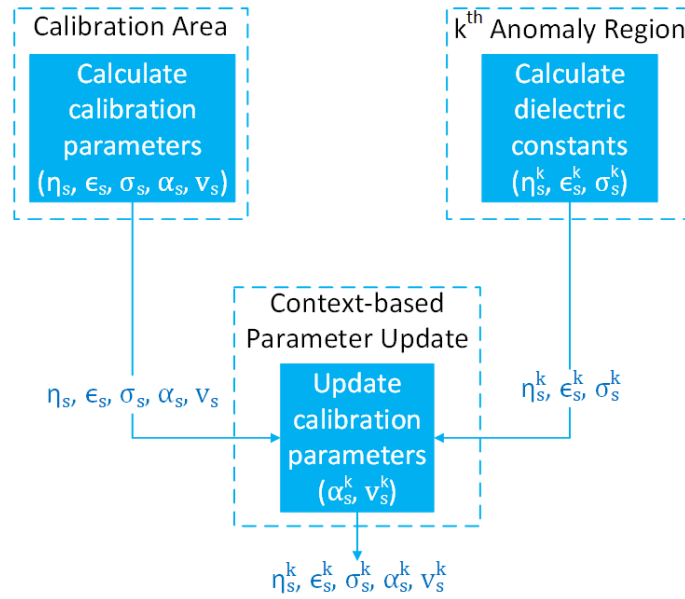

Figure 3.12. Context-based Parameter Update Step

Attenuation constant of the "k^{th}" anomaly region (α_s^k) is computed. For low-loss dielectrics, attenuation constant is calculated by Eq. 45. Hence, the attenuation constant of the calibration region (α_s) can be updated by applying Eq. 57 to obtain the attenuation constant of the anomaly region (α_s^k).

$$\alpha_s^k = \alpha_s \frac{\sigma_s^k}{\sigma_s} \sqrt{\frac{\epsilon_s}{\epsilon_s^k}}, \tag{57}$$

Finally, GPR signal velocity in the soil of the "k^{th}" anomaly region (v_s^k) is calculated. GPR signal propagates with the speed of light (c) in free space. GPR signal velocity in an environment can be calculated by Eq. 48. Hence, GPR signal velocity in the calibration region (v_s) can be updated by applying Eq. 58 to obtain GPR signal velocity in the anomaly region (v_s^k).

$$v_s^k = v_s \sqrt{\frac{\epsilon_s}{\epsilon_s^k}}, \tag{58}$$

All in all, in the calibration measurement, three important parameters: dielectric properties of soil (ϵ_s, σ_s and η_s), attenuation constant of soil (α_s) and GPR signal velocity in the soil (v_s) are calculated by Eq. 49-56 and in this section these parameters are updated for the corresponding anomaly region. Updated parameters are used to extract intrinsic features of the corresponding target.

3.4. Feature Extraction

In this work, three different features are extracted for each anomaly region: Dielectric feature, energy feature and geometry feature. Geometry feature is extracted from the ground bounce removed B-Scan image of the corresponding anomaly region. Dielectric feature and energy feature are extracted from the ground bounce removed A-Scan data (mid A-Scan) which has the highest amplitude in the corresponding B-Scan image.

Dielectric feature estimates the intrinsic impedance of the buried object by utilizing physics-based approach and depends on the material type of the underground target. Energy feature identifies significant GPR signal length. It depends on both material type and size, especially length of the buried object. Geometry feature computes gradient of the corresponding B-Scan data by utilizing image-based feature extraction methods. This feature depends on size, especially surface area of the buried object.

58

Therefore, these features are complementary to each other and the combination of them is very promising.

3.4.1. Dielectric Feature

The environment for the corresponding anomaly region is modelled during calibration and context-based parameter update steps, so the return signal for PEC object buried in any depth can be modelled as well. In this section, intrinsic properties of the unknown object are computed from its return signal (E_{return_target} in Figure 3.3) by utilizing theoretically computed PEC return signal.

The first step is to compute target depth (h_t) by using Eq. 59. Note that, in the context-based parameter update step, intrinsic impedance (η_s^k), attenuation constant (α_s^k) and GPR signal velocity (v_s^k) are calculated in the soil of the kth anomaly region.

$$h_t = \frac{v_s^k |time_{ground\ bounce} - time_{primary\ reflection}|}{2}, \tag{59}$$

After target depth is calculated, amplitude of the return signal from a PEC surface at the same depth of the target ($|E_{return\_PEC}(h_t)|$) is computed by using Eq. 60.

$$A(h_t) \triangleq |E_{return_{PEC}}(h_t)| = |E_0||\tau_{as}^k \tau_{sa}^k| G(h_a + h_t) e^{-2\alpha_s^k h_t}, \tag{60}$$

where $\quad |\tau_{as}^k \tau_{sa}^k| = \left|\frac{4\eta_s^k}{(\eta_s^k+1)^2}\right| \quad$ and $\quad G(h_a + h_t) = \frac{1}{8\pi^2(h_a+h_t)^2}$

Amplitude of the return signal from the target ($|E_{return\_target}(h_t)|$) is measured by GPR experimentally. This value ($|E_{return\_target}(h_t)|$) can be written theoretically as shown in Eq. 61.

$$A_{target}(h_t) \triangleq |E_{return_{target}}(h_t)| = |E_0||\tau_{as}^k \tau_{sa}^k||\Gamma_{st}^k| G(h_a + h_t) e^{-2\alpha_s^k h_t}, \tag{61}$$

where $\quad |\tau_{as}^k \tau_{sa}^k| = \left|\frac{4\eta_s^k}{(\eta_s^k+1)^2}\right| \quad$ and $\quad G(h_a + h_t) = \frac{1}{8\pi^2(h_a+h_t)^2}$

By comparing Eq. 60 and Eq. 61, amplitude of the reflection coefficient of target ($|\Gamma_{st}^k|$) in the "k^{th}" anomaly region can be computed by Eq. 62.

$$\left|\Gamma_{st}^{k}\right| = \frac{A_{target}(h_t)}{A(h_t)}, \tag{62}$$

In Section 2.4.1, it is written that the working medium can be assumed as low-loss according to the frequency band of GPR. Therefore, the intrinsic impedance of soil is almost real (complex part is very small with respect to the real part as shown in Figure 3.5). Moreover, in this study, our main interest is to identify the landmines with little or no metal content. These landmines are made of plastic, rubber, bakelite, glass or wood. All these materials satisfy low-loss condition. Therefore, the following equations are correct.

$$\eta_s^k \cong Re\{\eta_s^k\}, \tag{63}$$

$$\eta_t^k \cong Re\{\eta_t^k\}, \tag{64}$$

Theoretical formula of Γ_{st}^{k} is given in Eq. 41. So, the following equation can be written:

$$\left|\Gamma_{st}^{k}\right| = \begin{cases} \Gamma_{st}^{k} & if\ Re\{\eta_t^k\} > Re\{\eta_s^k\} \\ -\Gamma_{st}^{k} & else \end{cases}, \tag{65}$$

So, intrinsic impedance of the target is estimated by using Eq. 66;

$$\eta_t^k \cong Re\{\eta_t^k\} \cong \begin{cases} Re\{\eta_s^k\}\frac{1+\left|\Gamma_{st}^{k}\right|}{1-\left|\Gamma_{st}^{k}\right|} & if\ Re\{\eta_t^k\} > Re\{\eta_s^k\} \\ Re\{\eta_s^k\}\frac{1-\left|\Gamma_{st}^{k}\right|}{1+\left|\Gamma_{st}^{k}\right|} & else \end{cases}, \tag{66}$$

Dielectric feature of an anomaly region is equal to intrinsic impedance of the target (η_t^k) that is calculated from mid A-scan data by means of Eq. 59-66. Before applying Eq. 66, we should know whether $Re\{\eta_t^k\}$ is greater than $Re\{\eta_s^k\}$. This inequality can be checked by observing the sign of the primary reflection. If $Re\{\eta_t^k\}$ is greater than $Re\{\eta_s^k\}$, Γ_{st}^{k} is greater than zero and sign of the primary reflection becomes positive. If $Re\{\eta_t^k\}$ is less than $Re\{\eta_s^k\}$, Γ_{st}^{k} is less than zero and sign of the primary reflection becomes negative. It means that, primary reflection becomes flipped. This phenomenon can be understood by examining the following figure.

(a)   (b)

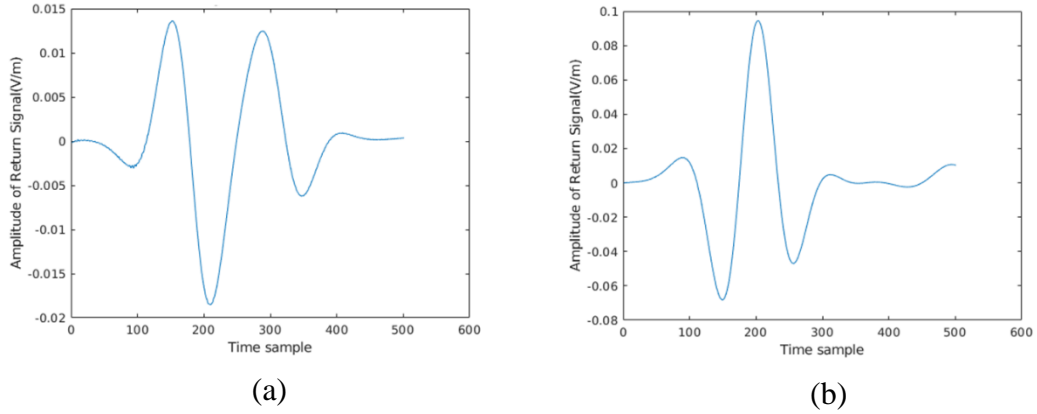*Figure 3.13.* (a) Primary Reflection for $Re\{\eta_t^k\} > Re\{\eta_s^k\}$, (b) Primary Reflection for $Re\{\eta_t^k\} < Re\{\eta_s^k\}$

If the buried object does not satisfy low-loss condition, Eq. 66 still estimates the real part of the intrinsic impedance as described in Appendix B. The flowchart of dielectric feature extraction method is given in Figure 3.14.
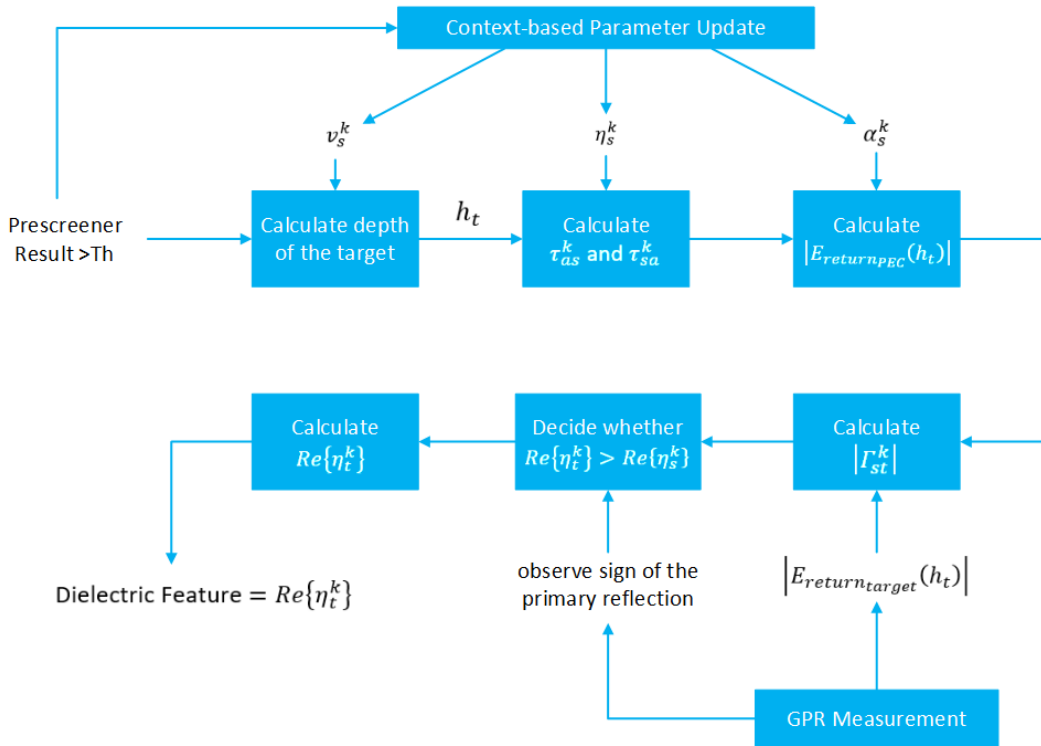

Figure 3.14. Dielectric Feature Extraction Method

3.4.2. Energy Feature

This feature is described as the minimum signal length that carries more than 90% of the signal's total energy. The rationale behind this feature is to figure out the size of the region where the energy of the signal (ground bounce removed A-Scan data) is concentrated. To measure this, initially ground bounce is removed from mid A-Scan data of the corresponding B-Scan image. Then, cumulative energy curve of this data is calculated as described in [107]. An example A-Scan data and its corresponding cumulative energy curve is shown in Figure 3.15.

(a)   (b)
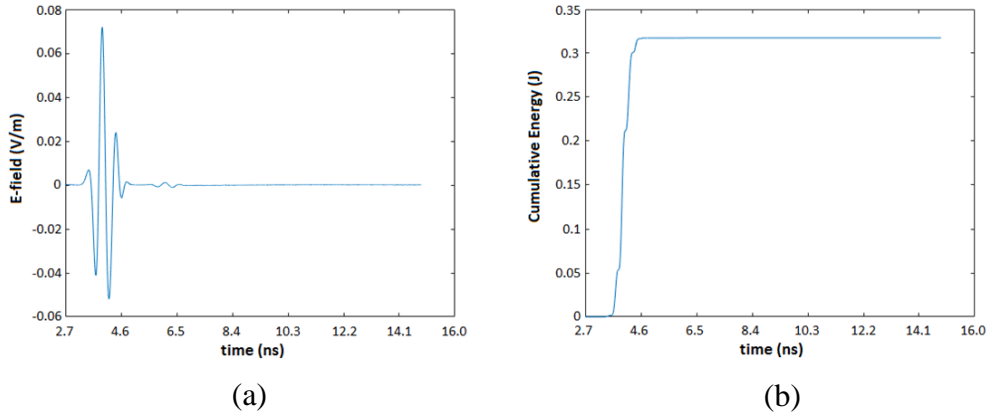
Figure 3.15. (a) Ground Bounce Removed mid A-Scan Data, (b) Its Cumulative Energy Curve

The formulation to extract the Energy Feature is given below:

- Define $n \coloneqq number\ of\ scan\ steps\ in\ GB\ removed\ mid\ A - Scan\ data$

- Define $e(t) \coloneqq ground\ bounce\ removed\ A\ Scan\ data\ for\ t = 1, \dots, n$

- Define $c(t) \coloneqq cumulative\ energy\ curve\ of\ e(t)\ s.t.\ c(t) \triangleq \sum_{k=1}^{t} |e(k)|^2$

- Find (a, b) pairs which satisfy

  o $a < b \leq n$

  o $c(b) - c(a) \geq 0.9c(n)$

- Choose the pair (a, b) such that $"b - a"\ is\ minimum$

- Energy feature = minimum signal length = $b - a$

62

3.4.3. Geometry Feature

First two features (Energy feature and Dielectric feature) consider the A-scan data which has the highest amplitude in the corresponding B-Scan image and try to extract discriminative information about the material type of the target. On the other hand, geometry (shape) of the target is another important information to discriminate different objects. Geometry feature estimates the shape, especially the surface area of the buried object.

To extract the geometry feature, right half of the corresponding B-Scan image is evaluated. Consider, I is the image of the right part from the apex point of the corresponding B-scan data as shown in Figure 3.16.
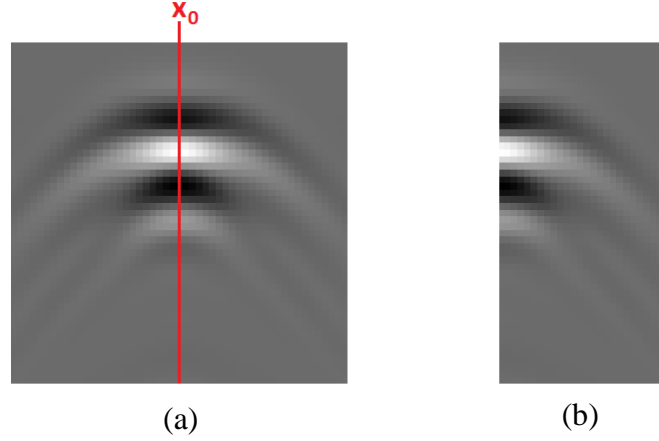

<div align="center">(a)   (b)</div>

Figure 3.16. (a) B-Scan Data of PMA Landmine (x_0 denotes the position of mid A-Scan data), (b) Right Half of It that is Denoted by I

Like Scale Invariant Feature Transform (SIFT) [64] or Histogram of Oriented Gradients (HoG) [21-23] feature extraction methods, the gradient vector at each point is calculated containing the horizontal and vertical derivatives as given in Eq. 67.

$$I_x = I * g_x \quad \text{and} \quad I_y = I * g_y, \tag{67}$$

where g_x and g_y represent gradient filters $[-1, 0, 1]$ and $[-1, 0, 1]^T$ respectively. The magnitude and the orientation of the resulting gradient vector are given in Eq. 68 and Eq. 69.

$$G(i,j) = \sqrt{(I_x(i,j)^2 + I_y(i,j)^2)}, \qquad (68)$$

$$A(i,j) = arctan\frac{I_y(i,j)}{I_x(i,j)}, \qquad (69)$$

Differently from the SIFT or HoG features, we do not assume a pre-specified block size. Instead, the gradient of the entire image I is calculated at one time by Eq. 70 and Eq. 71.

$$\text{normalized orientation } \overline{A}(i,j) = A(i,j) * G(i,j), \qquad (70)$$

$$\text{gradient} = \frac{\sum_i \sum_j \overline{A}(i,j)}{\sum_i \sum_j G(i,j)}, \qquad (71)$$

The gradient value, which is calculated by Eq. 71, is the geometry feature of the corresponding alarm location.

If the surface area of a buried object is large, the corresponding target response hyperbola of GPR measurement will be fairly flat and straight. Otherwise, it will be sharp. Geometry feature estimates how much the target response hyperbola is flat or sharp. If the surface area of a buried object is large (corresponding hyperbola is flat), its geometry feature will be small. Otherwise, the geometry feature will be large.

3.5. Classification

In Section 3.4, Dielectric Feature, Energy Feature and Geometry Feature of each anomaly region are calculated. For the classification, two class (Class 1: Landmine, Class 2: Innocuous Object) support vector machine (SVM) algorithm [73, 74, 108] is implemented as described in Section 2.3.6. By focusing on the training samples, SVM finds an optimal separating hyperplane with the maximum margin between the classes. The main advantage of SVM approach is the formulation of its learning problem. By utilizing the quadratic optimization task, SVM reduces the number of operations in the learning mode. Therefore, SVM algorithm is usually much quicker with respect to other classification methods.

SVM is a linear classifier and a kernel function should be used with SVM to achieve non-linear classification. A kernel function K(x, y) transforms the original data space into a new space with higher dimension. There are different kernel functions i.e. linear, radial basis function, sigmoid, polynomial, etc. and for a specific dataset, choosing the best kernel function with the optimum parameters is an important step.

In this study, we investigate the comparison of using three different kernel functions (sigmoid, radial basis function (RBF) and polynomial which are listed in Table 3.1) at the SVM algorithm. Each kernel function has particular parameters that must be optimized to obtain the best performance result.

Table 3.1. *Functions and Optimization Parameters of Sigmoid, RBF and Polynomial Kernels*

Kernel Name	Function	Optimization Parameters
Sigmoid	$K(x, y) = \tanh(\gamma(x^T y) + c)$	$\gamma = \dfrac{1}{2\sigma^2}$ and c
RBF	$K(x, y) = \exp(-\gamma\|x - y\|^2)$	$\gamma = \dfrac{1}{2\sigma^2}$
Polynomial	$K(x, y) = (\gamma(x^T y) + c)^d$	$\gamma = \dfrac{1}{2\sigma^2}, c$ and d

The classification results and the performance of the proposed features are given in Section 4.

CHAPTER 4

RESULTS

Performance of the proposed algorithm is presented in this section. For comparison, Histogram of oriented Gradients (HoG) feature extraction method [21-23] and Edge Histogram Descriptor (EHD) feature extraction method [20] are also implemented and the performance results are shown in the following sub-sections.

4.1. Dataset

In this study, simulation experiments are carried out to evaluate the proposed landmine discrimination algorithm by using gprMax electromagnetic modeling software [102, 109]. For the simulations, PMA, PMD and PMN are modelled as landmines; buried tin box, plastic box, wooden box and stone are modelled as innocuous objects. To model clutter, a few small pebbles are located in the vicinity of a buried landmine or innocuous object. A sample gprMax input file is given in Appendix C.
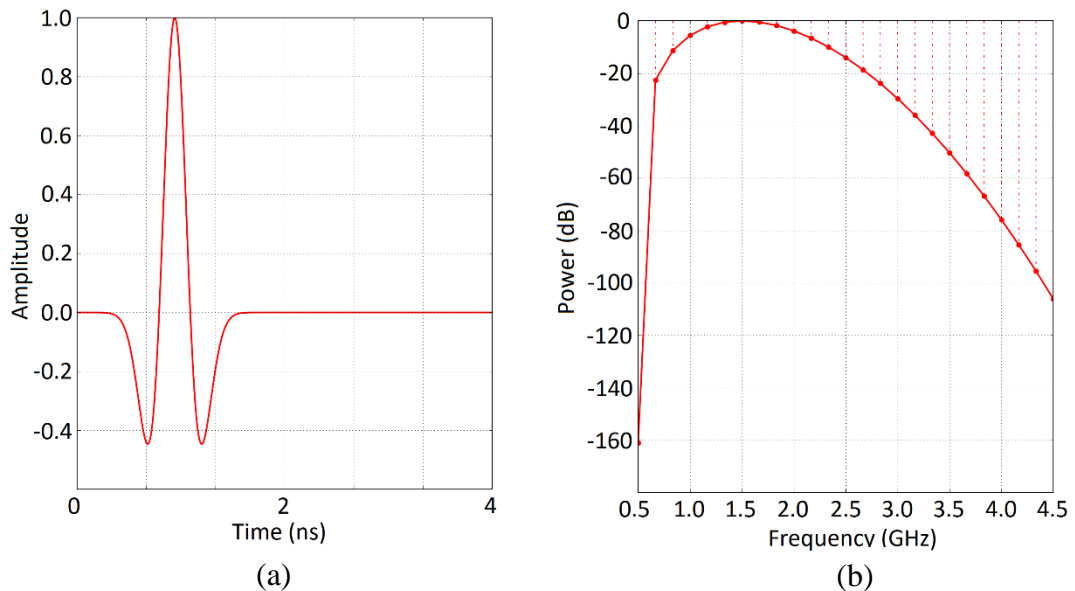

(a)   (b)

Figure 4.1. (a) Time Domain of Ricker Waveform, (b) Power Spectrum of Ricker Waveform

For the simulation, Hertzian dipole antenna and ricker waveform (which is also known as "Mexican hat") are used with the center frequency of 1.5 GHz. Time domain and power spectrum of the ricker waveform is shown in Figure 4.1. According to the power spectrum of the ricker waveform, -10 dB frequency bandwidth of the antenna is from 0.8 to 2.3 GHz. The transceiver and receiver are located 16 cm above the air – soil interface. The distance between transceiver and receiver is 3 cm as shown in Figure 4.2.
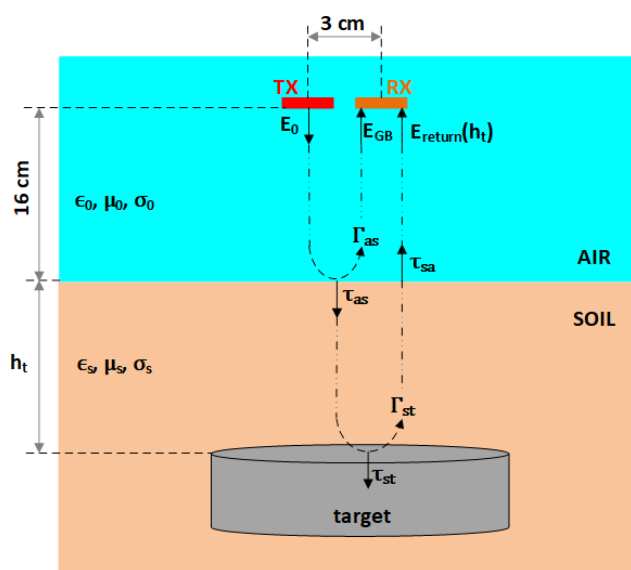

Figure 4.2. GPR Measurement Setup

For the simulations, 12 different soil types are created with permeability μ_0, relative permittivity between 4.5 to 10 and conductivity of 10 mS/m [95, 96, 110-113]. These soil types and relative dielectric properties are shown in Table 4.1.

Table 4.1. *Different Soil Types and Their Dielectric Properties*

Soil Type	1	2	3	4	5	6	7	8	9	10	11	12
Relative Permeability	1	1	1	1	1	1	1	1	1	1	1	1
Relative Permittivity	4.5	5.0	5.5	6.0	6.5	7.0	7.5	8.0	8.5	9.0	9.5	10.0
Conductivity (mS/m)	10	10	10	10	10	10	10	10	10	10	10	10

68

In general, soil is composed of sand, silt and clay particles. A fine concentration of them (around 40-50-10% respectively) is called as loam. These proportions can change and result in different loam types: sandy loam, silt loam, silt clay loam and loam. When the volumetric moisture content is $0.14 - 0.18\ cm^3/cm^3$ (that corresponds to a little wet a little dry soil 1-2 days after a rain), relative permittivity and electrical conductivity of sandy loam, loam, silt loam and silt clay loam are given in Table 4.2 for 1.5 GHz frequency [96, 111].

Table 4.2. *Dielectric Constants of Different Soil Types at 1.5 GHz Frequency*

Soil Type	Sand (%)	Silt (%)	Clay (%)	Dielectric Constant (ϵ_r)	Electrical Conductivity (ms/m)
Sandy loam	~ 50	~ 35	~ 15	~ 7.9 – 10	~ 0.1 – 1.5
Loam	~ 40	~ 50	~ 10	~ 7 – 9.2	~ 3.8 – 15
Silt loam	~ 20	~ 65	~ 15	~ 6 – 8.2	~ 1.7 – 15
Silt clay loam	~ 5	~ 47.5	~ 47.5	~4.5 – 6.6	> 10

To generate more realistic scenarios, a few random pebbles are created and located around the buried objects. Initially, landmines and innocuous objects are buried into these 12 different soil types at 3 different burial depths (10, 12 and 15 cm) without any pebbles and simulation results are collected. Then, 5 pebbles are located in the vicinity of the buried objects and simulations are repeated. Pebbles are modeled as spheres such that the radius is chosen randomly between 1.5 to 2.5 cm and the location is also chosen randomly around the buried object. Finally, 10 pebbles are located in the vicinity of the buried objects and simulations are repeated again. All in all, there are 12 different soil types, 3 different burial depths and 3 different pebble conditions (no pebble, 5 pebbles and 10 pebbles), hence 12x3x3=108 different simulation results are generated for each object.

4.1.1. Simulated Landmine Data

For the simulations, three different landmines (PMA, PMD and PMN) are used. PMA is an anti-personnel blast mine manufactured in the former Yugoslavia [114]. It is a

plastic box mine that is usually colored dark green. PMD is a rectangular wooden anti-personnel blast mine [115]. It is usually either unpainted wood or olive-green color. PMN is a bakelite-cased, pressure operated, anti-personnel blast mine manufactured in the former Soviet Union [116]. The mine has a body that is usually raw (reddish-brown) bakelite with a black rubber top. Pictures and dimensions of PMA, PMD and PMN landmines are given in Figure 4.3 and Table 4.3 respectively.
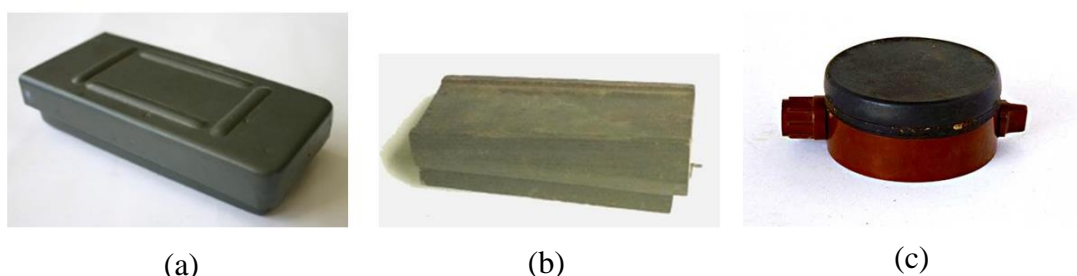

(a) (b) (c)
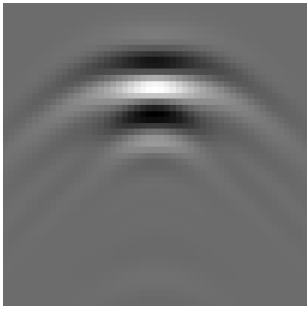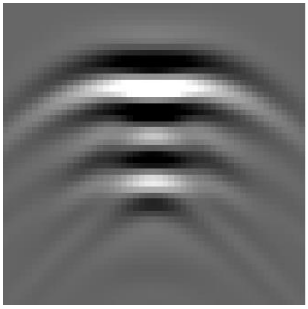
Figure 4.3. (a) PMA Landmine, (b) PMD Landmine, (c) PMN Landmine
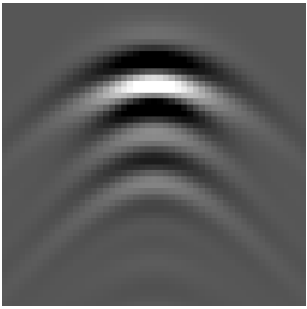
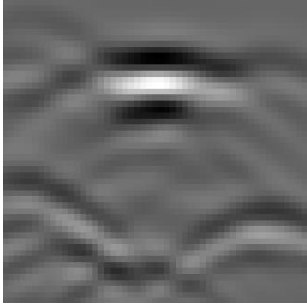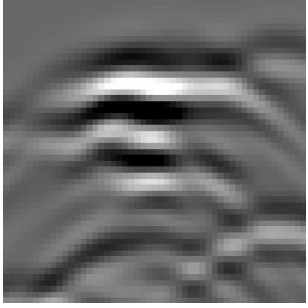Table 4.3. *Simulated Landmine Dimensions*

| Landmine | Casing | | | | | | Explosive Charge |
| | Material | Dimensions | | | | | |
		Width (mm)	Length (mm)	Radius (mm)	Height (mm)	Wall-thickness (mm)	
PMA	Plastic	70	140	-	30	3	200 g TNT
PMD	Wood	90	190	-	65	3	200 g TNT
PMN	Bakelite, rubber	-	-	56	56	3	200 g TNT

By using gprMax modeling software, PMA is modelled as full of TNT inside a plastic casing with 3 cm x 7 cm x 14 cm dimensions and 3 mm wall thickness. PMD is modelled as full of TNT inside a wooden casing with 6.5 cm x 9 cm x 19 cm dimensions and 3 mm wall thickness. PMN is modelled as full of TNT inside a bakelite casing with 112 mm diameter, 56 mm height and 3 mm wall thickness. Moreover, the rubber top with 3 mm thickness and a metallic cylindrical fuse with 4 mm diameter and 56 mm height at the middle of PMN are also modelled. Then, these landmines are buried into 12 different soil types at 3 different burial depths for each 3

different pebble conditions. For each case, GPR antenna is moved through cross-track (x) direction above the target and an A-Scan measurement is taken at each cm ($\Delta x = 1\ cm$). For each target, total of 51 A-Scan data are measured to generate a B-Scan image. Finally, 12x3x3x3=324 different B-Scan images are generated which belong to the simulated landmine data. As example, simulation results of landmine models for a sample soil type are given in Table 4.4.

Table 4.4. *Simulation Results of Landmine Models*

4.1.2. Simulated Innocuous Object Data

For the simulations, four different innocuous objects (tin box, plastic box, wooden box and stone) are used. Pictures and dimensions of innocuous objects are given in Figure 4.4 and Table 4.5 respectively.
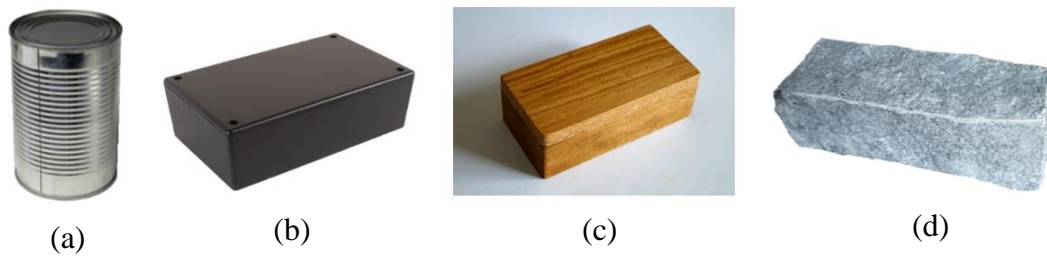
Figure 4.4. (a) Tin Box, (b) Plastic Box, (c) Wooden Box, (d) Stone

Table 4.5. *Simulated Innocuous Objects' Dimensions*

Clutter	Material	Dimensions				
		Width (mm)	Length (mm)	Radius (mm)	Height (mm)	Wall-thickness (mm)
Tin Box	Aluminum	-	-	40	80	3
Plastic Box	Plastic	70	140	-	30	3
Wooden Box	Wood	90	190	-	65	3
Stone	Sandstone	70	140	-	30	-

By using gprMax modeling software, the first innocuous object is modelled as an empty cylindrical aluminum box with 4 cm radius, 8 cm length and 3 mm wall thickness. The second object is modelled as an empty plastic box with 3 cm x 7 cm x 14 cm dimensions and 3 mm wall thickness. The third object is modelled as an empty wooden box with 6.5 cm x 9 cm x 19 cm dimensions and 3 mm wall thickness. The last object is modelled as a stone with 3 cm x 7 cm x 14 cm dimensions (same dimensions with PMA landmine) and 1 cm surface roughness. Then, these innocuous objects are buried into 12 different soil types at 3 different burial depths for each 3 different pebble con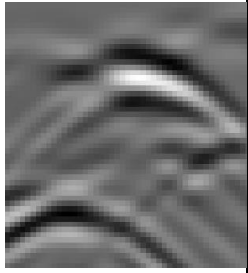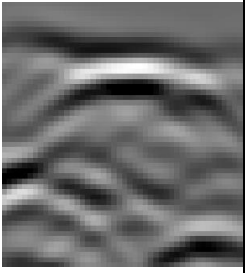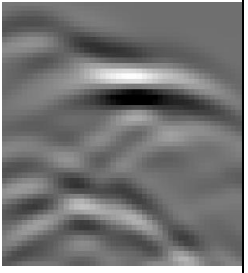ditions. For each case, GPR antenna is moved through cross-track (x) direction above the target and an A-Scan measurement is taken at each cm ($\Delta x = 1\ cm$). For each target, total of 51 A-Scan data are measured to generate a B-Scan image. Finally 12x3x3x4=432 different B-Scan images are generated which belong to the simulated innocuous objects. As example, simulation results of these models for a sample soil type are given in Table 4.6.

Table 4.6. *Simulation Results of Innocuous Objects*

	Tin Box	Plastic Box	Wooden Box	Stone
Without any clutter				
With random clutters				

4.2. Proposed Features / HoG Features / EHD Features Classification and Comparison ROC Curves

For the simulated landmine and innocuous object data, HoG features, EHD features and the proposed features in this study are extracted. HoG and EHD feature extraction algorithms are applied as described in Section 2.3.4 and 2.3.5 respectively. For the proposed feature extraction algorithm, the calibration object is chosen as a cylindrical PEC with 4 cm length and 10 cm diameter. Dielectric feature, energy feature and geometry feature are extracted and two-class support vector machine (SVM) algorithm is used for classification. For HoG and EHD features, SVM algorithm is also used for classification. Initially the best kernel match and optimum parameters are calculated for HoG, EHD and the proposed features; then the performance metrics of these features are computed by using the pre-determined kernel functions.

In this study, 324 landmine data and 432 innocuous object data are simulated as given in Section 4.1. Initially, 150 landmine data are selected for parameter optimization step and another 150 landmine data are selected for performance evaluation step.

Similarly, 150 innocuous object data are selected for parameter optimization step and another 150 innocuous object data are selected for performance evaluation step as shown in Figure 4.5. Note that, the selected data for parameter optimization step and performance evaluation step are different.
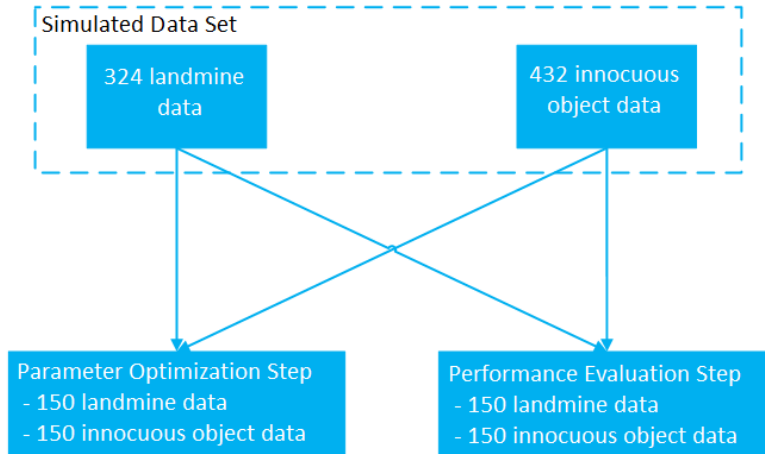
Figure 4.5. Data Allocation for Parameter Optimization and Performance Evaluation

The selected data for parameter optimization step is used to choose the best kernel function with the optimum parameters to achieve the highest performance. In parameter optimization step, the same dataset is used for HoG features, EHD features and the proposed features to make a fair comparison. Afterwards, the selected data for performance evaluation step is used to evaluate the performance of HoG features, EHD features and the proposed features. In this step, SVM algorithm is used with the selected kernel function and the optimum parameters. To implement SVM, "fitcsvm" command of MATLAB is used. To evaluate the performance, 10-fold cross-validation method is applied. For this, "crossval" and "kfoldPredict" commands of MATLAB are used. After this step, performance metrics (accuracy, receiver operating characteristics (ROC) curve and area under curve (AUC)) are obtained and compared for three different features (HoG, EHD and the proposed features). To draw ROC curve, "perfcurve" command of MATLAB is used. The flowchart of this step is given in Figure 4.6.
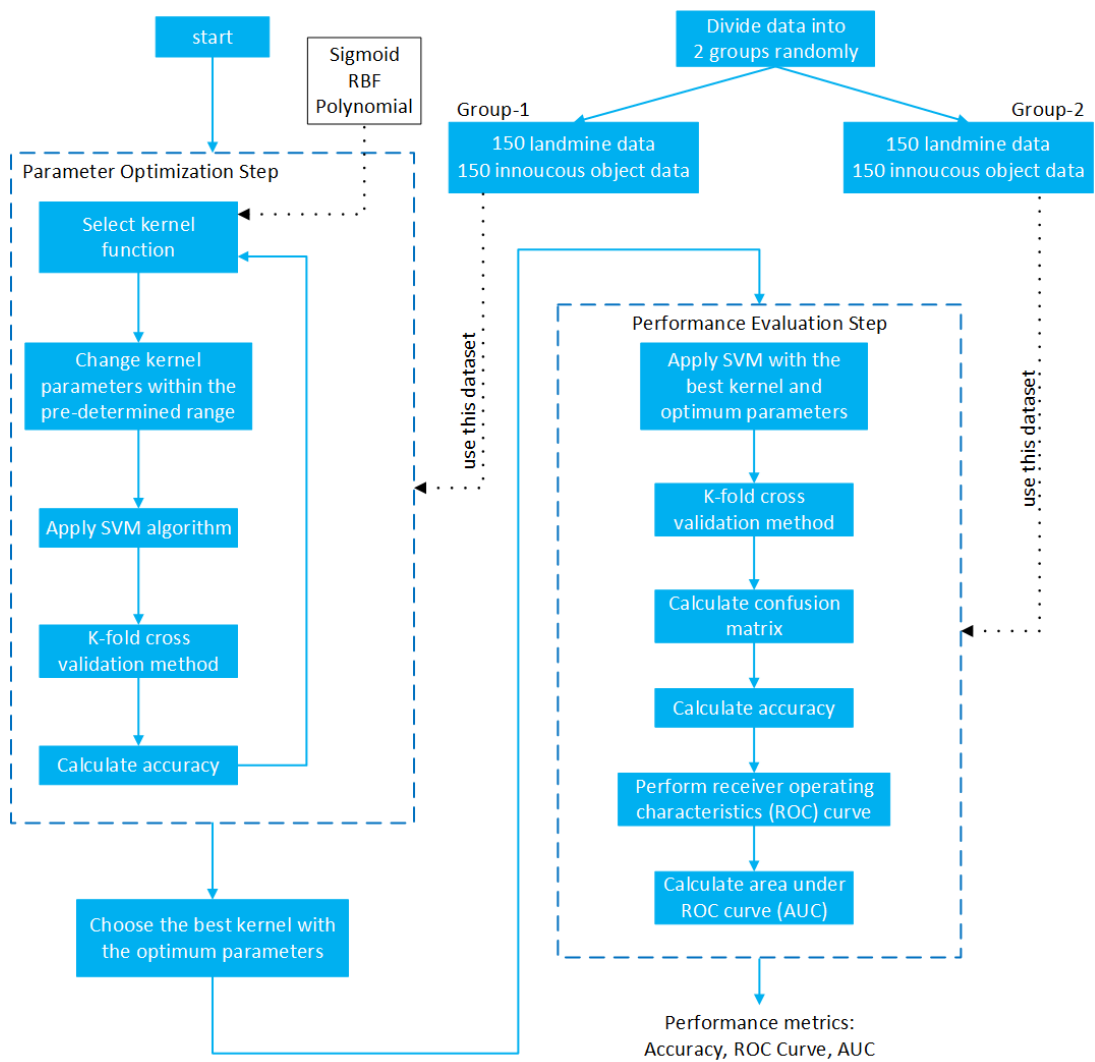
Figure 4.6. Parameter Optimization and Performance Evaluation Steps

Parameter optimization and performance evaluation steps are applied for HoG features, EHD features and the proposed features separately.

4.2.1. Kernel Selection and Parameter Optimization

In this section, firstly HoG features, EHD features and the proposed features in this study are extracted for 300 data (150 landmine and 150 innocuous objects) that are selected for parameter optimization step. Afterwards, performance of SVM with different kernel functions is evaluated for these features by using 10-fold cross validation. As explained in Section 3.5, sigmoid, RBF and polynomial kernel

functions are used in this study. Parameters of these kernels are given in Table 3.1. During parameter optimization step, σ value is changed between 0 and 25 (σ ∈ (0, 25]), c value is changed between 0 and 10 (c ∈ [0, 10]) and d value is changed between 1 and 5 (d ∈ [1, 5]). (Note that, σ = 0 value is not chosen to prevent zero division ($\gamma = \frac{1}{2\sigma^2}$). Instead, σ = 10^{-3} is taken for the minimum value of σ). Within these ranges, sigmoid kernel function is optimized in two-dimensional parameter space (σ and c), RBF kernel function is optimized in one-dimensional parameter space (σ) and polynomial kernel function is optimized in three-dimensional parameter space (σ, c and d). For all different σ, c and d values, accuracies of SVM are evaluated by using these kernel functions. Accuracy is a reliable performance metric for SVM that can be calculated as given in Eq. 72.

$$accuracy = \frac{TP+TN}{TP+FN+TN+FP}, \tag{72}$$

where TP: True positive (a landmine is classified correctly – correct detection)
TN: True negative (an innocuous object is classified correctly – correct rejection)
FN: False negative (a landmine is classified as an innocuous object – miss)
FP: False positive (an innocuous object is classified as a landmine – false alarm)

According to Eq. 72, accuracy values of SVM for HoG features of the selected data for parameter optimization step are calculated by using sigmoid kernel function. Accuracy values for different parameters are shown in Figure 4.7.
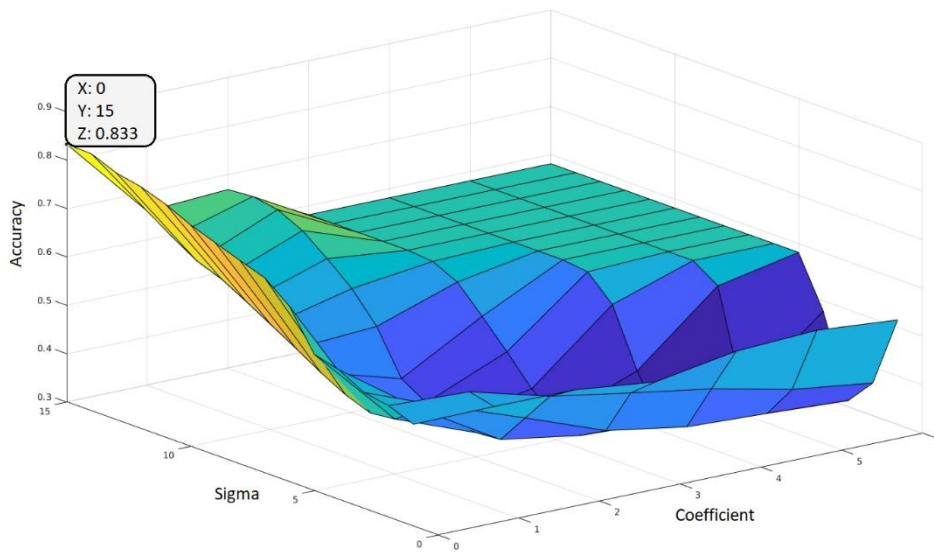
Figure 4.7. Accuracy Values of SVM for HoG Features by Using Sigmoid Kernel

According to Figure 4.7, accuracy of SVM for HoG features is maximum when the coefficient of the sigmoid kernel is 0. However, in the figure it is difficult to identify the optimum sigma value which makes the accuracy maximum. Therefore, while coefficient is 0, sigma value is changed from 0 to 25 to detect the optimum sigma value. As shown in Figure 4.8, when coefficient is 0 and the sigma value is 17, accuracy of SVM with sigmoid kernel is 0.8354 for HoG features.
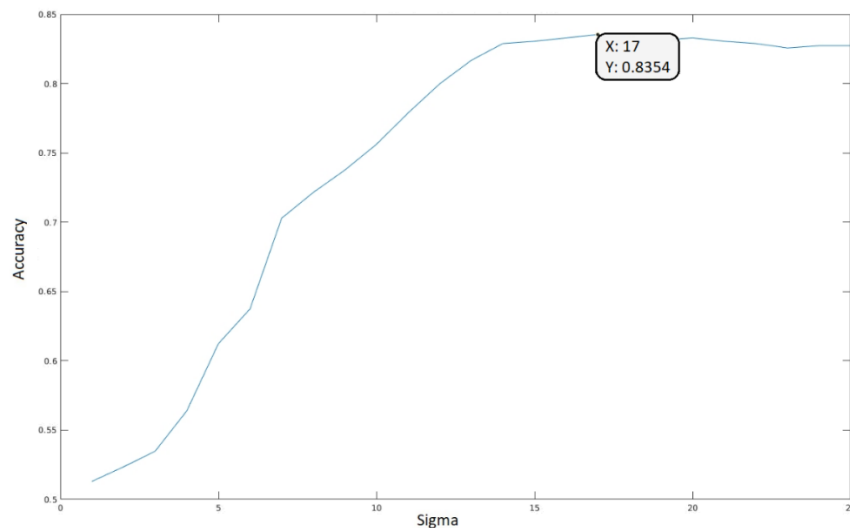
Figure 4.8. Accuracy Values of SVM for HoG Features by Using Sigmoid Kernel with Coefficient=0

Accuracy values of SVM for HoG features of the selected data for parameter optimization step are calculated by using RBF kernel function. Accuracy values for different parameters are shown in Figure 4.9. According to the figure, accuracy of SVM for HoG features is maximum when the parameter of RBF kernel is chosen as sigma is 10. For this parameter, accuracy of SVM is 0.8887 for HoG features.

Figure 4.9. Accuracy Values of SVM for HoG Features by Using RBF Kernel

Accuracy values of SVM for HoG features of the selected data for parameter optimization step are calculated by using polynomial kernel function. Accuracy values for different parameters are shown in Figure 4.10 and 4.11. According to the figures, accuracy of SVM for HoG features is maximum when the parameters of polynomial kernel are chosen as sigma is 2, degree is 2 and coefficient is 2. For these parameters, accuracy of SVM is 0.8998 for HoG features.

Figure 4.10. Accuracy Values of SVM for HoG Features by Using Polynomial Kernel with Degree=2
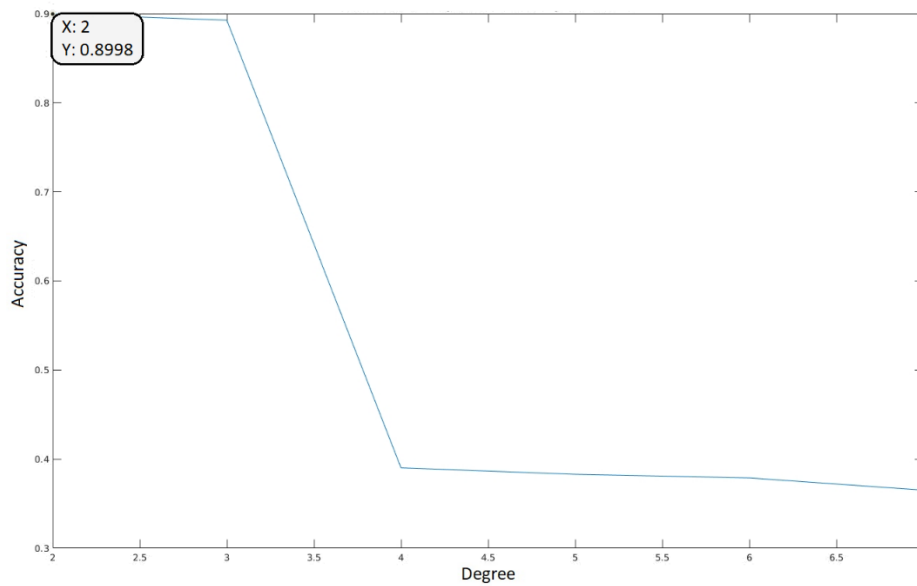
Figure 4.11. Accuracy Values of SVM for HoG Features by Using Polynomial Kernel with Sigma=2, Coefficient=2

According to Eq. 72, accuracy values of SVM for HoG features of the selected data for parameter optimization step are calculated by using sigmoid, RBF and polynomial kernel functions. Results are given in Figures 4.7-11 and the optimum parameters are shown in Table 4.7.

Table 4.7. *Accuracy of SVM for HoG Features by Using Different Kernels*

Kernel	Optimum Parameters	Accuracy
Sigmoid	$\sigma = 17$ and $c = 0$	0.8354
RBF	$\sigma = 10$	0.8887
Polynomial	$\sigma = 2, c = 2$ and $d = 2$	0.8998

Accuracy values of SVM for EHD features of the selected data for parameter optimization step are calculated by using sigmoid kernel function. Accuracy values for different parameters are shown in Figure 4.12.

Figure 4.12. Accuracy Values of SVM for EHD Features by Using Sigmoid Kernel

According to Figure 4.12, accuracy of SVM for EHD features is maximum when the coefficient of the sigmoid kernel is 0. However, in the figure it is difficult to identify the optimum sigma value which makes the accuracy maximum. Therefore, while coefficient is 0, sigma value is changed from 0 to 25 to detect the optimum sigma value. As shown in Figure 4.13, when coefficient is 0 and the sigma value is 14, accuracy of SVM with sigmoid kernel is 0.7266 for EHD features.

Figure 4.13. Accuracy Values of SVM for EHD Features by Using Sigmoid Kernel with
Coefficient=0

Accuracy values of SVM for EHD features of the selected data for parameter optimization step are calculated by using RBF kernel function. Accuracy values for different parameters are shown in Figure 4.14. According to the figure, accuracy of SVM for EHD features is maximum when the parameter of RBF kernel is chosen as sigma is 4. For this parameter, accuracy of SVM is 0.8663 for EHD features.
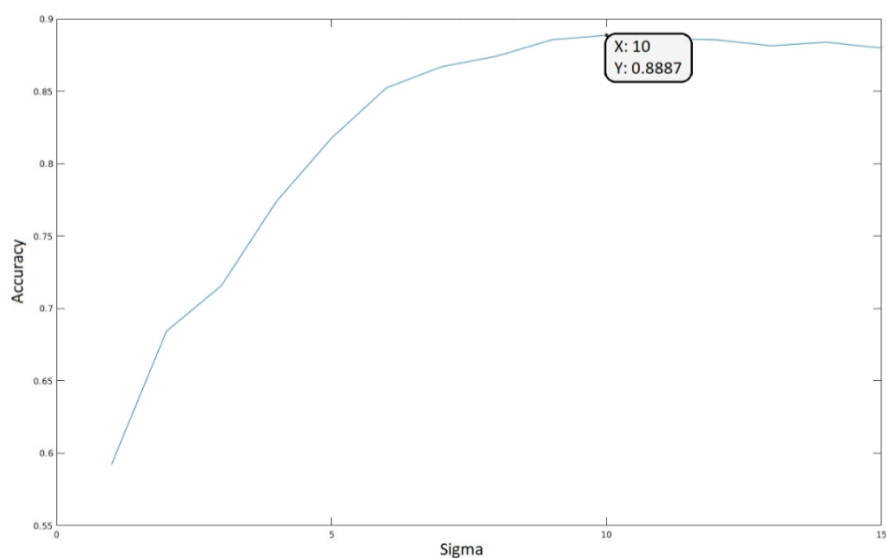

Figure 4.14. Accuracy Values of SVM for EHD Features by Using RBF Kernel

Accuracy values of SVM for EHD features of the selected data for parameter optimization step are calculated by using polynomial kernel function. Accuracy values for different parameters are shown in Figure 4.15 and 4.16. According to the figures, accuracy of SVM for EHD features is maximum when the parameters of polynomial kernel are chosen as sigma is 1, degree is 2 and coefficient is 9. For these parameters, accuracy of SVM is 0.8689 for EHD features.
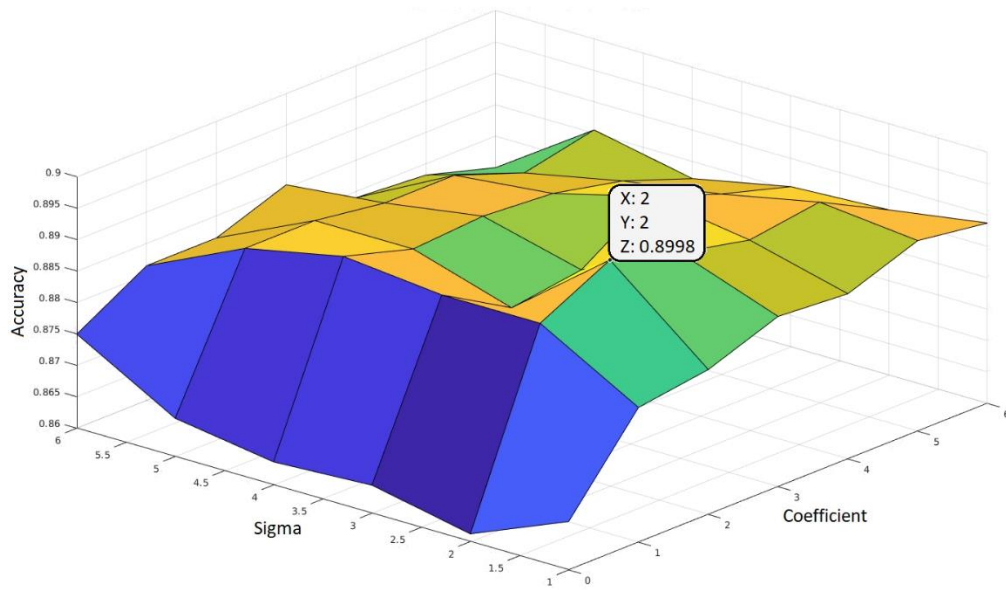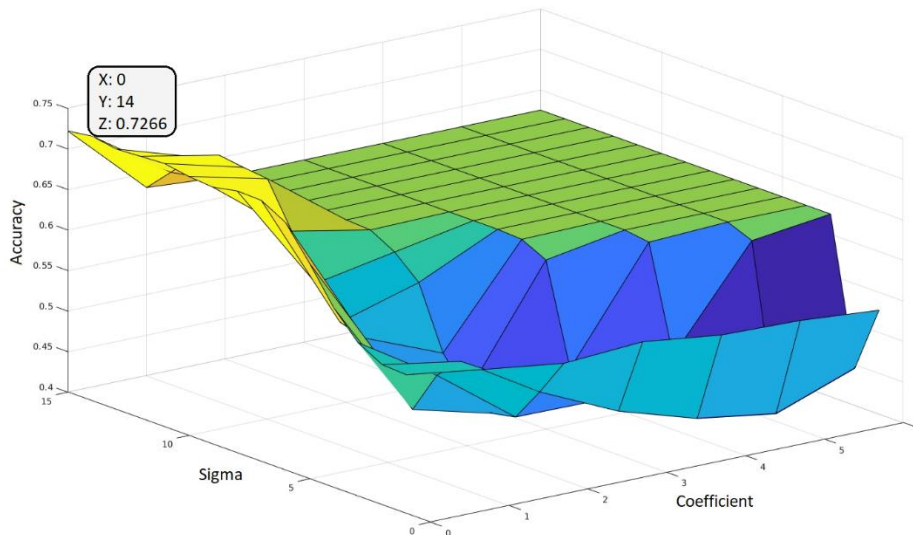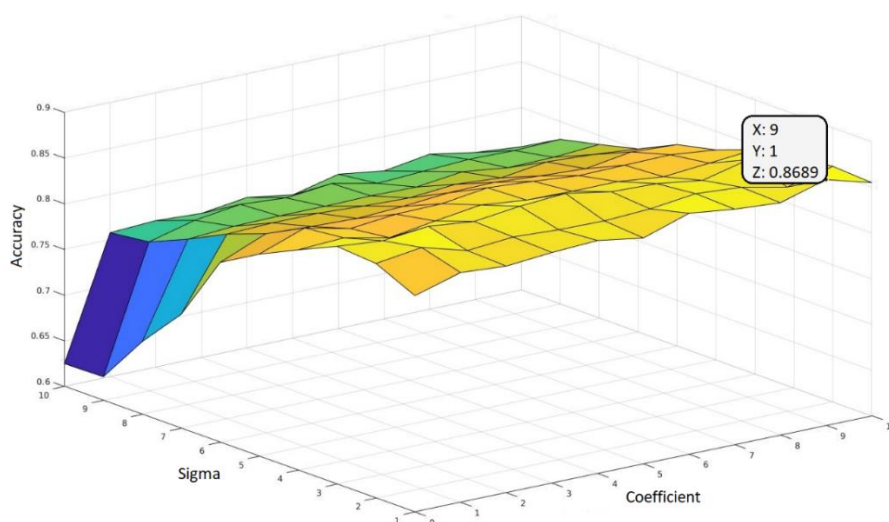

Figure 4.15. Accuracy Values of SVM for EHD Features by Using Polynomial Kernel with Degree=2

Figure 4.16. Accuracy Values of SVM for EHD Features by Using Polynomial Kernel with Sigma=1, Coefficient=9

According to Eq. 72, accuracy values of SVM for EHD features of the selected data for parameter optimization step are calculated by using sigmoid, RBF and polynomial kernel functions. Results are given in Figures 4.12-16 and the optimum parameters are shown in Table 4.8.

Table 4.8. *Accuracy of SVM for EHD Features by Using Different Kernels*

Kernel	Optimum Parameters	Accuracy
Sigmoid	$\sigma = 14$ and $c = 0$	0.7266
RBF	$\sigma = 4$	0.8663
Polynomial	$\sigma = 1, c = 9$ and $d = 2$	0.8689

Accuracy values of SVM for the proposed features of the selected data for parameter optimization step are calculated by using sigmoid kernel function. Accuracy values for different parameters are shown in Figure 4.17.
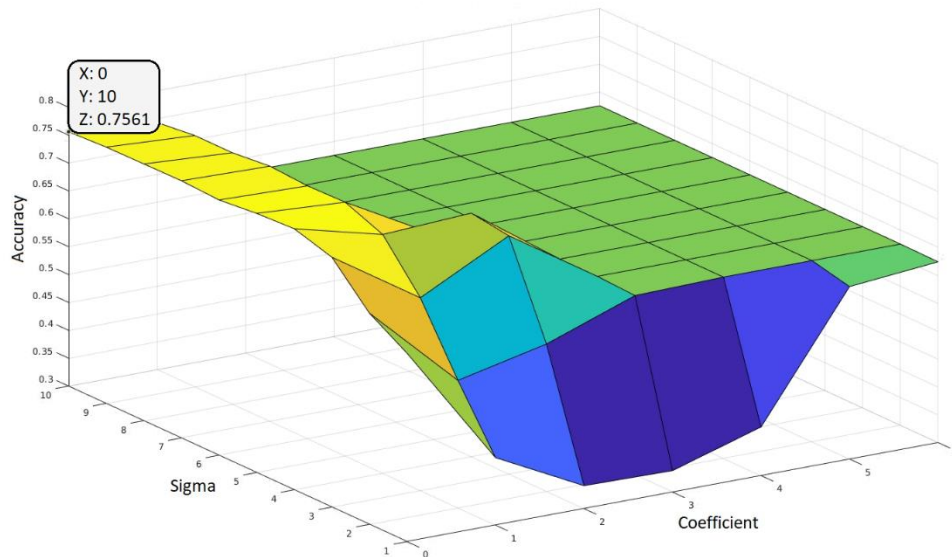
Figure 4.17. Accuracy Values of SVM for the Proposed Features by Using Sigmoid Kernel

According to Figure 4.17, accuracy of SVM for the proposed features is maximum when the coefficient of the sigmoid kernel is 0. However, in the figure it is difficult to

identify the optimum sigma value which makes the accuracy maximum. Therefore, while coefficient is 0, sigma value is changed from 0 to 25 to detect the optimum sigma value. As shown in Figure 4.18, when coefficient is 0 and the sigma value is 4, accuracy of SVM with sigmoid kernel is 0.7674 for the proposed features.
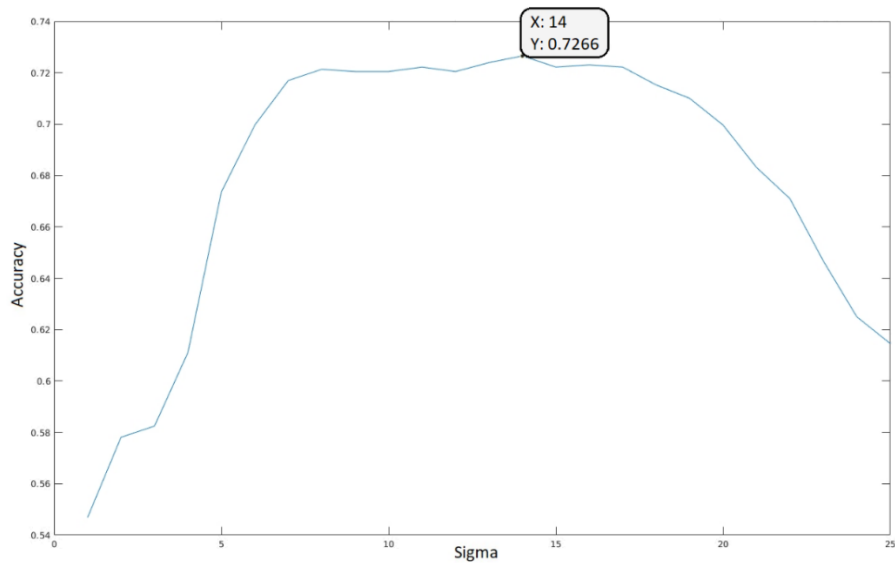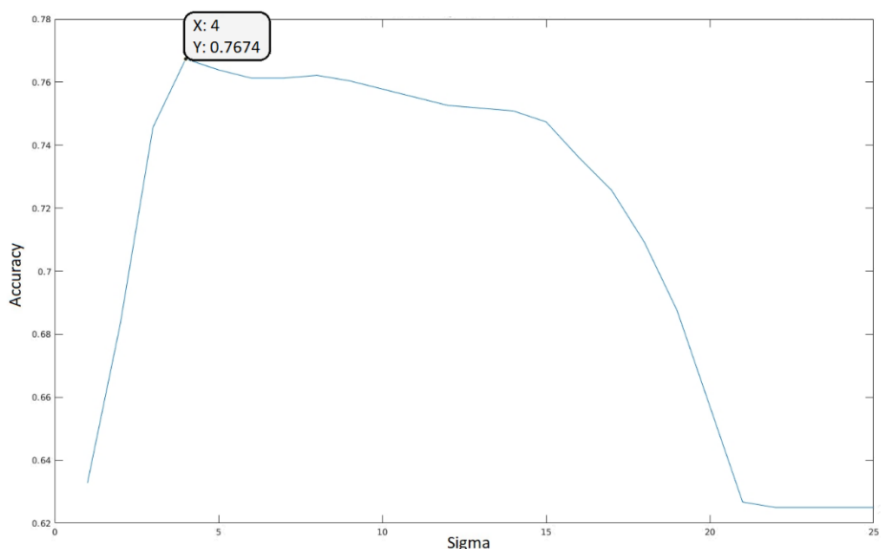

Figure 4.18. Accuracy Values of SVM for the Proposed Features by Using Sigmoid Kernel with Coefficient=0

Accuracy values of SVM for the proposed features of the selected data for parameter optimization step are calculated by using RBF kernel function. Accuracy values for different parameters are shown in Figure 4.19. According to the figure, accuracy of SVM for the proposed features is maximum when the parameter of RBF kernel is chosen as sigma is 0.7. For this parameter, accuracy of SVM is 0.9318 for the proposed features.
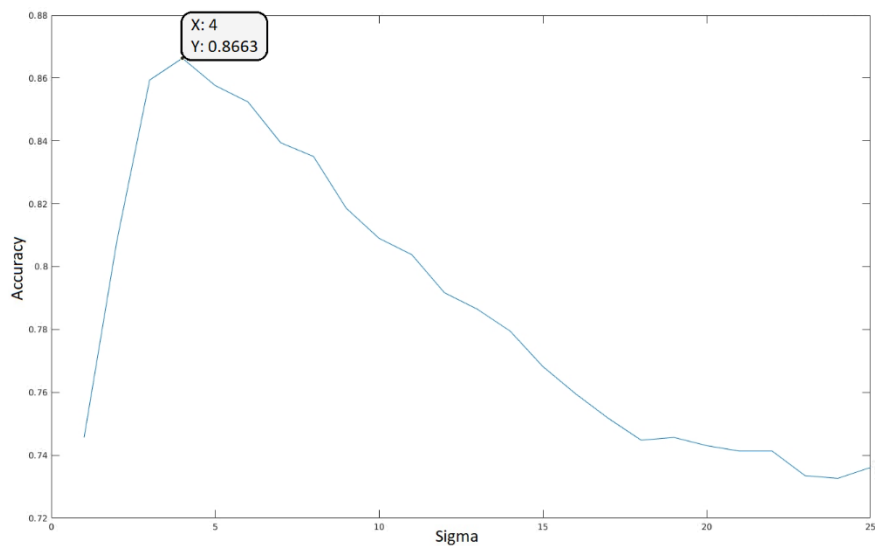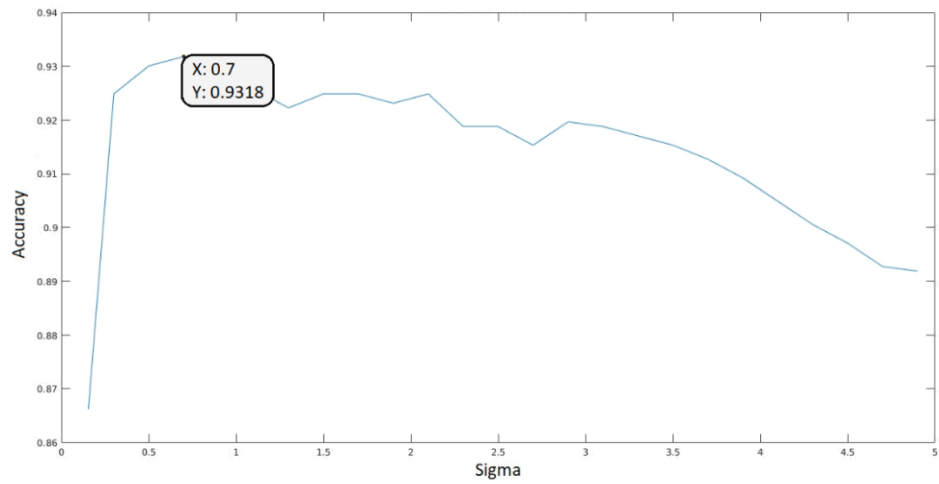
Figure 4.19. Accuracy Values of SVM for the Proposed Features by Using RBF Kernel

Accuracy values of SVM for the proposed features of the selected data for parameter optimization step are calculated by using polynomial kernel function. Accuracy values for different parameters are shown in Figure 4.20 and 4.21. According to the figures, accuracy of SVM for the proposed features is maximum when the parameters of polynomial kernel are chosen as sigma is 0.5, degree is 2 and coefficient is 8. For these parameters, accuracy of SVM is 0.9378 for the proposed features.
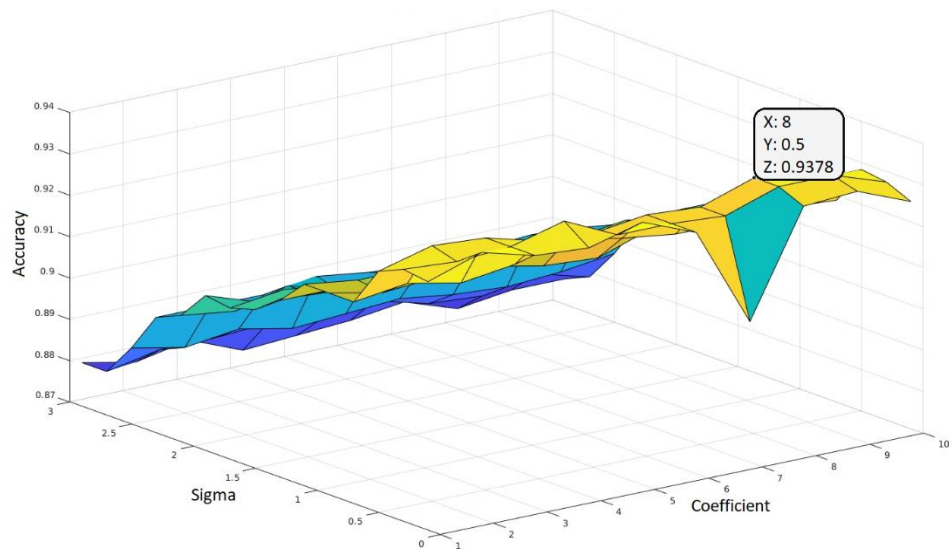
Figure 4.20. Accuracy Values of SVM for the Proposed Features by Using Polynomial Kernel with Degree=2
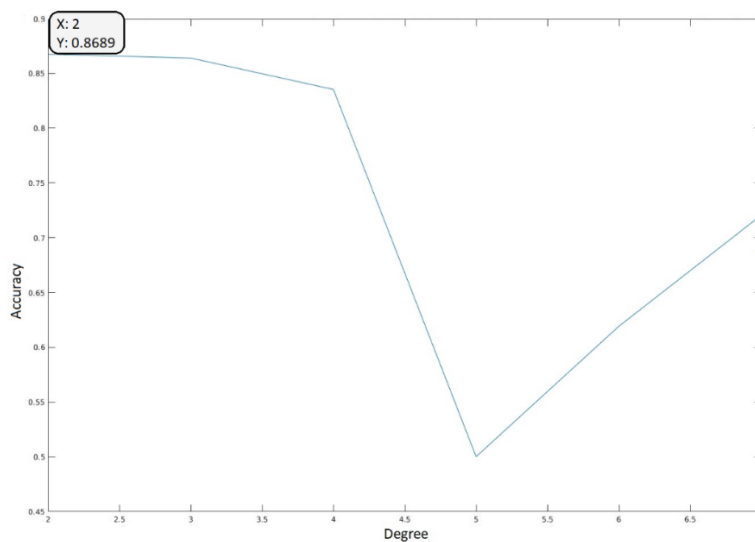
85
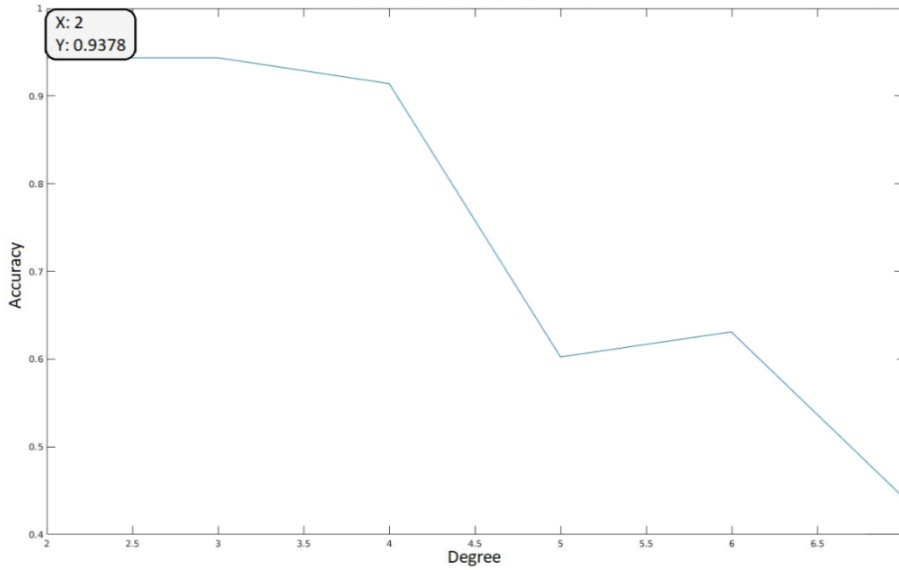
Figure 4.21. Accuracy Values of SVM for the Proposed Features by Using Polynomial Kernel with Sigma=0.5, Coefficient=8

According to Eq. 72, accuracy values of SVM for the proposed features of the selected data for parameter optimization step are calculated by using sigmoid, RBF and polynomial kernel functions. Results are given in Figures 4.17-21 and the optimum parameters are shown in Table 4.9.

Table 4.9. *Accuracy of SVM for the Proposed Features by Using Different Kernels*

Kernel	Optimum Parameters	Accuracy
Sigmoid	$\sigma = 4$ and $c = 0$	0.7674
RBF	$\sigma = 0.7$	0.9318
Polynomial	$\sigma = 0.5, c = 8$ and $d = 2$	0.9378

According to the accuracy values given in Tables 4.7-9, polynomial kernel function gives the best accuracy for all feature types. The optimum parameters for the polynomial kernel are σ=2, c=2 and d=2 for HoG features; σ=1, c=9 and d=2 for EHD features and σ=0.5, c=8 and d=2 for the proposed features in this study. In the next

step, performance of different features will be evaluated by using polynomial kernel function with optimum parameters. Although polynomial kernel gives the best accuracy for all feature types, RBF kernel function gives comparable accuracy values. Since RBF kernel has only one parameter and it is computationally less expensive, RBF kernel may also be used to avoid computational cost.

4.2.2. Performance Evaluation

In this section, HoG, EHD and the proposed features of the selected data for performance evaluation step are classified by SVM with the polynomial kernel function and the optimum parameters. Afterwards, 10-fold cross validation method is used to calculate the performance of HoG, EHD and the proposed features. For the performance evaluation, accuracy of these features is calculated as given in Eq. 72. Moreover, receiver operating characteristics (ROC) curves, area under curve (AUC) values and the confusion matrices are given for comparison.

HoG features, EHD features and the proposed features of the selected data for performance evaluation step are classified by SVM. For each case polynomial kernel function is used with the optimum parameters computed in Section 4.2.1. 10-fold cross validation method is applied to obtain the results. Confusion matrices and the accuracy values are given in Table 4.10.

Table 4.10. *Confusion Matrices and Accuracy values of SVM for HoG, EHD and the Proposed features by using polynomial kernel and optimum parameters computed in Sec 4.2.1*

	HoG Features			EHD Features			Proposed Features		
		actual			actual			actual	
Confusion Matrix	Predicted	TP 138	FP 16	Predicted	TP 121	FP 18	Predicted	TP 143	FP 13
		FN 12	TN 134		FN 29	TN 132		FN 7	TN 137
Accuracy	0.9067			0.8433			0.9333		

87

Finally, Figure 4.22 shows the results (comparison ROC curves and AUC values) obtained from evaluating SVM on the proposed features, HoG features and EHD features using the aforementioned cross-validation procedure.
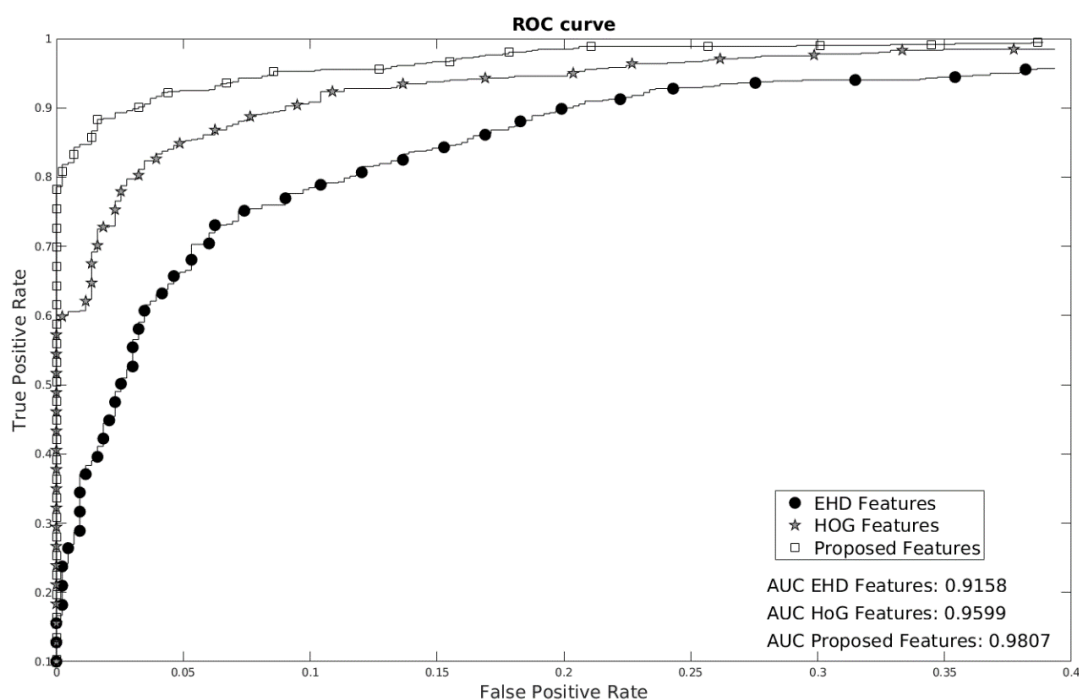
Figure 4.22. Classification Results of the Proposed Features / HoG Features / EHD Features

According to accuracy values, ROC curves and the areas under these curves (AUC values), the proposed features in this study has higher discrimination performance than HoG and EHD features.

4.2.3. Classification and Class Boundaries of Data with the Proposed Features

In Section 4.2.2, performance of the proposed features is given. In this section, classes and class boundaries are shown visually and the accuracy values of dielectric, energy and geometry features are computed separately. Therefore, success of each individual feature and the effect on final result is clarified.

During this study, 324 landmine data and 432 innocuous object data are simulated as given in Section 4.1. To visualize the classes and class boundaries, simulated data is divided into two different sets randomly as shown in Figure 4.5. In this case, the first

data set contains 200 landmine data and 200 innocuous object data while the second data set contains 100 landmine data and 100 innocuous object data. The first data set is classified by SVM with the polynomial kernel and the optimum parameters for the proposed features. This data set is classified with 20 support vectors as given in Figure 4.23.
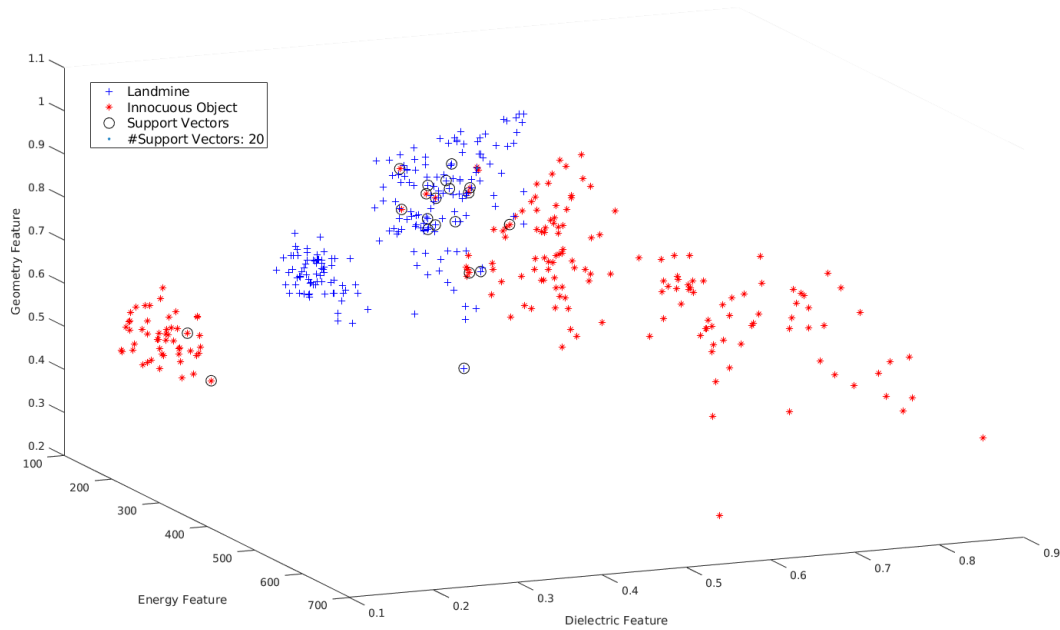
Figure 4.23. Support Vectors of the Simulated Landmine and Innocuous Object Data

In this study, three discriminative features are extracted for landmine identification. Contribution of each feature to the overall performance is evaluated here. As shown in Table 4.10, accuracy of the proposed features for the data set of performance evaluation step is 0.93. For the same data set, accuracy of the dielectric feature is 0.81, accuracy of energy feature is 0.86 and accuracy of geometry feature is 0.76. Moreover, dielectric and energy feature give around 0.91 accuracy together. Therefore, the proposed algorithm has higher discrimination power than HoG and EHD algorithm even if two features (dielectric and energy) are used.

As described above, the simulated data set is divided into two groups such that the first group has 200 landmine data and 200 innocuous object data for training; the

second group has 100 landmine data and 100 innocuous object data for testing. The first data set is classified by SVM with the polynomial kernel and the optimum parameters by using only two features (dielectric and energy). Classes, support vectors and class boundaries are shown in Figure 4.24.
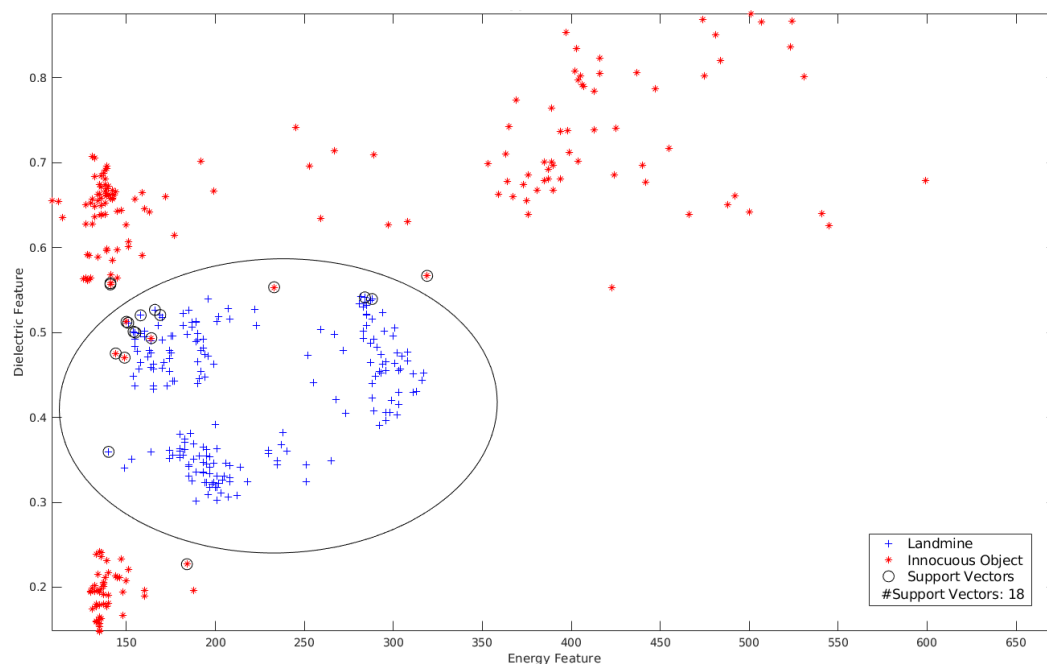
Figure 4.24. Class Boundaries and Support Vectors of the Simulated Data

Afterwards, the second data set is used to test the model. Classification result of the second group, which has 100 landmine data and 100 innocuous object data, is shown in Figure 4.25. In the figure, some data points are numbered. Number 1 and 2 show the landmine data classified as innocuous object (false negative). Number 6-15 show the innocuous object data classified as landmine (false positive). Number 3, 4 and 5 show three landmine data which are classified correctly however very close to the classification boundary. Number 16-21 show the innocuous object data which are on the limits of the feature space.
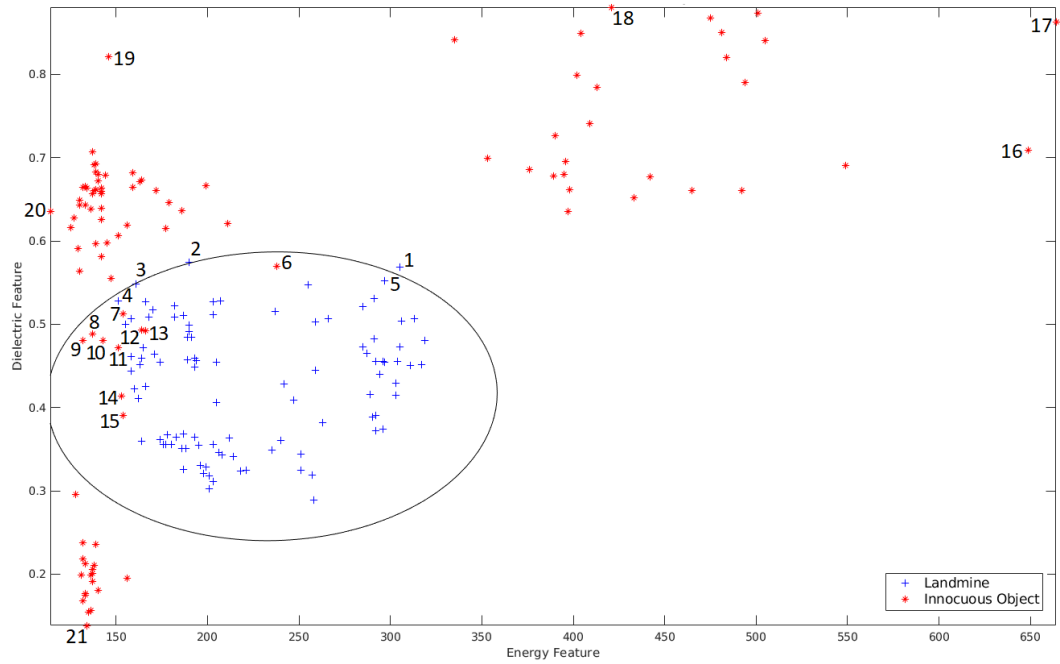
Figure 4.25. Classification Result of the Second Group according to the Model Trained by using the First Group

The simulated data belong to these 21 extreme points are shown in Figure 4.26. Details of the simulation scenarios (buried objects, soil types and burial depths) are given in Table 4.11. These scenarios are used to generate B-Scan images which are shown in Figure 4.26.

(1)   (2)   (3)
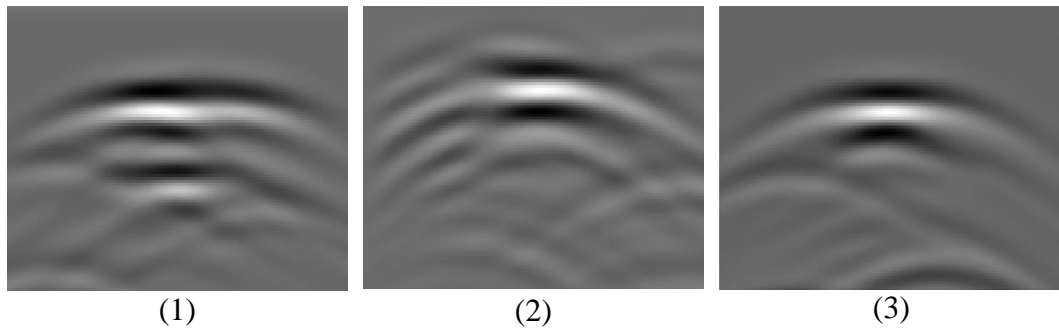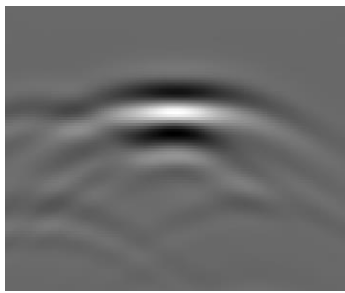
(4)
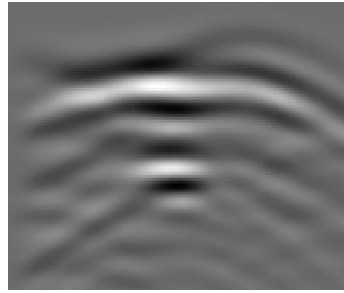
(5)
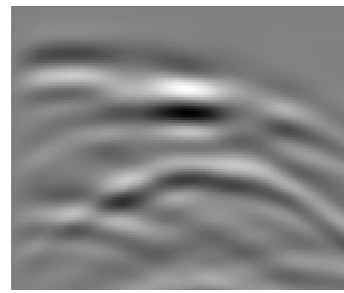
(6)
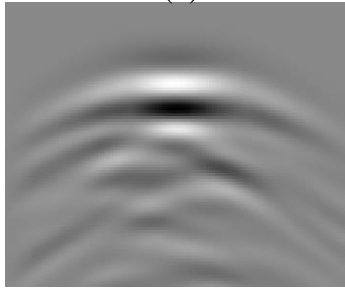
(7)
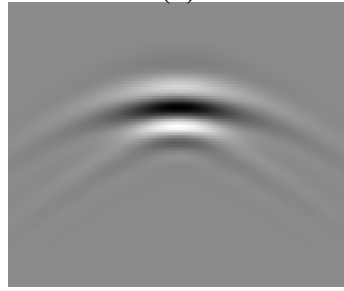
(8)
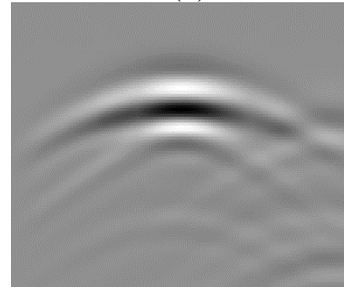
(9)
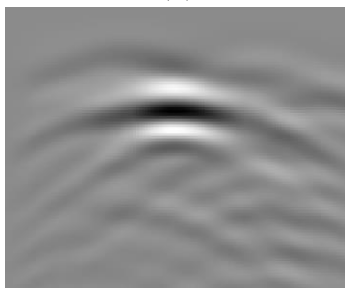
(10)
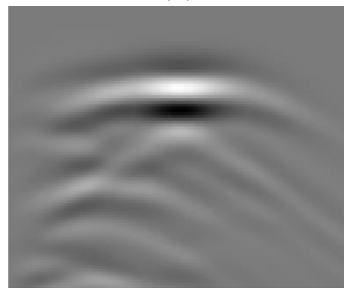
(11)

(12)

(13)

(14)

(15)

(16)

(17)

(18)

(19)   (20)   (21)
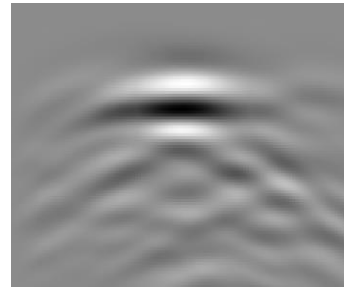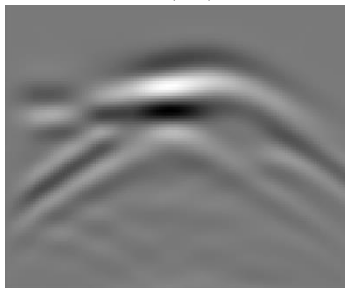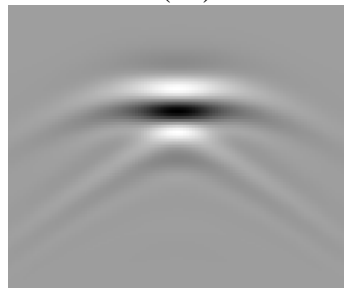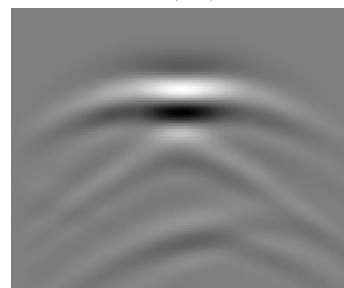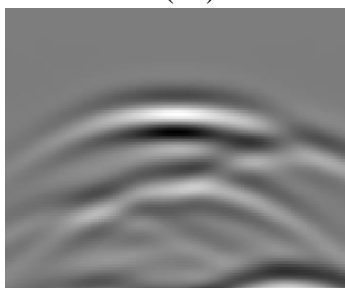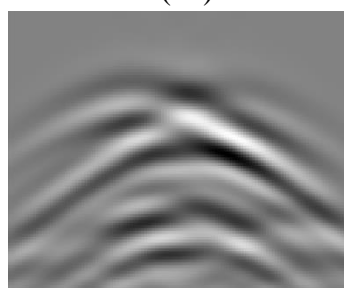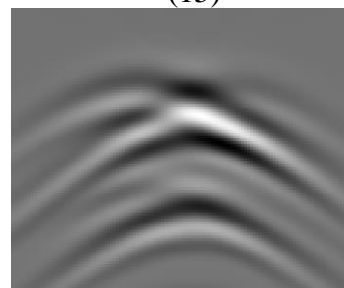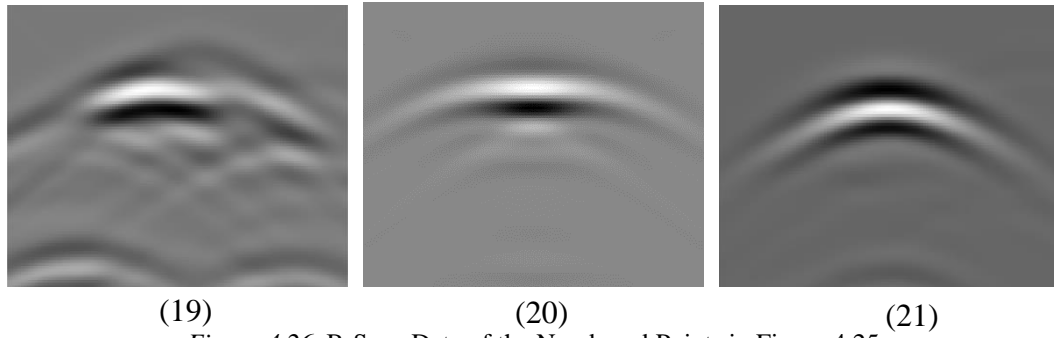
Figure 4.26. B-Scan Data of the Numbered Points in Figure 4.25

Table 4.11. *Simulation Scenarios with respect to B-Scan Images in Figure 4.26*

Data Point	Buried Object	Soil Type	Burial Depth
1	PMD	2	10 cm
2	PMA	8	15 cm
3	PMA	1	12 cm
4	PMA	5	10 cm
5	PMD	11	15 cm
6	Wooden box	8	15 cm
7	Wooden box	11	15 cm
8	Plastic box	10	15 cm
9	Plastic box	10	12 cm
10	Plastic box	10	15 cm
11	Wooden box	7	10 cm
12	Wooden box	11	15 cm
13	Wooden box	11	10 cm
14	Wooden box	10	15 cm
15	Wooden box	10	12 cm
16	Plastic box	1	12 cm
17	Stone	12	12 cm
18	Stone	6	12 cm
19	Plastic box	3	10 cm
20	Wooden box	5	10 cm
21	Tin box	10	10 cm

Up to this point, classification is performed for two different classes as landmine and innocuous object. The proposed algorithm can also classify different landmines and different innocuous objects unless their dielectric properties are very similar. The training data given in Figure 4.24 is also trained for multi-class classification. As shown in Figure 4.27, PMA, PMD and PMN landmines, stone and tin box have distinct classes and class boundaries. Plastic box and wooden box have similar

dielectric properties therefore their classes overlap. All in all, the proposed features can classify the simulated data as PMA, PMD, PMN, stone, tin box and plastic/wooden box as shown in Figure 4.27.
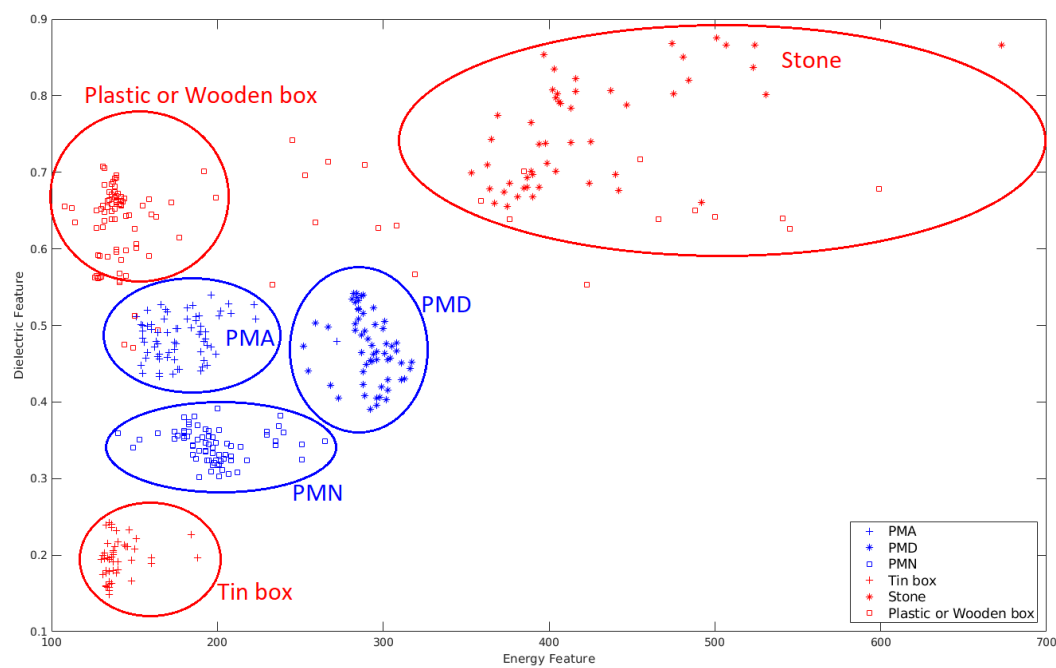
Figure 4.27. Multi-class Classification of the Simulated Data

As explained in Section 2.2.4, the basic steps of machine learning algorithms are training and testing. The algorithm learns a prediction rule based on the training data and applies this rule to classify test data. The training set consists of different categories of data and the prediction rule creates class boundaries based on these categories. For a new test data, which is from a completely new category, the performance of the prediction rule is ambiguous. For instance, our SVM classifier is trained for two class classification as landmine and innocuous object. Simulation data of PMA, PMD and PMN landmines are used to create landmine class boundaries. If a different landmine is tested by using our algorithm and our training data given in Figure 4.24, performance of the algorithm is uncertain. To observe the performance of our algorithm for different types of landmines (without any training data), we create

simulations of PMA-3, Gyata-64 and PPM-2 landmines. Pictures and dimensions of these landmines are given in Figure 4.28 and Table 4.12 respectively.

(a)   (b)   (c)

Figure 4.28. (a) PMA-3, (b) Gyata-64, (c) PPM-2

Table 4.12. *Dimensions of New Landmines*

Landmine	Casing				Explosive Charge
	Material	Dimensions			
		Radius (mm)	Height (mm)	Wall-thickness (mm)	
PMA-3	Rubber	55	40	3	35 g TNT
Gyata-64	Bakelite, rubber	54	61	3	300 g TNT
PPM-2	Plastic	67	60	3	110 g TNT

By using gprMax modeling software, these landmines are modeled into a soil which has relative permeability of 1, permittivity of 4.5 and conductivity of 10 mS/m at 10 cm depth. Then, dielectric feature and energy feature of these three different landmines are calculated. These landmine data are classified correctly by our algorithm as shown in Figure 4.29.
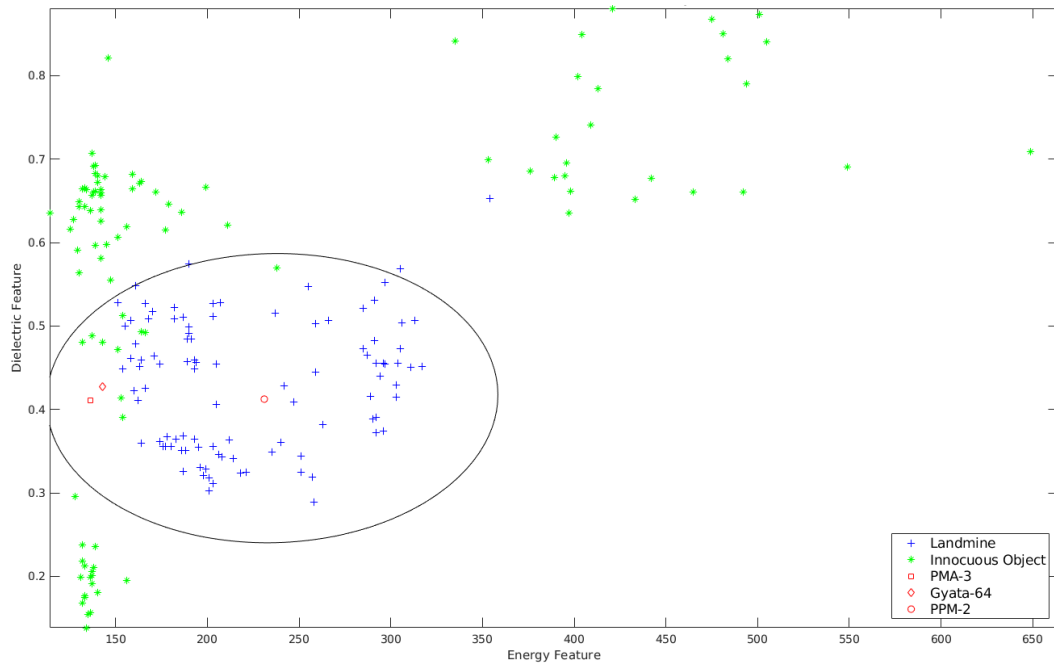
Figure 4.29. Classification Result of New Landmine Data by Our Algorithm

4.3. Complexity of the Proposed Features

In this study, three discriminative features are extracted for an anomaly region and detected targets are classified in a three-dimensional feature space. As explained before, HoG and EHD feature descriptors are 162 and 35-dimensional vectors respectively. To compare the complexity, feature extraction times and classification times of HoG features, EHD features and the proposed features in this study are determined. The extraction times of these features for 100 B-scan image that are randomly selected from the simulated data-set are calculated by MATLAB in a computer that has Intel Core i7-4790 CPU with 3.60 GHz base frequency and 4 Cores. Average feature extraction times of these 100 B-scan images are given in Table 4.13.

Moreover, classification times of these features are calculated such that computation time of SVM training phase and SVM test phase are evaluated separately. To achieve this, simulated data is divided into two different sets randomly as shown in Figure 4.5. In that case the first data set contains 200 landmine data and 200 innocuous object data while the second data set contains 100 landmine data and 100 innocuous object

96

data. The first data set is used to train SVM and the second data set is used for testing the model. MATLAB "fitcsvm" command is used to train SVM model. For two-class classification, fitcsvm uses Sequential Minimal Optimization (SMO) solver. SMO minimizes the soft margin problem given in Eq. 38 by using several two-point minimizations. Details of SMO algorithm is given in [117]. For testing the model, "predict" command is used. To achieve more robust solution, this process is repeated 50 times. Training time and test time are written down for each case. Finally, average of these 50 values is calculated to find the computation time of training phase and test phase. All in all, feature extraction time and classification times are pretty lower for the proposed features with respect to HoG and EHD features as shown in Table 4.13.

Table 4.13. *Extraction and Classification Times of HoG features, EHD Features and the Proposed Features*

Feature	Extraction time (ms)	Classification time (ms)	
		Training Phase	Test Phase
HoG	52.76	489	32.01
EHD	49.66	486	18.38
Proposed	15.21	423	10.49

4.4. Robustness of the Proposed Features

In this study, two of our proposed features are extracted from the mid A-Scan data of a given B-Scan image. If this A-Scan data is not chosen correctly, the resultant features become slightly different. By considering GPR step size and equipment noise, possible errors while choosing the mid A-Scan data and the resultant effects to the proposed features are evaluated.

During simulations, GPR step size is considered as 1 cm. That means, GPR antenna takes measurement at each cm. However, in real experiments it is not always possible. GPR systems generally take one measurement every 5 cm. Therefore, measurement

point may be 3 cm shifted from the position of mid A-Scan data at worst. In that case, dielectric feature and energy feature of the proposed algorithm become slightly different. To evaluate this issue, we have calculated the difference of the proposed features if mid A-Scan data is chosen 3 cm shifted. In Figure 4.30, dielectric and energy features of PMA, PMD, PMN landmines, stone and tin box are shown into different soil types at different burial depths in a clutter-free environment. As shown in the figure, these different objects are completely distinguishable without any clutter. In Figure 4.31, dielectric and energy features of the same data set are calculated again by using 3 cm shifted mid A-Scan data. These new results are given with red symbols. As shown in the figure, these objects are still distinguishable even if the mid A-Scan data is chosen 3 cm shifted.
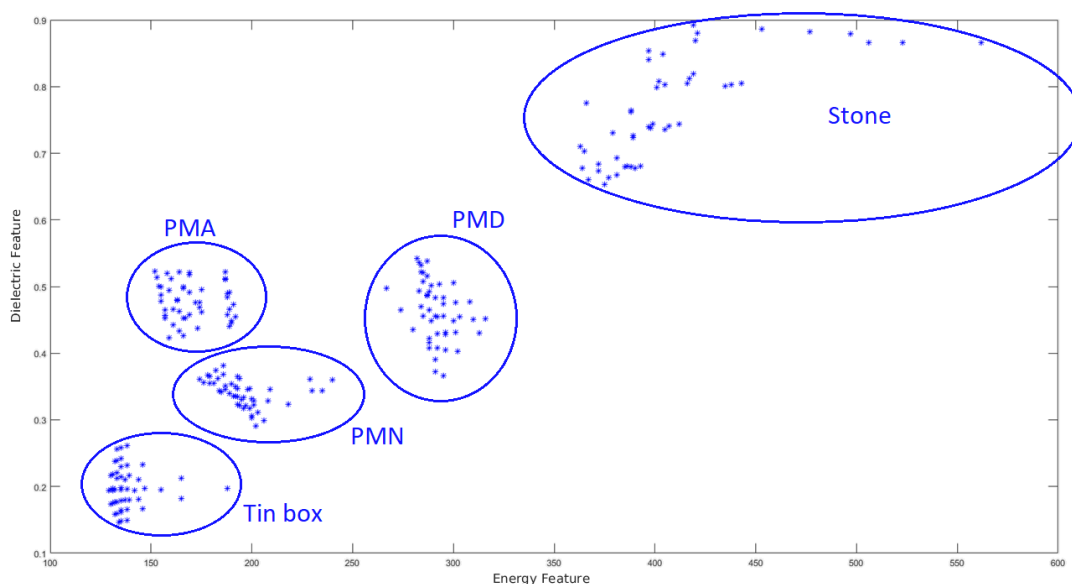
Figure 4.30. Dielectric and Energy Features of Different Objects
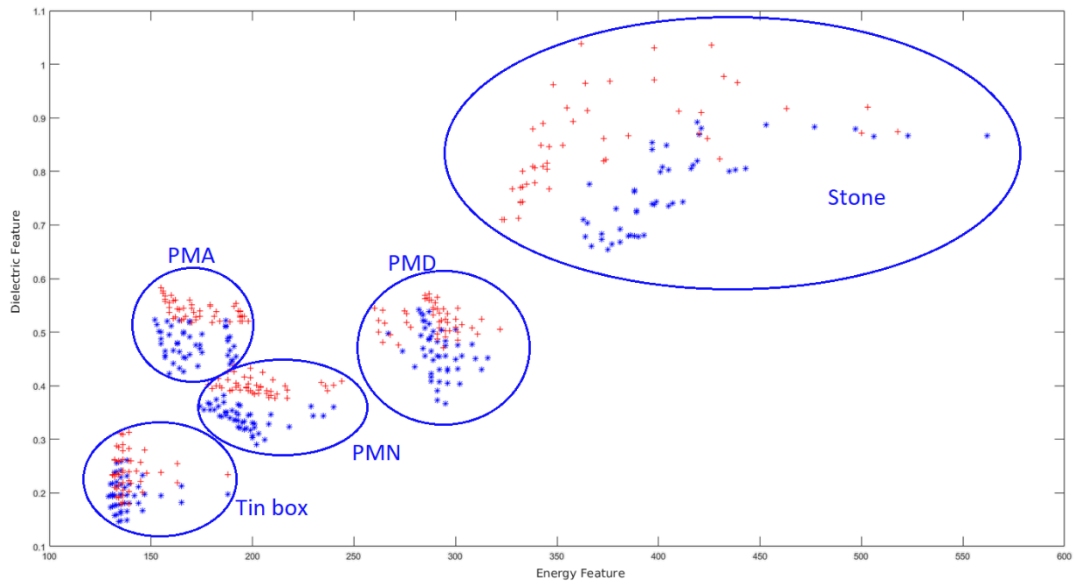
Figure 4.31. Dielectric and Energy Features by using 3 cm Shifted mid A-Scan Data

Moreover, the experiments given in Section 4.2.2 are repeated to calculate the accuracy of the proposed features for shifted measurement results. However, in that case for a given B-Scan image, mid A-Scan data, A-Scan data nearest to mid A-Scan data (1 cm shifted) or A-Scan data second nearest to mid A-Scan data (2 cm shifted) is used. To calculate dielectric feature and energy feature, one of these three A-Scan data is chosen randomly. Finally, performance of the proposed features is computed again. Accuracy value is around 0.9114 which is still higher than the performance of HoG and EHD features.

In this study, calculations are performed for normal incidence of GPR signal from the underground object. Pressure-operated landmines are buried flat on the ground to activate the fuse when a person (or vehicle) passes above the mine. However, during the years the position of the buried landmines may change due to underground movements of earth. Effects of orientations of buried objects to the proposed features are evaluated. In the gprMax modelling software, the cylindrical objects can be placed inclined underground. However, the cornered objects and boxes can only be located parallel to the ground. Therefore, to evaluate the orientation effect, PMN landmine (which has cylindrical shape) is placed inclined from 2-degree to 10-degree orientation

randomly. When orientation increases, dielectric feature and energy feature tend to increase. In Figure 4.32, dielectric and energy features of inclined PMN are given with red symbols. As shown in the figure, some inclined PMN features occur in PMA and PMD classes however they are still distinguishable from innocuous objects.
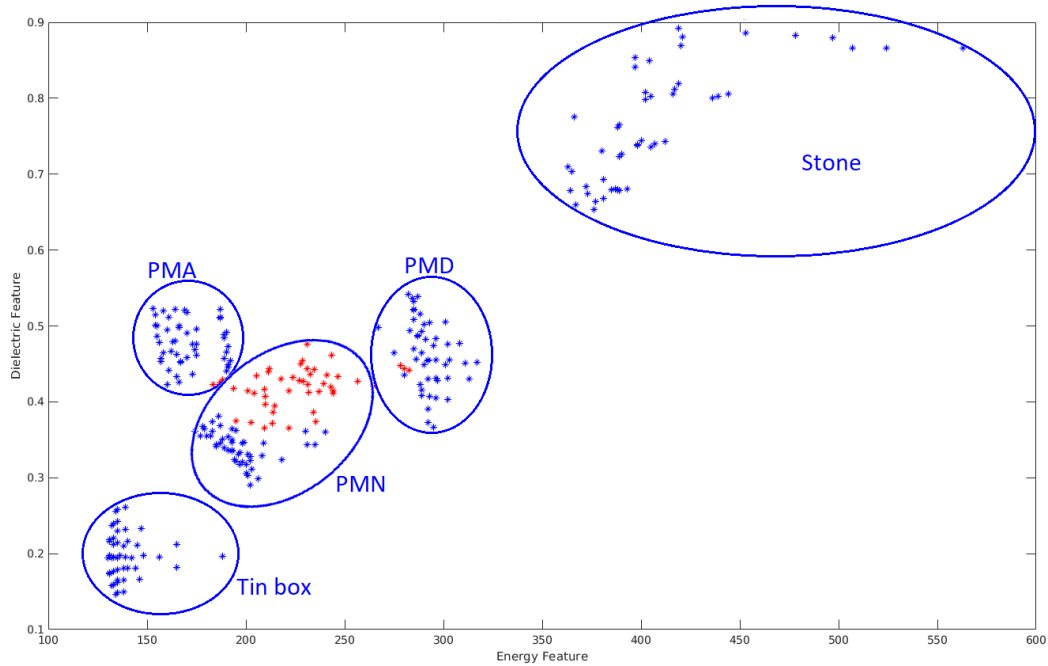
Figure 4.32. Different Orientations of PMN Landmine

CHAPTER 5

CONCLUSION

This study proposes two-stage algorithm as the first stage is calibration measurement and second stage is detection and classification of buried objects by utilizing three discriminative features. Results show that the proposed features in this study increase discrimination performance when compared to two well-known image-based features. The main reason is that image-based feature extraction techniques analyze the overall texture of B-Scan image in detail. This texture primarily depends on shape of the buried object. Object material type partially effects secondary reflections; hence texture of B-Scan image indirectly depends on the material type of the buried object. However, soil inhomogeneity and random clutter deteriorate the texture and creates secondary effects on the B-Scan data. Therefore, image-based features of a buried object change due to clutter effect, so the discrimination performance of these algorithms decreases. On the other hand, this paper extracts a simple feature (geometry feature) about the size of the buried object. It is a rough estimation of gradient of the underground target and the corruptive effect of clutter to the geometry feature is less compared to the same effect to image-based features. To achieve more robust solution, this paper combines the rough gradient estimation with the dielectric and energy feature that depend on material type directly. Therefore, the proposed features in this study do not consider only the texture of B-Scan image but also the material content of the buried object. In first place, this is the main advantage of the proposed study with respect to image-based techniques.

Moreover, computational complexity of the proposed algorithm is lower than many image-based techniques as given in the results section. Since, the proposed algorithm uses a three-dimensional feature vector which has pretty lower size than many feature descriptors in the literature. Therefore, extraction of the proposed features and classification of them are computationally cheaper.

Additionally, the algorithm proposed in this study is highly robust against target orientation and measurement errors (due to GPR step size and equipment noise) as given in the results section.

Furthermore, the algorithm derived in this paper proposes to take a calibration measurement in the experimental area before starting landmine sweeping. This calibration step is not common for GPR-based landmine detection algorithms in the literature. Although it seems an extra workload for landmine sweeping, it is very advantageous and increases the performance efficiently. The context can be clearly identified and the properties of the surrounding soil can be revealed by means of the calibration step. The initial measurement can be updated during landmine sweeping by using the recent ground bounce value. Hence, the context information can be revealed for each measurement separately. Moreover, users complain about the low performance of some commercial GPRs. The main reason is that manufacturers produce GPR and train the algorithm by using the data set in the country of origin. When they sell this GPR to another country, performance of the algorithm decreases for very different soil types under very different environmental conditions. To prevent this kind of performance loss, the calibration measurement is very beneficial to adapt the algorithm for dissimilar areas with different environmental conditions.

In the future, iterative approaches to calculate the dielectric properties of underground objects [11] can be applied to extract the dielectric feature derived in this study. By doing so, the calibration measurement can be removed from the algorithm. In addition, the proposed algorithm should be tested on real landmine and innocuous object data set.

REFERENCES

[1] H. Tozan and M. Karatas, "Operations Research for Military Organizations," *IGI Global, Hershey PA*, (2018).

[2] International Campaign to Ban Landmines, Landmine Monitor 2018 (ICBL-CMC: November 2018), www.the-monitor.org.

[3] L. Maresca and S. Maslen, "The Banning of Anti-Personnel Landmines," The Legal Contribution of the International Committee of the Red Cross, Cambridge University Press, 2004.

[4] Applied Engineering Products, "Unexploded Ordnance Removal Problem," www.aepcoinc.com.

[5] G. Borgioli et al., "The Detection of Buried Pipes from Time-of-Flight Radar Data," IEEE Transactions on Geoscience and Remote Sensing, vol. 46, no. 8, pp. 2254–2266 (2008).

[6] H. Chen and A. G. Cohn, "Probabilistic Robust Hyperbola Mixture Model for Interpreting Ground Penetrating Radar Data," Proceedings IJCNN 2010, pp. 1-8 (2010).

[7] R. Firoozabadi et al., "Subsurface Sensing of Buried Objects Under a Randomly Rough Surface using Scattered Electromagnetic Field Data," IEEE Transactions on Geoscience and Remote Sensing, vol. 45, no. 1, pp. 104–117 (2007).

[8] O. Lopera et al., "Filtering Soil Surface and Antenna Effects from GPR Data to Enhance Landmine Detection," IEEE Transactions on Geoscience and Remote Sensing, vol. 45, no. 3, pp. 707–717 (2007).

[9] F. Soldovieri, O. Lopera and S. Lambot, "Combination of Advanced Inversion Techniques for an Accurate Target Localization via GPR for Demining Applications," IEEE Transactions on Geoscience and Remote Sensing, vol. 49, no. 1, pp. 451–461 (2011).

[10] C. R. Ratto et al., "Physics-based Features for Identifying Contextual Factors Affecting Landmine Detection with Ground-Penetrating Radar," Proceedings of the SPIE Conference on Detection and Sensing of Mines, Explosive Objects and Obscured Targets XVI, vol. 8017, (2011).

[11] O. L. Mancilla and E. G. Trevino, "Ground Penetrating Radar Inversion in 1-D: An Approach for the Estimation of Electrical Conductivity, Dielectric Permittivity and Magnetic Permeability," Journal of Applied Geophysics, vol. 43, no. 2, pp. 199–213 (2000).

[12] T. Wang et al., "Frequency Sub-band Processing and Feature Analysis of Forward-Looking Ground Penetrating Radar Signals for Landmine Detection," IEEE Transactions on Geoscience and Remote Sensing, vol. 45, no. 3, pp. 718-729 (2007).

[13] D. P. Williams, V. Myers and M. S. Silvious, "Mine Classification with Imbalanced Data," IEEE Geoscience and Remote Sensing Letters, vol. 6, no. 3, pp. 528–532 (2009).

[14] E. Pasolli, F. Melgani and M. Donelli, "Automatic Analysis of GPR Images: A Pattern-Recognition Approach," IEEE Transactions on Geoscience and Remote Sensing, vol. 47, no. 7, pp. 2206–2217 (2009).

[15] J. S. Kobashigawa et al., "Classification of Buried Targets using Ground Penetrating Radar: Comparison between Genetic Programming and Neural Networks," IEEE Antennas and Wireless Propagation Letters, vol. 10, pp. 971–974 (2011).

[16] A. B. Yoldemir and M. Sezgin, "A Least Squares Approach to Buried Object Detection using Ground Penetrating Radar," IEEE Sensors Journal, vol. 11, no. 6, pp. 1337–1341 (2011).

[17] P. D. Gader, M. Mystkowski and Y. Zhao, "Landmine Detection with Ground Penetrating Radar using Hidden Markov Models," IEEE Transactions on Geoscience and Remote Sensing, vol. 39, no. 6, pp. 1231–1244 (2001).

[18] S. E. Yuksel and P. D. Gader, "Context-based Classification Using a Mixture of Hidden Markov Models with Applications in Landmine Detection," IET Computer Vision, vol. 10, no. 8, pp. 873-883 (2016).

[19] S. E. Yuksel, J. Bolton and P. D. Gader, "Multiple Instance Hidden Markov Models with Applications to Landmine Detection," IEEE Transactions on Geoscience and Remote Sensing, vol. 53, no. 12, pp. 6766–6775 (2015).

[20] H. Frigui and P. Gader, "Detection and Discrimination of Landmines in Ground Penetrating Radar based on Edge Histogram Descriptors and a Possibilistic K-Nearest Neighbor Classifier," IEEE Transactions on Fuzzy Systems, vol. 17, no. 1, pp. 185–199 (2009).

[21] P. A. Torrione et al., "Histogram of Gradient Features for Buried Threat Detection in Ground Penetrating Radar Data," Proceedings IGARSS 2012, pp. 3182-3185 (2012).

[22] P. A. Torrione et al., "Histograms of Oriented Gradients for Landmine Detection in Ground Penetrating Radar Data," IEEE Transactions on Geoscience and Remote Sensing, vol. 52, no. 3, pp. 1539–1550 (2014).

[23] D. Reichman, L. M. Collins and J. M. Malof, "Improvements to the Histogram of Oriented Gradient (Hog) Pre-screener for Buried Threat Detection in Ground

Penetrating Radar Data," Proceedings of the SPIE Conference on Detection and Sensing of Mines, Explosive Objects and Obscured Targets XXII, vol. 10182, (2017).

[24] S. Lameri et al., "Landmine Detection from GPR Data using Convolutional Neural Networks," Proceedings EUSIPCO 2017, pp. 508-512 (2017).

[25] D. Reichman, L. M. Collins and J. M. Malof, "Some Good Practices for Applying Convolutional Neural Networks to Buried Threat Detection in Ground Penetrating Radar," Proceedings IWAGPR 2017, pp. 1-5 (2017).

[26] L. E. Besaw and P. J. Stimac, "Deep Convolutional Neural Networks for Classifying GPR B-Scans," Proceedings of the SPIE Conference on Detection and Sensing of Mines, Explosive Objects and Obscured Targets XX, vol. 9454, (2015).

[27] A. Genc and G. B. Akar, "A GPR-based Landmine Identification Method using Energy and Dielectric Features," Proceedings of the SPIE Conference on Detection and Sensing of Mines, Explosive Objects and Obscured Targets XXIII, vol.10628, (2018).

[28] C. Ratto, P. A. Torrione and L. M. Collins, "Exploiting Ground-Penetrating Radar Phenomenology in a Context-Dependent Framework for Landmine Detection and Discrimination," IEEE Transactions on Geoscience and Remote Sensing, vol. 49, no. 5, pp. 1689–1700 (2011).

[29] B. Scheers, "Ultra-Wideband Ground Penetrating Radar, with Application to the Detection of Antipersonnel Landmines (Doctoral Dissertation)," retrieved from Royal Military Academy, (2011).

[30] D. J. Daniels, *Ground Penetrating Radar*, Institution of Electrical Engineers, London (2004).

[31] E. C. Utsi, *Ground Penetrating Radar Theory and Applications*, Elsevier (Butterworth-Heinemann), Oxford (2017).

[32] X. L. Travassos et al., "A Review of Ground Penetrating Radar Antenna Design and Optimization," Journal of Microwaves, Optoelectronics and Electromagnetic Applications, vol. 17, no. 3, pp. 385-402 (2018).

[33] F. Fioranelli, "Through-the-Wall Detection Using Ultra Wide Band Frequency Modulated Interrupted Continuous Wave Signals (Doctoral Dissertation)," retrieved from Durham University, (2013).

[34] E. Pasolli et al., "Automatic Detection and Classification of Buried Objects in GPR Images using Genetic Algorithms and Support Vector Machines," IEEE International Geoscience and Remote Sensing Symposium, vol. 2, pp. 525-528 (2008).

[35] U. Pisipati, "Techniques for Improving Landmine Detection using Ground Penetrating Radar (Master's Thesis)," retrieved from University of Missouri (2006).

[36] A. Van der Merwe and J. Gupta, "A Novel Signal Processing Technique for Clutter Reduction in GPR Measurements of Small, Shallow Land Mines," IEEE Transactions on Geoscience and Remote Sensing, vol. 38, no. 6, pp. 2627-2637 (2000).

[37] H. Brunzell, "Clutter Reduction and Object Detection in Surface Penetrating Radar," Proceedings of IEEE Radar Conference, vol. 449, pp. 688-691 (1997).

[38] J. W. Brooks, L. M. V. Kempen and H. Sahli, "Primary Study in Adaptive Clutter Reduction and Buried Minelike Target Enhancement from GPR Data," Proceedings of the SPIE Conference on Detection and Remediation Technologies for Mines and Minelike Targets V, vol. 4038, pp. 1183-1192 (2000).

[39] A. Gunatilaka and B.A. Baertlein, "A Subspace Decomposition Technique to Improve GPR Imaging of Anti-Personnel Mines," Proceedings of the SPIE Conference on Detection and Remediation Technologies for Mines and Minelike Targets V, vol. 4038, (2000).

[40] W. Al-Nuaimy et al., "Automatic Detection of Buried Utilities and Solid Objects with GPR using Neural Networks and Pattern Recognition," Journal of Applied Geophysics, vol. 43, no. 2–4, pp. 157–165 (2000).

[41] B. Karlsenab et al., "Antenna Characteristics and Air-Ground Interface De-Embedding Methods for Stepped-Frequency Ground Penetrating Radar Measurements," Proceedings of the SPIE Conference on Detection and Remediation Technologies for Mines and Minelike Targets V, vol. 4038, pp. 1420 (2000).

[42] S. H. Yu, R. K. Mehra and T. R. Witten, "Automatic Mine Detection based on Ground Penetrating Radar," Proceedings of the SPIE Conference on Detection and Remediation Technologies for Mines and Minelike Targets IV, vol. 3710, pp. 961–972 (1999).

[43] B. Karlsen et al., "Comparison of PCA and ICA based Clutter Reduction in GPR Systems for Anti-Personal Landmine Detection," 11th IEEE Signal Processing Workshop on Statistical Signal Processing, pp. 146-149 (2001).

[44] F. S. Tjora, E. Eide and L. Lundheim, "Evaluation of Methods for Ground Bounce Removal in GPR Utility Mapping," 10th International Conference on Ground Penetrating Radar, pp 1-4 (2004).

[45] L. van Kempen et al., "Signal Processing and Pattern Recognition Methods for Radar AP Mine Detection and Identification," Second International Conference on the Detection of Abandoned Land Mines, pp. 81 - 85 (1998).

[46] P. D. Gader, W. Lee and J. Wilson, "Detecting Landmines with Ground Penetrating Radar using Feature-Based Rules, Order Statistics, and Adaptive Whitening," IEEE Transactions on Geoscience and Remote Sensing, vol. 42, no. 11, pp. 2522-2534 (2004).

[47] M. P. Masarik et al., "GPR Anomaly Detection with Robust Principal Component Analysis," Proceedings of the SPIE Conference on Detection and Sensing of Mines, Explosive Objects and Obscured Targets XX, vol. 9454, (2015).

[48] A. Etebari, "QSCAN: Method for Real Time Anomaly Detection using GPR Imaging," Proceedings of the SPIE Conference on Detection and Sensing of Mines, Explosive Objects and Obscured Targets XVII, vol. 8357, (2012).

[49] B. Baydar et al., "Fusion of KLMS and Blob based Pre-screener for Buried Landmine Detection using Ground Penetrating Radar," Proceedings of the SPIE Conference on Detection and Sensing of Mines, Explosive Objects and Obscured Targets XXI, vol. 9823, (2016).

[50] P. A. Torrione, C. S. Throckmorton and L. M. Collins, "Performance of an Adaptive Feature-based Processor for a Wideband Ground Penetrating Radar System," IEEE Transactions on Aerospace and Electronic Systems, vol. 42, no. 2, pp. 644–658 (2006).

[51] R. Mahmood, A. Sadjadi and H. Pan, "Two-Dimensional Block Diagonal LMS Adaptive Filtering," IEEE Transactions on Signal Processing, vol. 42, no. 9, pp. 2420–2429 (1994).

[52] P. A. Torrione et al., "Application of the LMS Algorithm to Anomaly Detection using the Wichmann/NIITEK Ground Penetrating Radar," Proceedings of the SPIE Conference on Detection and Remediation Technologies for Mines and Minelike Targets VIII, vol. 5089, (2003).

[53] M. Stiles, V. Apte and B. Beh, "A Group-Theoretic Analysis of Symmetric Target Scattering with Application to Landmine Detection," IEEE Transactions on Geoscience and Remote Sensing, vol. 40, no. 8, (2002).

[54] H. Frigui, P. D. Gader and J. M. Keller, "Fuzzy Clustering for Land Mine Detection," Proceedings of NAFIPS 1998, pp. 261-265 (1998).

[55] P. D. Gader et al., "New Results in Fuzzy Set based Detection of Landmines with GPR," Proceedings of the SPIE Conference on Detection and Remediation Technologies for Mines and Minelike Targets IV, vol. 3710, pp. 1075-1084 (1999).

[56] P. D. Gader and M. Mystkowski, "Applications of Hidden Markov Models to Detecting Landmines with Ground Penetrating Radar," Proceedings of the SPIE Conference on Detection and Remediation Technologies for Mines and Minelike Targets IV, vol. 3710, pp. 1085-1093 (1999).

[57] E. Duflos et al., "Time-Frequency Analysis of Ground Penetrating Radar Signals for Mines Detection Applications," IEEE International Conference on Systems, Man, and Cybernetics, pp. 520-525 (1999).

[58] O. Lopera et al., "Time–Frequency Domain Signature Analysis of GPR Data for Landmine Identification," 4th International Workshop on Advanced Ground Penetrating Radar, pp. 159–162 (2007).

[59] T. G. Savelyev et al., "Investigation of Time-Frequency Features for GPR Landmine Discrimination," IEEE Transactions on Geoscience and Remote Sensing, vol. 45, no. 1, pp. 118–129 (2007).

[60] M. H. Horng, "Texture Feature Coding Method for Texture Classification," Optical Engineering, vol. 42, no. 1, pp. 228-238 (2003).

[61] K. C. Ho et al., "An Investigation of Using the Spectral Characteristics from Ground Penetrating Radar for Landmine Clutter Discrimination", IEEE Transactions on Geoscience and Remote Sensing, vol. 46, no. 4, pp. 1177-1192 (2008).

[62] C. Harris and M. Stephens, "A Combined Corner and Edge Detector," Proceedings of the Alvey Vision Conference, pp. 147–151 (1988).

[63] H. Bay, T. Tuytelaars, and L. Van Gool, "Surf: Speeded up Robust Features," Lecture Notes in Computer Science - Computer Vision ECCV 2006, vol. 3951, pp. 404–417 (2006).

[64] D. G. Lowe, "Distinctive Image Features from Scale-Invariant Keypoints," International Journal of Computer Vision, vol. 60, pp. 91–110 (2004).

[65] M. Calonder et al., "Brief: Binary Robust Independent Elementary Features," Lecture Notes in Computer Science - Computer Vision ECCV, vol. 6314, pp. 778–792 (2010).

[66] N. Dalal and B. Triggs, "Histograms of Oriented Gradients for Human Detection," IEEE Computer Society Conference on Computer Vision and Pattern Recognition (CVPR) 2005, vol. 1, pp. 886–893 (2005).

[67] P. Viola and M. J. Jones, "Robust Real-Time Face Detection," International Journal of Computer Vision, vol. 57, no. 2, pp. 137–154 (2004).

[68] C. Papageorgiou and T. Poggio, "A Trainable System for Object Detection," International Journal of Computer Vision, vol. 38, pp. 15–33 (2000).

[69] R. Sakaguchi, "Image Processing Methods Applied to Landmine Detection in Ground Penetrating Radar (Master's Thesis)," retrieved from Duke University (2013).

[70] P. Gamba and S. Lossani, "Neural Detection of Pipe Signatures in Ground Penetrating Radar Images," IEEE Transactions on Geoscience and Remote Sensing, vol. 38, no. 2, pp. 790-797 (2000).

[71] S. Delbo, P. Gamba and D. Roccato "A Fuzzy Shell Clustering Approach to Recognize Hyperbolic Signatures in Subsurface Radar Images," IEEE Transactions on Geoscience and Remote Sensing, vol. 38, pp. 1447-1451 (2000).

[72] A. C. Braun, U. Weidner and S. Hinz, "Classification in High-Dimensional Feature Spaces—Assessment Using SVM, IVM and RVM with Focus on Simulated EnMAP Data," IEEE Journal of Selected Topics in Applied Earth Observations and Remote Sensing, vol. 5, no. 2, pp. 436-443 (2012).

[73] Y. Bazi and F. Melgani "Toward an Optimal SVM Classification System for Hyperspectral Remote Sensing Images," IEEE Transactions on Geoscience and Remote Sensing, vol. 44, no. 11, pp. 3374-3385 (2006).

[74] Z. Gavrilov, "SVM Tutorial (Doctoral Dissertation)," retrieved from Massachusetts Institute of Technology (2012).

[75] M. E. Tipping, "The Relevance Vector Machine," Advances in Neural Information Processing Systems, vol. 12, pp. 652-658 (2000).

[76] D. G. Tzikas et al., "A Tutorial on Relevance Vector Machines for Regression and Classification with Applications," EURASIP News Letter, vol. 17, no.2, (2006).

[77] M. E. Tipping, "Sparse Bayesian Learning and the Relevance Vector Machine," Journal of Machine Learning Research, pp. 211-244 (2001).

[78] M. E. Tipping and A. C. Paul, "Fast Marginal Likelihood Maximization for Sparse Bayesian Models," Proceedings of the 9th International Workshop on Artificial Intelligence and Statistics, (2003).

[79] L. Breiman, "Random Forests," Machine Learning, vol. 45, pp. 5-32 (2001).

[80] H. Wold, "Estimation of Principal Components and Related Models by Iterative Least Squares," Journal of Multivariate Analysis, pp. 391-420 (1966).

[81] M. Barker and W. Rayens, "Partial Least Squares for Discrimination," Journal of Chemometrics, vol. 17, no. 3, pp. 166-173 (2003).

[82] E. Fix and J. L. Hodges, "Discriminatory Analysis, Nonparametric Discrimination: Consistency Properties," International Statistical Review, vol. 57, no. 3, pp. 238-247 (1989).

[83] R. M. Balabin, R. Z. Safieva and E. I. Lomakina, "Gasoline Classification using Near Infrared (NIR) Spectroscopy Data: Comparison of Multivariate Techniques," Analytica Chimica Acta, vol. 671, no. 1-2, pp. 27-35 (2010).

[84] J. M. Keller, M. R. Gray and J. A. Givens, "A Fuzzy K-Nearest Neighbor Algorithm," IEEE Transactions on Systems, Man, And Cybernetics, vol. 15, no. 4, pp. 580-585 (1985).

[85] J. V. Oliveira and W. Pedrycz, *Advances in Fuzzy Clustering and its Applications*, John Wiley & Sons (2007).

[86] R. Krishnapuram, H. Frigui and O. Nasraoui, "The Fuzzy C Quadric Shell Clustering Algorithm and the Detection of Second-Degree Curves," Pattern Recognition Letters, vol. 14, pp. 545-552 (1993).

[87] J. Han, M. Kamber and J. Pei, *Data Mining Concepts and Techniques*, Elsevier, Massachusetts (2012).

[88] K. M. A. Chai, H. T. Ng and H. L. Chieu, "Bayesian Online Classifiers for Text Classification and Filtering," Proceedings of the 25th Annual International ACM SIGIR, pp. 97-104 (2002).

[89] K. Saravanan and S. Sasithra, "Review on Classification based on Artificial Neural Networks," International Journal of Ambient Systems and Applications, vol. 2, no. 4, pp. 11-18 (2014).

[90] B. D. Ripley, "Neural Networks and Related Methods for Classification," Journal of the Royal Statistical Society, vol. 56, no. 3, pp. 437-456 (1994).

[91] W. H. Lee, "Ground-Tracking for On and Off-Road Detection of Landmines with Ground Penetrating Radar," Proceedings of the 24th Army Science Conference, pp. 11-15 (2006).

[92] D. K. Cheng, *Fundamentals of Engineering Electromagnetics*, Prentice-Hall, New Jersey (1993).

[93] R. E. Collin, *Foundations for Microwave Engineering*, IEEE Press, New York (2001).

[94] S. J. Orfanidis, *Electromagnetic Waves and Antennas*, Rutgers University Press, New Jersey (2008).

[95] K. Takahashi, H. Preetz and J. Igel, "Soil Properties and Performance of Landmine Detection by Metal Detector and Ground Penetrating Radar – Soil Characterization and Its Verification by a Field Test," Journal of Applied Geophysics, vol. 73, pp. 368–377 (2011).

[96] E. A. Awak et al., "Determination of Soil Electrical Conductivity using Ground Penetrating Radar (GPR) for Precision Agriculture," International Journal of Science and Engineering Research (IJSER), vol. 8, no. 1, pp. 1971–1977 (2017).

[97] F. Parrini et al, "ULTRA: Wideband Ground Penetrating Radar," Proceedings of 3rd European Radar Conference, pp. 182-185 (2006).

[98] L. Qu and Y. Yin, "Non-Uniform Fast Fourier Transform based Fast Back-Projection Algorithm for Stepped Frequency Continuous Wave Ground Penetrating Radar Imaging," Journal of Applied Remote Sensing, vol. 10, no. 4, (2016).

[99] H. Zhang et al., "Back-Projection Algorithm based on Self-Correlation for Ground Penetrating Radar Imaging," Journal of Applied Remote Sensing, vol. 9, no. 1, (2015).

[100] H. A. Haus and J. R. Melcher, *Electromagnetic Fields and Energy*, Prentice-Hall, New Jersey (1989).

[101] G. Leucci, "Ground Penetrating Radar: The Electromagnetic Signal Attenuation and Maximum Penetration Depth," Scholarly Research Exchange, vol. 1, pp. 1-7 (2008).

[102] A. Giannopoulos and C. Warren, "gprMax: Electromagnetic Modelling Software," (2015) [www.gprmax.com].

[103] T. A. Milligan, *Modern Antenna Design*, IEEE Press, John Wiley & Sons inc. (2007).

[104] B. Scheers et al., "Time Domain Modeling of UWB GPR and Its Application on Landmine Detection," Proceedings of the SPIE Conference on Detection and Remediation Technologies for Mines and Minelike Targets V, vol. 4038, (2000).

[105] S. N. Haubrock et al., "Surface Soil Moisture Quantification and Validation based on Hyperspectral Data and Field Measurements," Journal of Applied Remote Sensing, vol. 2, no. 1, (2008).

[106] S. Esch et al., "Soil Moisture Index from ERS-SAR and Its Application to the Analysis of Spatial Patterns in Agricultural Areas," Journal of Applied Remote Sensing vol. 12, no. 2, (2018).

[107] M. Dogan and G. T. Sayan, "Preprocessing of A-Scan GPR Data based on Energy Features," Proceedings of the SPIE Conference on Detection and Sensing of Mines, Explosive Objects and Obscured Targets XXI, vol. 9823, (2016).

[108] J. Zhang, Q. Liu and B. Nath, "Landmine Feature Extraction and Classification of GPR Data based on SVM Method," Proceedings of International Symposium on Neural Networks, pp. 636-641 (2004).

[109] I. Giannakis, A. Giannopoulos and C. Warren, "A Realistic FDTD Numerical Modeling Framework of Ground Penetrating Radar for Landmine Detection," IEEE Journal of Selected Topics in Applied Earth Observations and Remote Sensing, vol. 9, no. 1, pp. 37-51 (2016).

[110] N. R. Peplinski, F. T. Ulaby and M. C. Dobson, "Dielectric Properties of Soils in the 0.3-1.3 GHz Range," IEEE Transactions on Geoscience and Remote Sensing, vol. 33, no. 3, pp. 803–807 (1995).

[111] F. T. Hallikainen et al., "Microwave Dielectric Behavior of Wet Soil-Part 1: Empirical Models and Experimental Observations," IEEE Transactions on Geoscience and Remote Sensing, vol. 23, no. 1, pp. 25–34 (1985).

[112] M. C. Dobson et al., "Microwave Dielectric Behavior of Wet Soil-Part 2: Dielectric Mixing Models," IEEE Transactions on Geoscience and Remote Sensing, vol. 23, no. 1, pp. 35–46 (1985).

[113] W. Patitz, B. Brock and E. Powell, "Measurement of Dielectric and Magnetic Properties of Soil: Sandia Report SAND95-2419," Sandia National Laboratory, vol. 87185, no. 46, (1995).

[114] A. Smith, "PMA landmine," (2002) [https://nolandmines.com/minesPMA1.htm].

[115] A. Smith, "PMD landmine," (2002) [https://nolandmines.com/PMD6.htm].

[116] A. Smith, "PMN landmine," (2002) [https://nolandmines.com/minesPMN.htm].

[117] R. E. Fan, P. H. Chen and C. J. Lin, "Working Set Selection Using Second Order Information for Training Support Vector Machines," Journal of Machine Learning Research, vol. 6, pp. 1889-1918, (2005).

APPENDICES

A. Comparison of Normal and Oblique Incidence for Calibration Measurement

In this study, calculations are performed under normal incidence case to achieve physics-based parameters as shown in Figure 3.3. However, there is a distance between transmitter and receiver of GPR, therefore an oblique ray transmitted from TX can reach RX of GPR as shown in Figure 0.1. In the figure, the distance between TX and RX is 2d; position of the reflection point on the PEC surface is denoted by (x, y) and center of the PEC surface is assumed as origin (0, 0). In this section, we will show the difference between the calculations for normal incidence case and for oblique rays during calibration measurement.
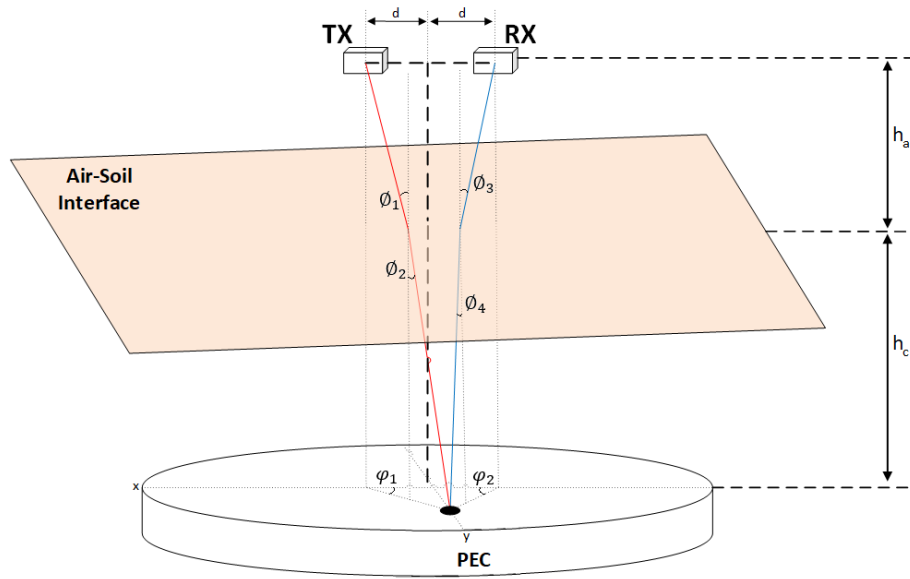

Figure 0.1. Calibration Measurement Setup by Considering Oblique Rays

If we focus on the incident wave transmitted from TX and the return wave reflected from PEC surface separately, 2-D drawings can be achieved as shown in Figure 0.2.
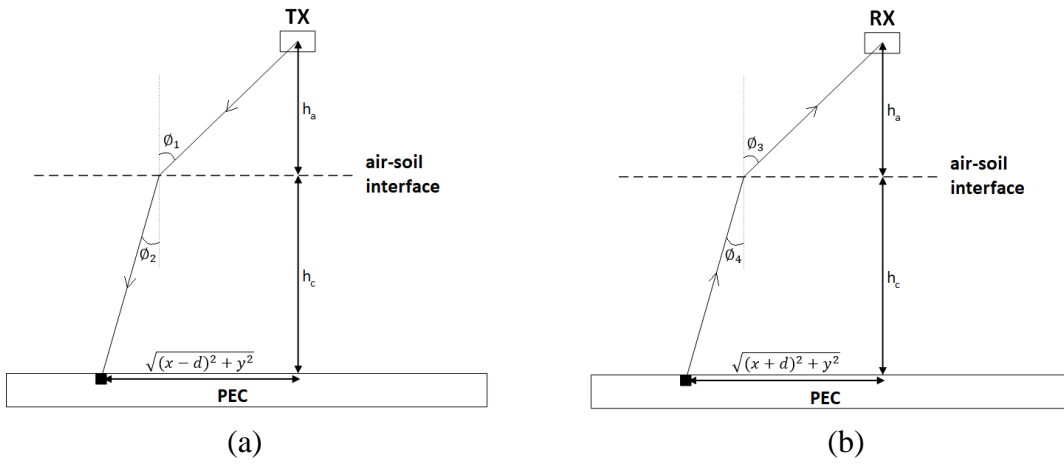
Figure 0.2. (a) Incident Wave Transmitted from TX, (b) Return Wave Reflected from PEC Surface

According to the Brewster's Law [92], angles $\emptyset_1, \emptyset_2, \emptyset_3$ and $\emptyset_4$ should satisfy the following equations.

$$\sin \emptyset_1 = \sqrt{\epsilon_{soil}} \sin \emptyset_2, \tag{73}$$

$$\sin \emptyset_3 = \sqrt{\epsilon_{soil}} \sin \emptyset_4, \tag{74}$$

During simulations, Hertzian dipole antenna is used. Radiation pattern of a dipole antenna is shown in Figure 0.3 [103].

Figure 0.3. Radiation Pattern of Dipole Antenna

The shape of the pattern resembles a bagel. The signal strength does not change with respect to angle along x-axis. However, the signal strength is proportional with $\cos\theta$ where θ is the angle between the projection of the signal onto x=0 plane and z axis as shown in Figure 0.4 [103].

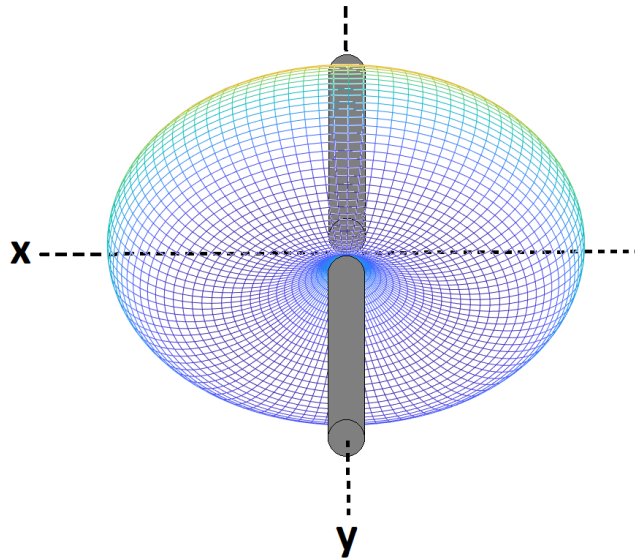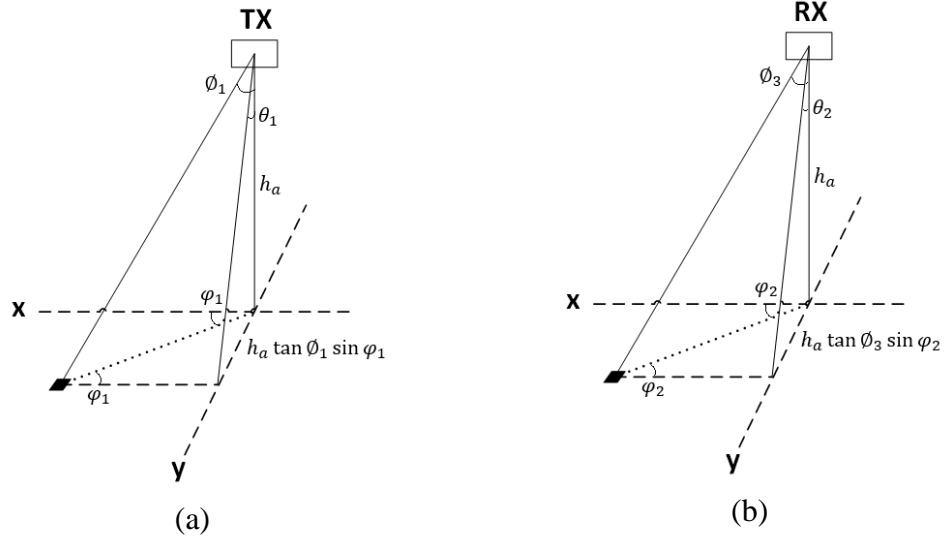*Figure 0.4.* (a) Angle between the Projection of the Transmitted Signal onto x=0 Plane and z Axis, (b) Angle between the Projection of the Return Signal onto x=0 Plane and z Axis

According to Figure 0.4, θ_1 and θ_2 can be computed as:

$$\theta_1 = \tan^{-1}(\tan\emptyset_1 \sin\varphi_1), \tag{75}$$

$$\theta_2 = \tan^{-1}(\tan\emptyset_3 \sin\varphi_2), \tag{76}$$

Transmission and reflection for normal incidence are given in Eq. 41. For oblique rays, these coefficients can be computed according to Fresnel's Equations as follows [92]:

$$\tau_{as} = \frac{2\cos\emptyset_1}{\cos\emptyset_1 + \sqrt{\epsilon_{soil}}\cos\emptyset_2}, \tag{77}$$

$$\tau_{sa} = \frac{2\sqrt{\epsilon_{soil}}\cos\emptyset_4}{\cos\emptyset_3 + \sqrt{\epsilon_{soil}}\cos\emptyset_4}, \tag{78}$$

During calibration measurement, a PEC object with smooth surface is used. Hence, the incident wave is reflected from the PEC surface with the same angle as shown in Figure 0.5.

Figure 0.5. Total Reflection at the PEC Surface

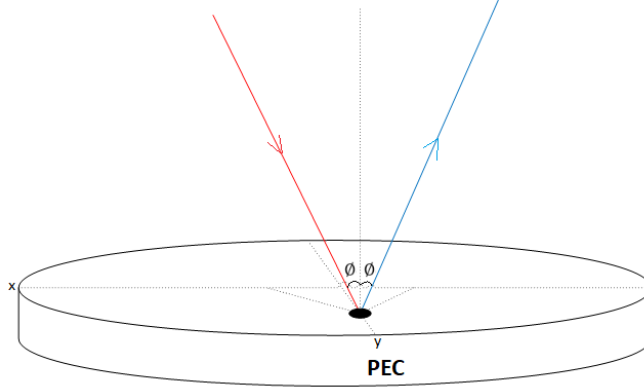Therefore, amplitude of the return signal from a PEC surface under oblique incidence conditions can be written as in Eq. 79 [104].

$$\left| E_{return\_PEC}^{oblique}(h_c) \right| = |E_0| \left| \tau_{as}^{oblique} \tau_{sa}^{oblique} \right| \frac{\cos\theta_1 \cos\theta_2}{8\pi^2 R_{TX} R_{RX}} e^{-\alpha_s h_c (\cos\emptyset_2 + \cos\emptyset_4)}, \quad (79)$$

$$\text{where } \tau_{as}^{oblique} = \frac{2\cos\emptyset_1}{\cos\emptyset_1 + \sqrt{\epsilon_{soil}}\cos\emptyset_2},$$

$$\tau_{sa}^{oblique} = \frac{2\sqrt{\epsilon_{soil}}\cos\emptyset_4}{\cos\emptyset_3 + \sqrt{\epsilon_{soil}}\cos\emptyset_4},$$

$$R_{TX} = h_a \cos\emptyset_1 + h_c \cos\emptyset_2,$$

$$R_{RX} = h_a \cos\emptyset_3 + h_c \cos\emptyset_4,$$

As given in Section 3.1.2, amplitude of the return signal from a PEC surface under normal incidence conditions can be written as in Eq. 80.

$$\left| E_{return\_PEC}^{normal}(h_c) \right| = |E_0| \left| \tau_{as}^{normal} \tau_{sa}^{normal} \right| \frac{1}{8\pi^2 (h_a + h_c)^2} e^{-2\alpha_s h_c}, \quad (80)$$

$$\text{where } \tau_{as}^{normal} = \frac{2}{1 + \sqrt{\epsilon_{soil}}},$$

$$\tau_{sa}^{normal} = \frac{2\sqrt{\epsilon_{soil}}}{1 + \sqrt{\epsilon_{soil}}},$$

During simulations, $h_a = 160\ mm$, $d = 15\ mm$ and PEC radius is 50 mm. We have created 12 different soil types which have relative permeability of 1, conductivity of

116

10 mS/m and relative permittivity between 4.5 and 10 with the increment of 0.5. Calibration object is buried at depths between 50 mm and 150 mm. For different soil types and different burial depths, percentage differences between Eq. 79 and Eq. 80 are given in Table 0.1.

Table 0.1. *Percentage Differences between Eq. 79 and Eq. 80*

Depth:	50mm	60mm	70mm	80mm	90mm	100mm	110mm	120mm	130mm	140mm	150mm
Soil-1	1,91	1,78	1,67	1,57	1,48	1,39	1,32	1,25	1,18	1,12	1,07
Soil-2	1,94	1,82	1,71	1,60	1,51	1,43	1,35	1,28	1,21	1,15	1,10
Soil-3	1,97	1,85	1,74	1,64	1,54	1,46	1,38	1,31	1,25	1,19	1,13
Soil-4	2,00	1,88	1,77	1,67	1,57	1,49	1,41	1,34	1,28	1,21	1,16
Soil-5	2,03	1,91	1,80	1,69	1,60	1,52	1,44	1,37	1,30	1,24	1,19
Soil-6	2,05	1,93	1,82	1,72	1,63	1,54	1,47	1,39	1,33	1,27	1,21
Soil-7	2,07	1,95	1,84	1,74	1,65	1,57	1,49	1,42	1,35	1,29	1,23
Soil-8	2,10	1,97	1,87	1,77	1,67	1,59	1,51	1,44	1,37	1,31	1,26
Soil-9	2,11	1,99	1,89	1,79	1,69	1,61	1,53	1,46	1,40	1,33	1,28
Soil-10	2,13	2,01	1,90	1,81	1,71	1,63	1,55	1,48	1,42	1,35	1,30
Soil-11	2,15	2,03	1,92	1,82	1,73	1,65	1,57	1,50	1,44	1,37	1,32
Soil-12	2,17	2,05	1,94	1,84	1,75	1,67	1,59	1,52	1,45	1,39	1,33

As shown in Table 0.1, the difference between Eq. 79 and Eq. 80 is less than % 2 therefore, normal incidence assumption is acceptable during the calculations.

B. Calculation of Intrinsic Impedance for Low-loss Dielectrics and Good Conductors

In Section 3.4.1, it is written that the working medium satisfies low-loss condition and our main interest is to identify buried landmines with little or no metal content. These landmines are made of plastic, rubber, bakelite, glass or wood. All these materials also satisfy low-loss condition. So, the following equations are correct.

$$\eta_s \cong Re\{\eta_s\}, \tag{81}$$

$$\eta_t \cong Re\{\eta_t\}, \tag{82}$$

Under these conditions, intrinsic impedance of the target is estimated by using Eq. 83;

$$\eta_t^k \cong Re\{\eta_t^k\} \cong \begin{cases} Re\{\eta_s^k\} \frac{1+|\Gamma_{st}^k|}{1-|\Gamma_{st}^k|} & if \ Re\{\eta_t^k\} > Re\{\eta_s^k\} \\ Re\{\eta_s^k\} \frac{1-|\Gamma_{st}^k|}{1+|\Gamma_{st}^k|} & else \end{cases}, \tag{83}$$

If the buried object is highly conductive material (such as metallic innocuous object), then η_t becomes:

$$\eta_t = \sqrt{\frac{j\omega\mu_t}{\sigma_t+j\omega\epsilon_t}} \cong 0 \ since \ \sigma_t \gg \omega\mu_t, \tag{84}$$

In this case, the buried object behaves like a calibration object and $|\Gamma_{st}|$ becomes almost 1. So, Eq. 83 gives that $\eta_t^k \cong 0$. Hence, our proposed approach also works for highly conductive targets.

For the buried objects which do not satisfy low-loss or highly conductive conditions, the result of Eq. 83 is calculated theoretically. For two different soil types (soil type-1: $\mu_{s_1} = 1, \epsilon_{s_1} = 4.5, \sigma_{s_1} = 0.01 \ S/m$ / soil type-2: $\mu_{s_1} = 1, \epsilon_{s_1} = 6, \sigma_{s_1} = 0.01 \ S/m$), dielectric properties of the buried object is chosen as: $\mu_t = 1, \epsilon_t = 10$ and σ_t changes between 10^{-4} and 10^8. Figure 0.6 shows the theoretical results of $Re\{\eta_t\}$ computed by Eq. 39 and the simulated results computed by Eq. 83.
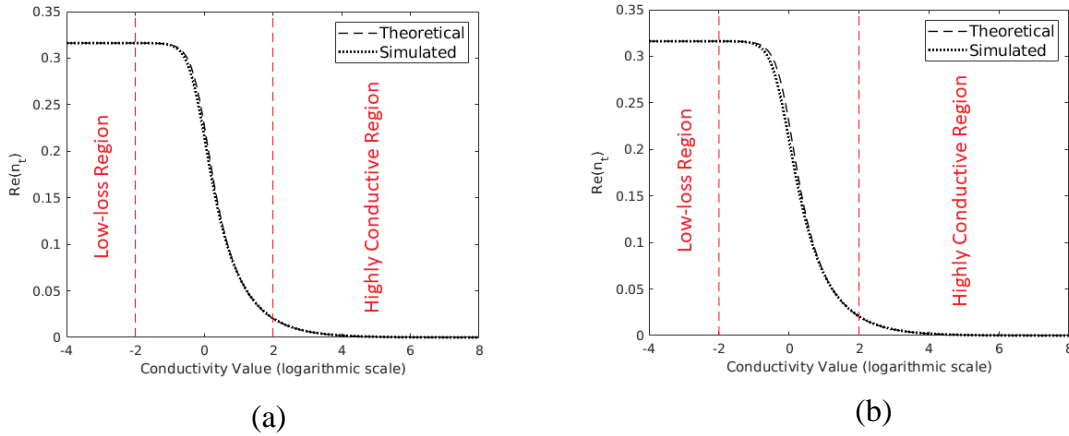

Figure 0.6. Theoretical and Simulated Results of $Re\{\eta_t\}$ into (a) Soil Type-1, (b) Soil Type-2

The buried object satisfies low-loss condition when $\sigma_t < 10^{-2}$ and highly conductive condition when $\sigma_t > 10^2$. For these two regions, theoretical and simulated results are

almost the same as shown in Figure 0.6. For the other region, theoretical and simulated results are close enough. Therefore, Eq. 83 can be used to calculate $Re\{\eta_t\}$ for all underground objects.

C. A Sample gprMax Input File

In this study, simulation experiments are performed by using gprMax electromagnetic modeling software. gprMax, which simulates electromagnetic wave propagation, is an open source software. It solves Maxwell's equations in 3D by applying Yee's algorithm and uses the Finite Difference Time Domain (FDTD) method [102, 109]. A sample gprMax input file, to simulate PMA landmine in a soil with $\mu_s = 1, \epsilon_s = 4.5, \sigma_s = 0.01$ at 10 cm depth is shown in Figure 0.7.

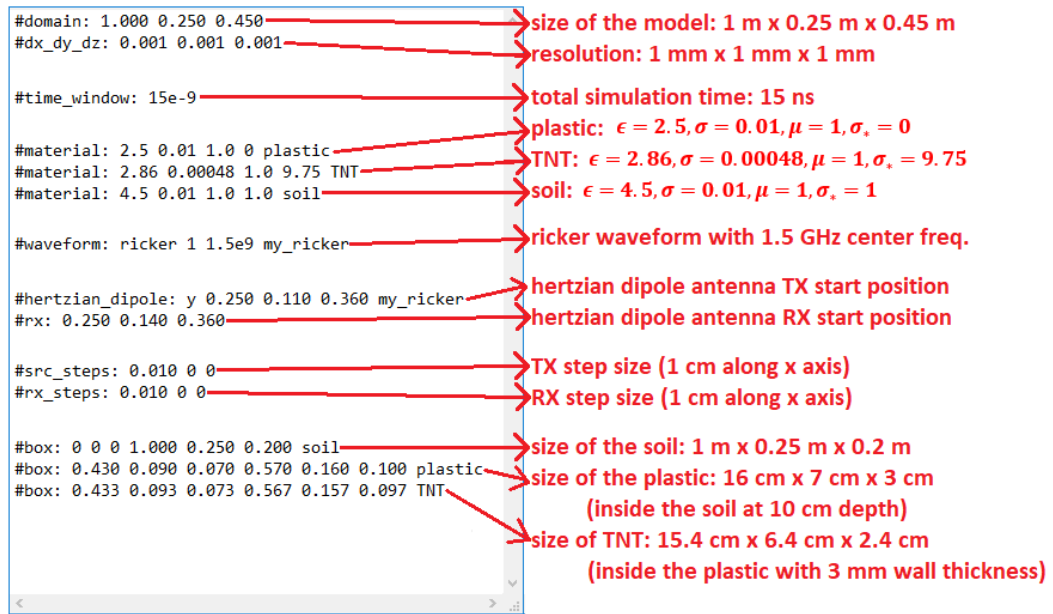*Figure 0.7*. A Sample gprMax Input File

CURRICULUM VITAE

PERSONAL INFORMATION

Surname, Name	: Genç, Alper
Nationality	: Turkish (TC)
Date and Place of Birth	: 1 February 1987, Ankara
Phone	: +90 530 110 77 08
E-mail	: alper.genc@metu.edu.tr

EDUCATION

Degree	Institution	Year of Graduation
MS	Eindhoven University of Technology, Embedded Systems, the Netherlands	2011
BS	I.D. Bilkent University Electrical and Electronics Engineering, Ankara	2009
High School	Ankara Science High School, Ankara	2005

WORK EXPERIENCE

Year	Place	Enrollment
2015-2019	ASELSAN INC.	Systems Engineer
2011-2015	ASELSAN INC.	Hardware Design Engineer
2010-2011	ASML (the Netherlands)	Candidate Engineer

FOREIGN LANGUAGES

Advanced English, Mid German

PUBLICATIONS

1. A. Genc and G. B. Akar, "Combination of Physics-based and Image-based Features for Landmine Identification in Ground Penetrating Radar Data," Journal of Applied Remote Sensing, vol. 13, no. 3, (2019).

2. A. Genc and G. B. Akar, "A GPR-based landmine identification method using energy and dielectric features," Proceedings of the SPIE Conference on Detection and Sensing of Mines, Explosive Objects and Obscured Targets XXIII, vol.10628, (2018).

3. A. Genc, M. K. Akkaya and A. E. Yılmaz, "Ground Penetrating Radar Signal Enhancement by Surface Covering Method," Proceedings IGARSS (2018).

4. M. K. Akkaya, A. Genc and A. E. Yılmaz, "A Random Modeling Approach for the Description of Underground Layers," Proceedings IGARSS (2018).

HOBBIES

Swimming, Skiing, Movies